Petrogenesis and Tectonic Implications of Almond Trondhjemite of Southern Appalachians in Alabama

by

Ozan Sinoplu

A thesis submitted to the Graduate Faculty of
Auburn University
in partial fulfillment of the
requirements for the Degree of
Master of Science

Auburn, Alabama
August 2023

Appalachian Orogeny, granite, (isotope)-geochemistry, thermochronology
tectonics

Approved by

Dr. Haibo Zou, Chair, Professor – Auburn University, Department of Geosciences
Dr. Willis E. Hames, Professor – Auburn University, Department of Geosciences
Dr. Timothy M. Kusky, Distinguished Professor – China University of Geosciences (Wuhan), School of Earth Sciences

Abstract

In the southernmost Appalachians, Devonian-Carboniferous Eastern Blue Ridge (EBR) syn/post-orogenic granitoids are examined in two groups, high Sr/Y and low Sr/Y granitoids. The Almond Trondhjemite (AT) is a part of these Alleghenian granitoids, and it shows high Sr/Y ratio, as well as other adakitic geochemical characteristics, and intrudes Wedowee Group metasedimentary rocks. Its parent melt was proposed to result from heating of lower crust by upwelling asthenospheric mantle via delamination. The existing data on AT is neither complete nor statistically robust to support this interpretation. New whole rock geochemistry data was complemented by critical novel data such as Sr-Nd isotope systematics, single mineral chemistry and $^{40}Ar/^{39}Ar$ thermochronology to solidify interpretations on its source, emplacement, and post crystallization history in the context of Paleozoic-Mesozoic tectonism in Southern Appalachians.

The AT is a weakly foliated, I-type peraluminous granitoid that consists of quartz+plagioclase (mostly oligoclase)+muscovite+biotite with trace amounts of orthoclase+zircon+apatite and secondary epidote+calcite. Sr-Nd isotope systematics, whole rock geochemistry and mineral chemistry support previous interpretations of a lower crustal source. Grenville orogenic affinity of this crustal source was proved with Sr-Nd isotopes. However, the lack of associated mantle related rocks in the vicinity argues against asthenospheric involvement in generation of the AT. Biotite crystallization temperatures show that the magma was fluxed with water during final stages of crystallization. Muscovite $^{40}Ar/^{39}Ar$ thermochronology suggests that cooling of the AT is controlled regional cooling, possibly on the footwall of a core complex-style exhumation.

Acknowledgements

First of all, I want to thank my parents Meryem Sinoplu, Mesut Sinoplu and Nurşen Kırkız, for without their support, I would not have any chance to pursue my dreams. I dedicate my thesis to them.

I would like to express my gratitude to my advisor Dr. Haibo Zou for his wisdom and critical guidance in the course of this project, as well as all he taught me on geochemical lab practices, mass spectrometry and academic world. Working with him in the lab was always a pleasure that transcended the boundaries of geological discussions. I also thank him for steering me through administrative and financial issues during my time in Auburn, as well as funding this study.

I would like to thank Dr. Willis (Bill) Hames for always being there to discuss problems related to this project and more. Discussions with him helped me a lot to shape my future academic endeavors. I also thank him for funding $^{40}Ar/^{39}Ar$ work and answering my endless questions on noble gas mass spectrometry with great patience and wisdom.

Dr. Tim Kusky was always there for me since we met in 2018. He first as my advisor, then as my reference to Auburn University, and lately as my committee member. I can't describe how grateful I am for his mentoring and friendship over the years. Even his vast knowledge of geology can't compare with his kind heart.

I am grateful to all my undergraduate professors in METU for teaching me not only geology, but also the ways of science. I owe special thanks to Dr. Erdin Bozkurt, Dr. Nuretdin Kaymakcı and Dr. Bora Rojay for their valuable input on the foundation of my scientific thinking and their continued friendship over the years.

I would like to thank Dr. Zeki Billor for encouraging me to apply for Auburn University, hence opening the door for me. He and Dr. Nedret Billor were always a great help in all matters and sources of continuous support. I owe my thanks to Sara Speetjens for her help during my time in Auburn and her input to my thesis, and to Dogancan Yasar for fruitful discussions in academics and more, for his help on $^{40}Ar/^{39}Ar$ work, as well as his help during my time in Auburn. I would also like to express gratitude to Yağmur Yavuz Özdemir, Rıdvan Özdemir and Turgay Yıldırım for making Auburn a better place to live.

Mert İnanç Örge is thanked for always being there and putting up with my academic and personal problems.

I also owe thanks to Dr. David Brink-Roby, Dr. Ashraf Uddin, Dr. Laura Bilenker for their support and creating a welcoming environment in the department and Auburn University Geosciences Advisory Board for partially funding my thesis.

There are many more people academically and personally involved in my long journey for this degree. Last but not least, my thanks extend to all my friends in different parts of the world for their continuous support and encouragement through rough times. If you are reading this and do not see your name, please know that it was not intentional, and thank you.

"All that is gold does not glitter,

Not all those who wander are lost.

The old that is strong does not wither,

Deep roots are not reached by the frost."

J.R.R. Tolkien

Table of Contents

List of Figures

List of Tables

Appendices

List of Abbreviations

IP	Inner Piedmont
EBR	Eastern Blue Ridge
AT	Almond Trondhjemite
REE	Rare Earth Elements
LREE	Light Rare Earth Elements
HREE	Heavy Rare Earth Elements
HFSE	High Field Strength Elements
MORB	Mid-Ocean Ridge Basalt
WT%	Weight Percent
LOI	Loss on Ignition
EPMA	Electron Probe Micro Analysis
METU	Middle East Technical University
AU-EMPA	Auburn University Electron Microprobe Analysis Lab
AU-ISOLAB	Auburn University Isotope Geochemistry Lab
ANIMAL	Auburn Noble Gas Isotope Mass Analysis Laboratory
BSE	Back-Scattered Image
WDS	Wavelength Dispersive Spectrometer
QA/QC	Quality Assurance/Quality Control
TIMS	Thermal Ionization Mass Spectrometer
LILE	Large Ion Lithophile Elements
CIAAW	Commission on Isotopic Abundances and Atomic Weights
IUPAC	International Union of Pure and Applied Chemistry

1. Introduction

Deciphering ancient plate tectonic puzzles requires solid knowledge on bookmarks through time such as supercontinents, ancient oceans and orogenies. Orogenies probably are the best of these because of their sub-linear extent, grand footprint and trackable nature among continents that are separate now. To define an orogeny, one should identify rocks of different origins bounded by faults and sutured in a sub-linear trend. Rocks of each zone (or terrane) in these accretionary settings will have genetic relationships and identification of different terranes is done based on multiple lines of evidence using petrology, geochemistry, paleomagnetism, geochronology, and paleontology (see reviews by Cawood et al., 2009; Kusky et al., 2016; Kusky and Şengör, 2023). When the oceanic crust between these terranes is lost to subduction, remaining pieces are accreted on top of each other and amalgamated since their density is not high enough and/or their root is too thick to subduct fully. Intense compressional deformation and metamorphism obviously accompanies the amalgamation process which results in increase in relief and creation of fold and thrust belts, as well as orogens. Driving forces of the deformation are mainly slab pull and ridge push. During the peak orogenic activity, the relief is controlled by the interplay of these driving forces, isostasy, and erosion. After some time (tens of millions of years), when driving forces of slab pull and ridge push are no longer effective by slab detachment and/or ridge extinction, roles of isostasy and erosion take full control of topography. This generally leads to a decrease in relief in the long-term as high relief is more prone to erosion. This interplay between isostatic rebound and erosion results in unroofing of deep rocks, generally by orogen-parallel normal faulting. In ancient orogens, such as Appalachians, the relief is greatly lost to erosion and extension, terrane-based identification and correlation with their lateral extent, and foreland basin studies are important to identify and constraint these.

Igneous activity can be present in all stages of an orogenic system, from subduction stage to post-collisional extension stage and resulting rocks hold precious information on timing of events, emplacement environments, as well as deep processes beneath the orogen (e.g., Kusky and Wang, 2022). Geochemical/isotope geochemical studies on well-mapped areas are required to unroof this information. Overprinting metamorphic conditions can be observed on igneous rocks better than sedimentary rocks and they are generally better candidates for geochronological applications. Furthermore, spatiotemporal variations in igneous characteristics can be used to make regional tectonic interpretations. For these reasons, studying igneous rocks is essential in tectonic studies. Continuous development in analytical techniques is also creating the need for new and improved data to be produced for more sophisticated interpretations.

This study focuses on southernmost Appalachians and uses geochemistry/isotope geochemistry to characterize an igneous body, the Almond Trondhjemite. Details of the study, its objective, methodology and the results are discussed in this manuscript.

1.1 Regional Geology

The Appalachian Orogen (*sensu lato*) formed in a long-lived series of orogenic episodes, forming a spatially extensive mountain belt that covers most of the eastern United States, eastern Quebec and Newfoundland with numbers of tectonic units overlying one another *(Figure 1)*. It is thought to correlate with orogens in Europe and be roughly coeval to the Caledonian and Variscan orogens (Scotese, 2004; Hatcher, 2010; Hibbard et al., 2010; Stampfli et al., 2013; Henderson et al., 2018), and possibly the Uralian Orogen (Pushkov, 1997). It records a complete Wilson Cycle, starting from cessation of Grenville Orogeny in Early Neoproterozoic (Tollo et al., 2004 *and references therein*) and ending with the opening of Atlantic Ocean in Jurassic (Labails et al., 2010 *and references therein*). The older Greenville orogeny marks the assembly

of supercontinent Rodinia, which rifted away by the opening of Iapetus and Rheic Oceans in Late Precambrian-Cambrian.

Major continental pieces that played significant roles in Appalachian orogenic events are Gondwana and Laurentia. During Silurian, convergence between these two masses started with other minor tectonic units accreting one on top of/next to one another. Accretion in the Appalachians occurred in four main stages or events, Taconic (Ordovician), Salinic (Silurian), Acadian-Neoacadian (Devonian-Mississippian) and Alleghenian (Pennsylvanian-Permian) (Hatcher, 2010). With the completion of amalgamation, the supercontinent Pangea was formed and a whole Wilson Cycle was completed. Researchers investigate the Appalachian orogen in two main parts: Southern Appalachians and Northern Appalachians. The boundary between these is not a sharp contact but it is roughly located around the New York Promontory, where the orogen is at its narrowest and widens toward either side *(Figure 1)*. This study focuses on the southern Appalachians.

The Southern Appalachians consists of polydeformed, folded/faulted, and metamorphosed terranes that lie in a NE-SW trend *(Figure 2)*. For *Figure 2*, it is important to note that Thigpen and Hatcher (2017) used the term Piedmont in a sense that includes central and eastern Blue Ridge, as well as Inner Piedmont and group them in their figure 1. Their map was modified to separate Inner Piedmont (IP) and Eastern Blue Ridge (EBR) terranes, for this study is concerned with EBR. These two and other neighboring terranes were accreted on top of each other during different stages of Appalachian orogeny, starting from Taconic (Middle-Late Ordovician). This stage marks the obduction of IP on top of Laurentia along Hayesville and Brevard Fault zones, squeezing minor continental/magmatic fragments in between (which includes EBR, *Figure 2*). Two major components of IP are the Dadeville Complex and EBR,

which consists of metamorphosed granitic, mafic and ultramafic plutonic rocks, amphibolite-facies metabasalts that formed the arc itself, as well as the back-arc basin that consists of mainly schists and other metasedimentary sequences. Emplacement of the Dadeville Complex is thought to have been completed by a dextral transpressional movement through an orogenic channel to its present location from north during later Alleghenian orogeny (Tull et al., 2018). Ma et al. (2019) on the other hand, suggests that this movement occurred during Acadian-Neoacadian orogeny. Nonetheless, metamorphism associated with Taconic orogeny reached up to granulite-eclogite facies (Moecher et al., 2004; Miller et al., 2010). This stage also has development of some arc and ophiolite systems that are observed in the Northern Appalachians, but these are either absent or not well-preserved in the south (Robinson, 1998).

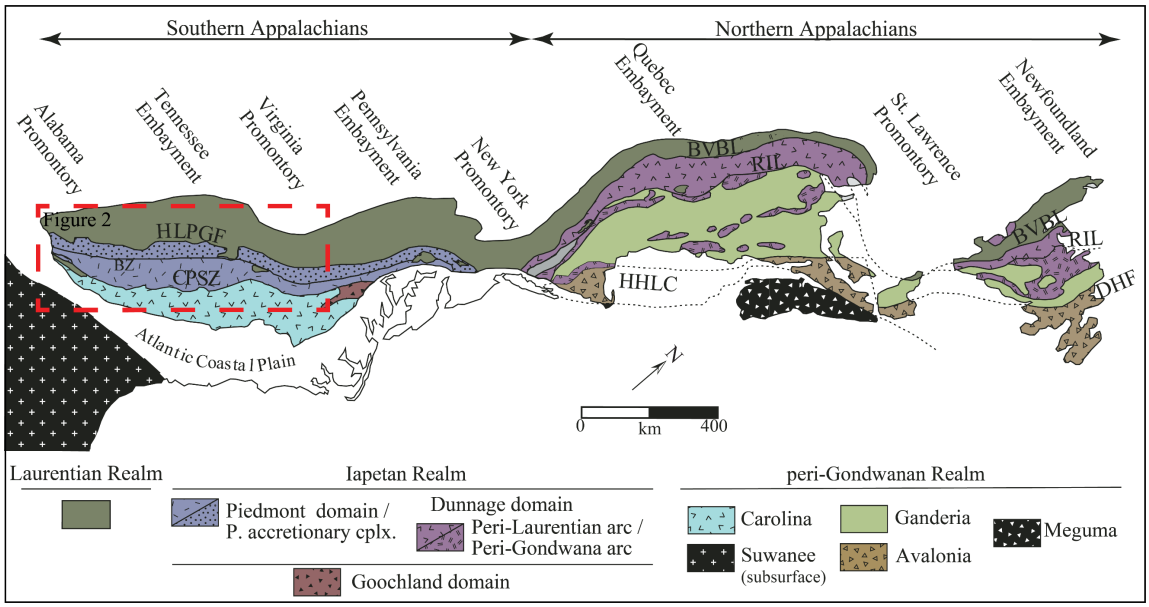

Figure 1: Major tectonic units of Appalachian Orogeny. BVBL—Baie Verte–Brompton Line; BZ—Brevard zone; CPSZ—central Piedmont shear zone; DHF—Dover–Hermitage Bay faults; HHLC—Honey Hill–Lake Char fault system; HLPGF—Hollins Line–Pleasant Grove fault system; RIL—Red Indian Line. Modified from Hibbard et al. (2010).

The subsequent Salinic event is not prominent in the Southern Appalachians and has been recognized mainly in the northern part of the orogen (van Staal et al., 2004), therefore the next event for the study region is Acadian-Neoacadian orogeny that marks docking of Avalon, Carolina and Ganderina(?) (super-)terranes to Laurentia (Shekan and Rast, 1990). Among these, only the Carolina Superterrane is found in the southernmost Appalachians, whereas the others belong to Northern Appalachians. Carolina is a composite superterrane that is peri-Gondwanan in origin, exotic to Laurentia, and it consists of Late Precambrian volcanic arc-subarc plutonic complexes as well as volcanogenic sediments related to these. Some of the sub-terranes of this unit were accreted and metamorphosed at ca.530Ma (Rast and Skehan, 1983; Barker et al., 1998), well before their amalgamation to Laurentia as a composite terrane during Acadian-Neoacadian events. This event is characterized by zippering tectonics from north to south with a westward subduction in the Southern Appalachians (Hatcher, 2010 *and references therein*). Moreover, the Cat Square Terrain, that consists of aluminous schist, metagreywacke and granites that intrude these, is thought to be a remnant ocean basin that accreted towards west during this time (Bream et al., 2004; Merschat and Hatcher, 2007). The latest Neoacadian orogeny is thought to be more uniform between northern and southern Appalachians (Hibbard et al., 2010) and this stage was accompanied by upper amphibolite facies metamorphism (Merschat et. al., 2005; Miller et al., 2010).

Acadian-Neoacadian was a long-lived stage and was followed by the last stage of Appalachian orogeny during Carboniferous, Alleghenian. This final stage marked the closure of the Rheic Ocean with amalgamation of Laurentia and Gondwana and formation of Pangea. Crustal thickness was at its highest during this orogenic event since it marked the climax of deformation with continent-continent collision and numerous thrust sheets were emplaced. The

Greater Black Warrior Basin was formed as a foreland basin due to flexural subsidence and it was later structurally separated into sub-basins (Thomas, 1976; Haque and Uddin, 2016). Metamorphic grade reached up to upper greenschist-lower amphibolite facies in EBR during this time (Miller et al., 2010, Stowell et al., 2019). With the collision, the Appalachian Orogeny *(sensu lato)* was completed, and supercontinent Pangea was formed.

Intense plutonism that had started at the latest Neoacadian also reached its climax during Alleghenian. A number of these plutons are cropping out in Alabama and were grouped as EBR plutons and IP plutons according to the tectonic units they intruded in. EBR plutons are felsic in composition and lying in an orogen parallel (SW-NE) trend *(Figure 3)*. These plutons contain important information for the tectonic evolution of southernmost Appalachians and for the crust-mantle interactions during the Paleozoic.

EBR plutons in southernmost Appalachians were grouped as low Sr/Y (Rockford Granite and Bluff Springs Granite) and high Sr/Y (Almond Trondhjemite, Blakes Ferry and Wedowee plutons) magmas with the former preceding the latter. Low Sr/Y suite is thought to be formed between ca 390Ma and 365Ma by anatexis of supracrustal rocks. The high Sr/Y suite formed between ca 349Ma and 335Ma and source these magmas is a matter of debate with previous arguments including partial melting of subducted oceanic crust and lower-crustal melting (Stowell et al., 2019 *and references therein*). Degree of mantle interaction during formation of high Sr/Y plutons is also controversial. One whole rock geochemistry data was presented for each pluton in this paper, therefore, the data validity is in question.

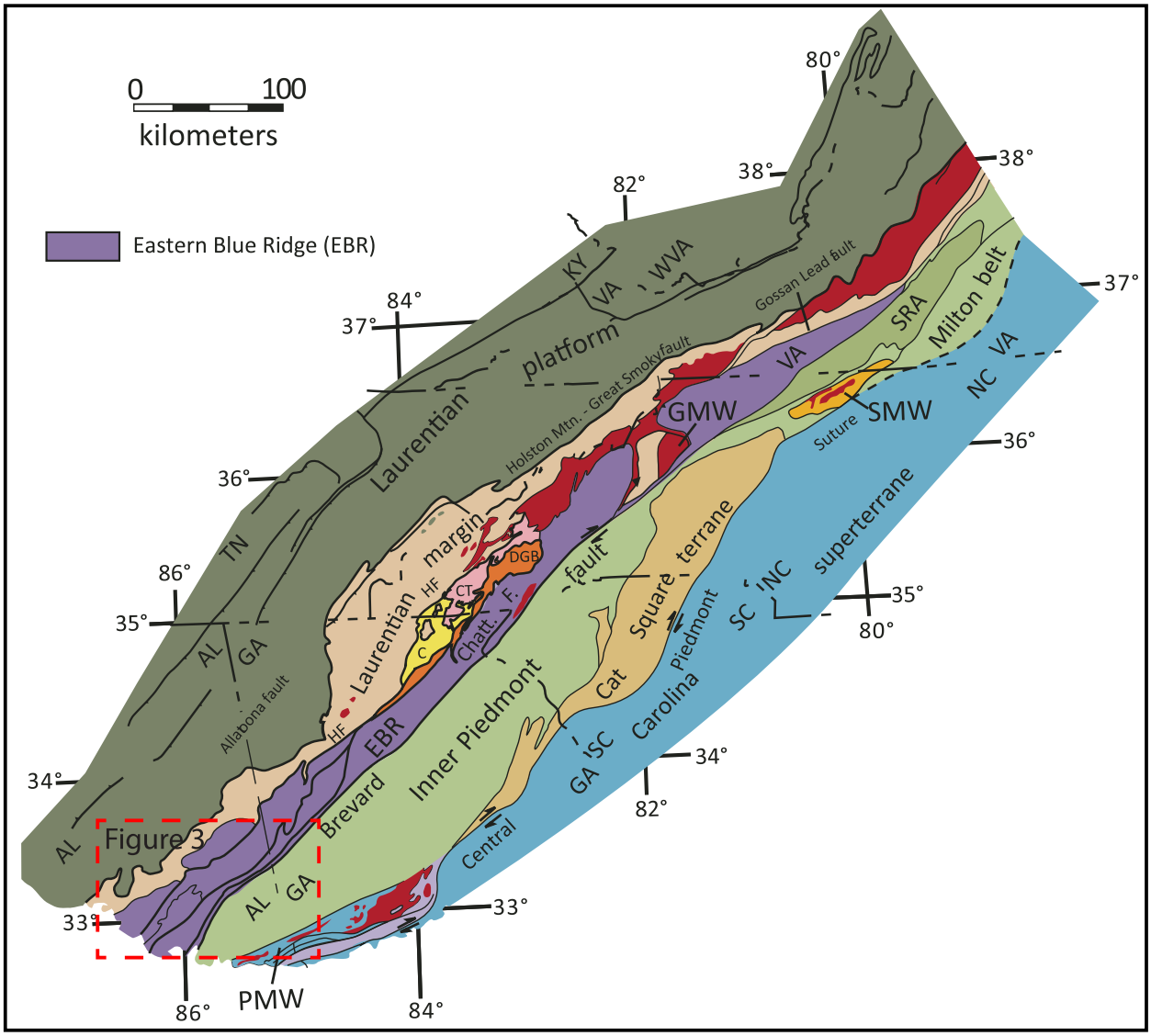

Figure 2: Simplified tectonic map of southern Appalachians. (Modified from Thigpen and Hatcher, 2017). Terrane of interest for this study is shown in legend and others are excluded for the sake of simplicity. C-Cowrock terrane, CT-Cartoogechaye terrane, Chatt F- Chattahoochee–Holland Mountain fault, GMW-Grandfather Mountain Window, HF- Hayesville Fault, PMW-Pine Mountain Window, SRA-Smith River allochthon.

The Almond Trondhjemite (AT) of high Sr/Y EBR plutons crops out as multiple small scale igneous bodies that show strong NE-SW elongation. *Figure 3* was made using shapefiles

that are available on the USGS website (https://pubs.er.usgs.gov/publication/ds1052) and the AT is shown with red outcrops. There seems to be a discrepancy in literature, some outcrops of the AT are named locally by some researchers as Blakes Ferry and Wedowee plutons (Neathery and Reynolds, 1975; Size and Dean, 1987). On top of these, some proportions of neighboring highly heterogeneous Rockford Granite seem to show trondhjemitic affinities (Deininger et al., 1973). Genetic relations between these trondhjemitic rocks were discussed in unpublished reports of Geological Survey of Alabama and although weak, there is evidence that these might belong to the same magma series. Another argument that is not conclusive was older Elkahatchee Quartz Diorite Gneiss was the source of high Sr/Y granitoids (Deininger et al., 1973; Size and Dean, 1987, Defant et al., 1987).

In this study, all the collected rocks are from the AT in its narrower description (i.e. which excludes, Blakes Ferry and Wedowee plutons). Tull (1978) suggested that the AT is pre-metamorphic to syn-metamorphic. Two of the samples were collected from an unmapped small outcrop of the AT (near Alexander City). It is defined as an I-type, peraluminous trondhjemite with metasediment-tonalite enclaves and intermediate SiO_2 (67%-71%) content (Deininger et al., 1973; Size and Dean, 1987) and it intrudes the Wedowee Group. Moreover, Stowell et al. (2019) classified it as a high Sr/Y suite and calculated initial $^{87}Sr/^{86}Sr$ as 0.7041-0.7054, using data from Russell et al. (1987) and their zircon $^{206}Pb/^{238}U$ age (~340 Ma). It should be noted that measured $^{87}Sr/^{86}Sr$ data of Russell et al. (1987) show a great uncertainty of ±0.0065. Stowell et al. (2019) argues that petrogenesis of Almond Trondhjemite is related to slab-breakoff that occurred in Latest Neoacadian-Earliest Alleghenian stage.

Whole rock geochemistry data regarding trondhjemitic bodies of EBR was compiled from unpublished reports and a thesis. It is apparent that the data is neither complete nor reliable by modern standards *(Appendix A)*.

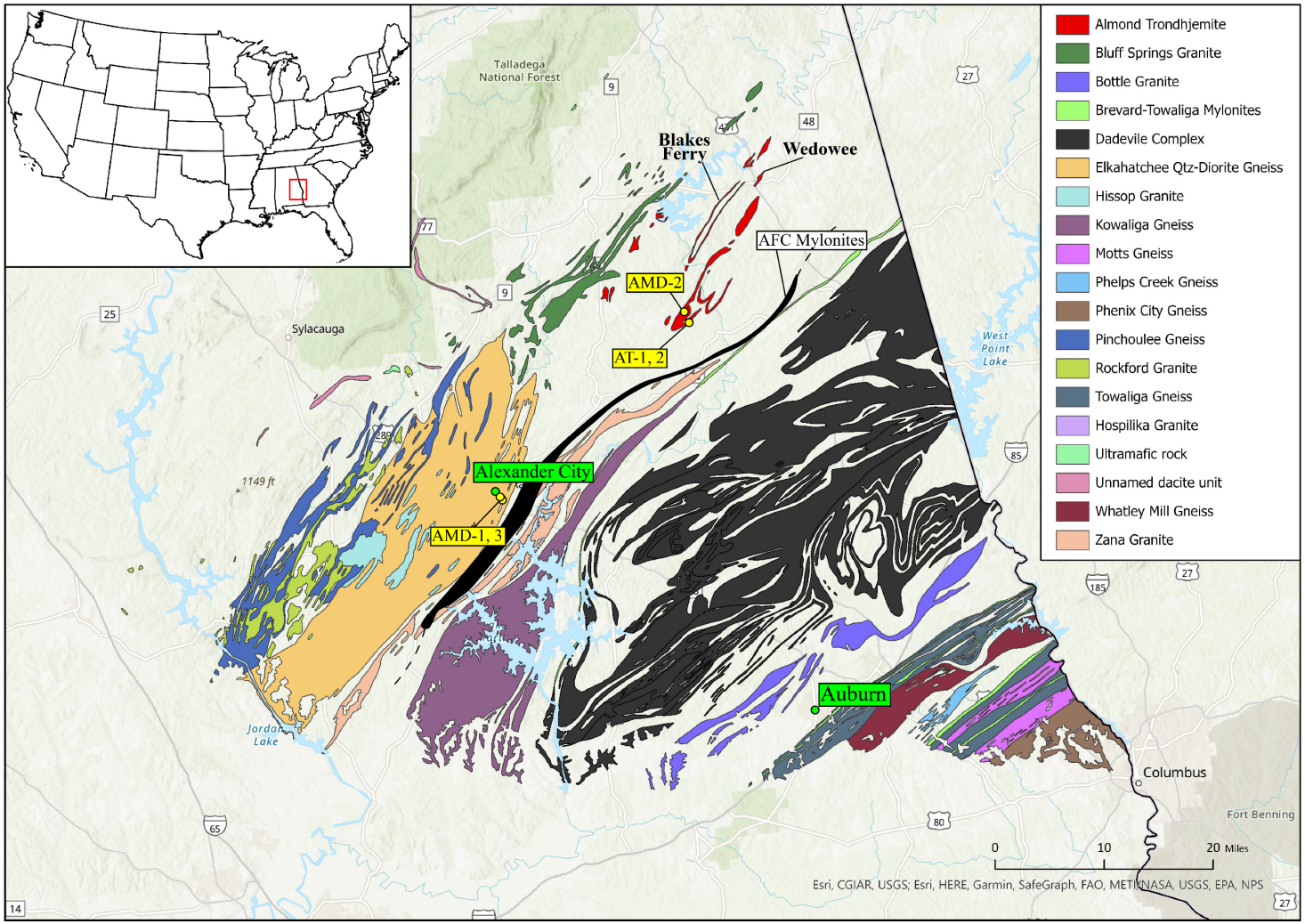

Figure 3: (Meta)-Igneous rocks of Alabama. Inner Piedmont rocks are combined for the sake of simplicity (Adapted from USGS [Horton, 2017]). Sample locations and two major cities are marked with yellow and green dots, respectively. Alexander City Fault (AFC) mylonite zone is from Steltenpohl et al. (2013).

1.2 A Note on Trondhjemites/Adakites

Adakites were defined by Defant and Drummond (1990), as "volcanic or intrusive rocks in Cenozoic associated with subduction of young (<25Myr) oceanic lithosphere", as they were documented in Adak Island (Alaska) by Kay (1978). 'Original adakites' are characterized by >56% SiO_2, >15% Al_2O_3 (rarely lower), usually <3% MgO, low Y and heavy rare earth elements (HREE) relative to island-arcs (for example, Y and Yb < 18 and 1.9 ppm, respectively), high Sr relative to island-arcs (rarely <400 p.p.m.), low high-field strength elements (HFSEs), as in most island-arcs. In the original definition, another possible way of generating adakitic rocks were given as melting of lower crust by underplating, however, this option was contended because of absence of negative Eu anomalies and >15% Al_2O_3 content. It was concluded that the anatexis of young oceanic slab (i.e., a slab that is hot enough to melt relatively early on its way to the mantle) is the source of adakites, as supported by existence of amphibolites and eclogites associated with these rocks (Defant and Drummond, 1990). However, in subsequent years, the term 'adakite' has started to be used in a broader context, regardless of petrogenesis and tectonic setting and became a more descriptive term rather than a petrogenetic one. In an attempt to constraint the term, Martin et al. (2005) further divided adakitic rocks into sub-groups, main ones being high-silica adakites, low-silica adakites and continental adakites. Apart from these, some fractionated andesites and sodic rhyolites were also discussed in this paper as they might show adakitic signature. Regardless of variations, adakitic signature is mainly characterized by high Sr/Y and La/Yb ratios. Sr and Y mobility during melting is depth sensitive. Destabilizing plagioclase at depth is releasing Sr whereas newly stabilizing garnet and amphibole retains Y which results in increasing Sr/Y ratio in resulting melt (Moyen, 2009). The effect of garnet/amphibole in residue is also observable as depleted HREE patterns. Apart from this, a

source with a high Sr/Y ratio is also possible, which bypasses the deep source argument. Another possible contribution to high Sr/Y and La/Yb ratios is mantle interaction, which would also increase Mg#, Cr and Ni values of the rock. Although garnet fractionation at depth is thought to be the main factor in creating the adakitic signature, further modification to a higher Sr/Y ratio is possible with shallower amphibole fractionation according to Moyen et al. (2007).

Experimental studies were successful in generating adakitic signature using mid-ocean ridge basalt (MORB) as starting material and applying fluid-absent melting conditions (Rapp and Watson, 1995; Moyen and Martin, 2012). According to some other experimental studies (Rudnick and Gao, 2003; Qian and Hermann, 2013), it is possible to generate adakites by 10-40 wt% melting of hydrous mafic lower crust in a depth as shallow as ~35km and with lower temperatures. This formation does not necessitate eclogitization and delamination *(Figure 4)*. It was also argued that K_2O content in adakites are mainly controlled by the source effect in some experiments (Wang et al., 2022 *and references therein*).

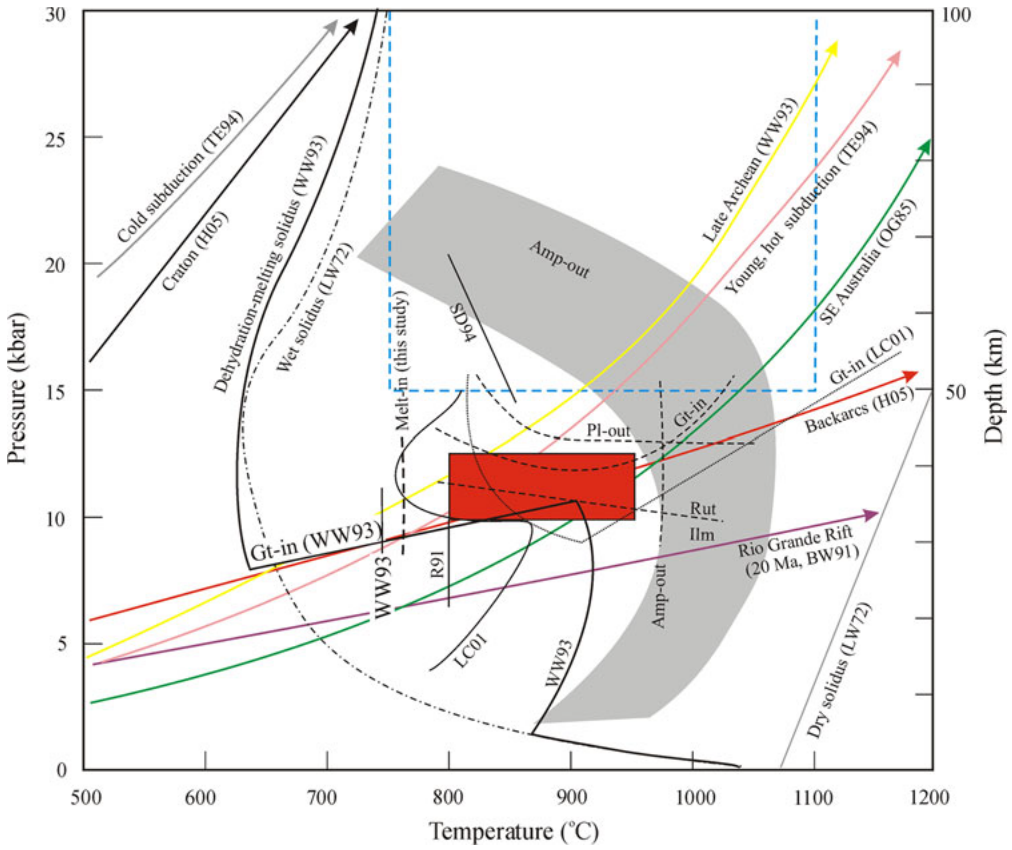

Figure 4: P-T diagram for adakitic melt generation. Red rectangle is the proposed conditions for adakite formation from partial melting of mafic lower crust and the blue rectangle represents previously proposed zone of adakite generation from subducted oceanic crust (Qian and Hermann, 2013; and references therein).

In the light of these, there are several possible geological settings that give rise to adakitic signature, the usual suspect being slab melting as the original proposition (Defant and Drummond, 1990; Kay et al., 1993; Qu et al., 2004; Martin et al., 2005;). Slab derived melts that interact with the mantle wedge or ridge subduction may alter chemical and Sr-Nd isotope signatures towards more primitive values (Aguillón-Robles et al., 2001, Tuena et al., 2008). Relatively shallow slab melting may be caused by ridge subduction in these settings. During the

rise of these magmas, they can have assimilation and fractional crystallization to a level that they produce high silica rhyolites as documented in Southern Philippines by Castillo et al. (1999).

Another mode of formation is partial melting of thickened lower crust (Petford and Atherton, 1996; Hou et al., 2004; Topuz et al., 2005; Guo et al., 2007; Eyuboglu et al., 2012; Zhao et al., 2013; Pang et al., 2016; Zhou et al., 2016; He et al., 2018; Hao et al., 2021). These can be primary melts or the ones that have equilibrated or interacted with mantle via delamination or underplating (Castillo, 2012) *(Figure 5)*. The former gives way to low MgO, high silica rocks and the latter results in high MgO (low FeO/MgO) and high Cr-Ni content. The difference between these two modes of formation should also be visible in Sr-Nd isotope signatures, as the involvement of mantle will result in lower $^{87}Sr/^{86}Sr$ and higher $^{143}Nd/^{144}Nd$ ratios. However, a possible complication regarding this is the degree of mantle melting effect, which will impact chemical signatures of the rock. This type of adakite petrogenesis also requires the lag time between cessation of subduction by collision and generation of adakites since increased crustal thickness is required. It also requires a heat source, especially for the low MgO-high silica rocks, that is generally argued to be mantle derived ultrapotassic-potassic rocks that are ponding in juvenile crust (MASH zone) to be this heat source. Lastly, some researchers argued that adakitic signatures can be achieved by hydrous melting or decompression melting through crustal extension (Wang et al., 2006) without an external heat source required.

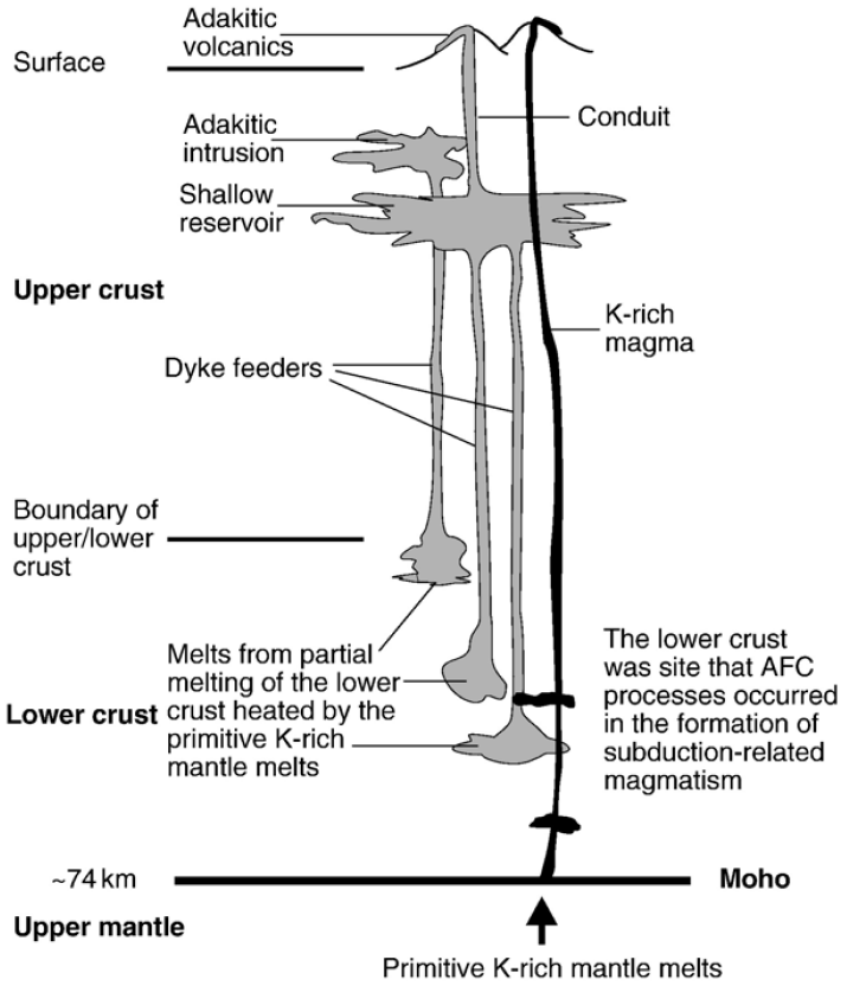

Figure 5: Proposed formation of post-collisional adakites from thickened crust in Lhasa Terrane.

Modified from Annen et. al. (2006) by Guo et al. (2007).

1.3 Objectives and Significance

The objective of this study is to generate precise, accurate and statistically acceptable geochemical data from fresh samples of the AT, which is an especially important problem in Southern Appalachians because of the polyphase deformation, regional/local overprinting metamorphism and subsequent weathering and alterations. Furthermore, the possibly

heterogeneous nature of igneous intrusions may lead to misleading interpretations. Therefore, additional data allow researchers to converge interpretations to true nature of this intrusive rock and its tectonic meaning.

Although there existed geochemical and Sr isotope data from the AT, it is scarce and was collected 70's and 80's and rather recent unpublished whole-rock geochemistry data of Ingram (2012) is questionable. The uncertainty of measured $^{87}Sr/^{86}Sr$ by Russell et al. (1987) is 0.0065 but modern mass spectrometer can achieve much higher precision <0.00001. In addition, Nd isotopic compositions ($^{143}Nd/^{144}Nd$) are still lacking but are needed for a robust geochemical characterization. The whole rock major and trace element data is rather recent (Ingram, 2012; Stowell et al., 2019) but it still needs to be complemented because of the reasons discussed above, as well as high Loss on Ignition (LOI) values of analyses in these manuscripts. Another aimed contribution is extensive data collection on single mineral major oxides using electron probe micro analysis (EPMA) which has not been reported from the AT. Lastly, another data that does not exist but will be produced is muscovite $^{39}Ar/^{40}Ar$ dating.

The AT was classified as a high Sr/Y granitoid by previous researchers and generation of high Sr/Y granitoids is a matter of debate in the literature as established earlier in this manuscript. Discussion about these potential sources of the AT requires more reliable whole rock major and trace element geochemistry and Sr-Nd isotope data because of their combined strength of characterizing magma source and evolution. Single mineral geochemistry by EPMA also was used to interpret emplacement conditions (i.e., temperature, pressure) using biotite thermobarometer. Lastly, muscovite $^{39}Ar/^{40}Ar$ data will be used in combination with published zircon U/Pb ages to interpret late/post emplacement history. In combination, these datasets

present a holistic story about the AT by allowing the complete interpretation of magma source/evolution, emplacement, and subsequent cooling history.

2. Methodology

Five samples are presented in this study. Four of these, AT-1, AT-2, AMD-2 and AMD-3 have been used for all analyses that will be presented later. One sample, AMD-1 was used for $^{40}Ar/^{39}Ar$ analyses only. Although it might create confusion, sample names that were given at the time of collection were preserved. AMD-1, 2 and 3 *(Figure 6)* were collected by Dr. Haibo Zou, AT-1 and AT-2 *(Figure 7)* were collected by Sara Speetjens and Bishop Robbins, prior to the author's arrival to Auburn and they were generously offered for this study. Sample locations can be seen in *Figure 3*. Later, additional fieldwork was conducted to possibly observe contact relations and collect more samples. Two more samples were collected but geochemical data collection on these was not possible during the course of this project.

Figure 6: Field photo of AMD-2 outcrop.

Figure 7: Field photo of AT-1 and AT-2 outcrop.

Figure 8: The author standing on an outcrop of AT.

Four samples were prepared for Electron Probe Micro Analysis (EPMA) and polarized microscope analyses in Sample Preparation Laboratory, Middle East Technical University

(METU, TUR). EPMA was conducted at Auburn University Electron Microprobe Analysis Lab (AU-EMPA). Whole rock major and trace element compositions of the same four samples were measured using XRF and ICP-MS, respectively, at Wuhan Sample Solution Analytical Technology to characterize the Almond Trondhjemite. $^{87}Sr/^{86}Sr$ and $^{143}Nd/^{144}Nd$ isotope ratios were determined in Wuhan Sample Solution Analytical Technology and Auburn University Isotope Geochemistry Lab (AU-ISOLAB). This analysis further constrains the petrogenesis of Almond Trondhjemite. Lastly, muscovite $^{40}Ar/^{39}Ar$ dating was done in Auburn Noble Gas Isotope Mass Analysis Laboratory (ANIMAL).

2.1 Whole Rock Geochemistry

Whole rock geochemistry is concerned with the wt% and ppm abundances of various elements that include major oxides and trace elements, respectively. Various geochemical processes leave their signature on element distributions of the rocks and in order to reveal these, element abundances are plotted on bivariate and trivariate diagrams (Rollinson and Peace, 2021).

Samples were analyzed in Wuhan Sample Solution Analytical Technology using XRF and ICP-MS for major and trace elements, respectively.

Whole-rock chemical compositions were measured at Wuhan Sample Solution Analytical Technology using an XRF. The sample pretreatment of whole rock major element analysis was made by melting method. The flux is a mixture of lithium tetraborate, lithium metaborate and lithium fluoride (45:10:5). Ammonium nitrate and lithium bromide were used as oxidant and release agent, respectively. The melting temperature was 1050 ℃ and the melting time was 15 minutes. ZSX Primus II wavelength dispersive X-ray fluorescence spectrometer (XRF) by RIGAKU, Japan, was used for the analysis of major elements in the whole rock. The X-ray tube is a 4.0KW end window Rh target. Analytical conditions are voltage at 50kV and current at

60mA. All major element analysis lines are kα. The calibration curve was obtained from rock standards GBW07101-14. The data were corrected by theoretical α coefficient method, The relative standard deviation (RSD) is less than 2%. Trace element analyses of whole rocks were conducted on Agilent 7700e inductively coupled plasma mass spectrometer at the Wuhan Sample Solution Analytical Technology.

It is important to note that Loss on Ignition (LOI) is calculated as a first step by heating the sample to ~1000°C to enable escape of volatile phases (e.g., H_2O and CO_2).

2.2 Mineral Chemistry

EPMA allows determination of major oxide abundances (and trace element concentrations with some settings). It is a spot analysis, therefore, it can detect intragrain changes along specified line traverses. It produces particularly good results on major oxides (SiO_2, TiO_2, Al_2O_3, FeO, MnO, MgO, CaO, Na_2O and K_2O) in a very short time. Moreover, it requires simple sample preparation and measurement procedures. This analysis revealed major oxide contents of biotite, plagioclase and titanite, which were used in thermobarometric calculations (e.g., Luhr et al., 1984; Shabani et al., 2003; Uchida et al., 2007; Erdmann et al., 2019; Shellnutt et al., 2020; Eyüboğlu et al., 2021). Moreover, biotite compositions can also be used for source classification (Shabani et al., 2003, Wang et al., 2022) Another strength of EPMA is to acquire back-scattered image (BSE) to create elemental abundance maps. These maps reveal heterogeneities which can be used to interpret variation in crystallization conditions during mineral growth and/or to interpret secondary processes.

Polished sections were carbon-coated to create an electrically conductive surface and measured in AU-EMPA laboratory. AU-EMPA is equipped with JEOL JXA-8600 electron

microprobe with four wavelength dispersive spectrometers (WDS). This allows measurement of four different elements at the same time. *Figure 9* shows a basic sketch of JEOL-8600 Electron Microprobe Analyzer. Electron Microprobe uses an electron gun to create the beam. A filament is heated to emit the electron beam, that is condensed towards the sample holder by condenser lenses. This leads to emission of a characteristic X-Ray from the sample. This X-ray is then focused on an X-ray Spectrometer using a diffractive crystal and elemental abundances are calculated. *Table 1* shows the crystals used for specific element measurements in the context of Bragg's Law. The angle of the crystal relative to the sample is modified for different element measurements. 15kV accelerating voltage and 20nA beam current were used for the instrument settings. 1µm and 5µm beam size were used for biotite and plagioclase, respectively. Matrix corrections for analyses are directly applied by the instrument software.

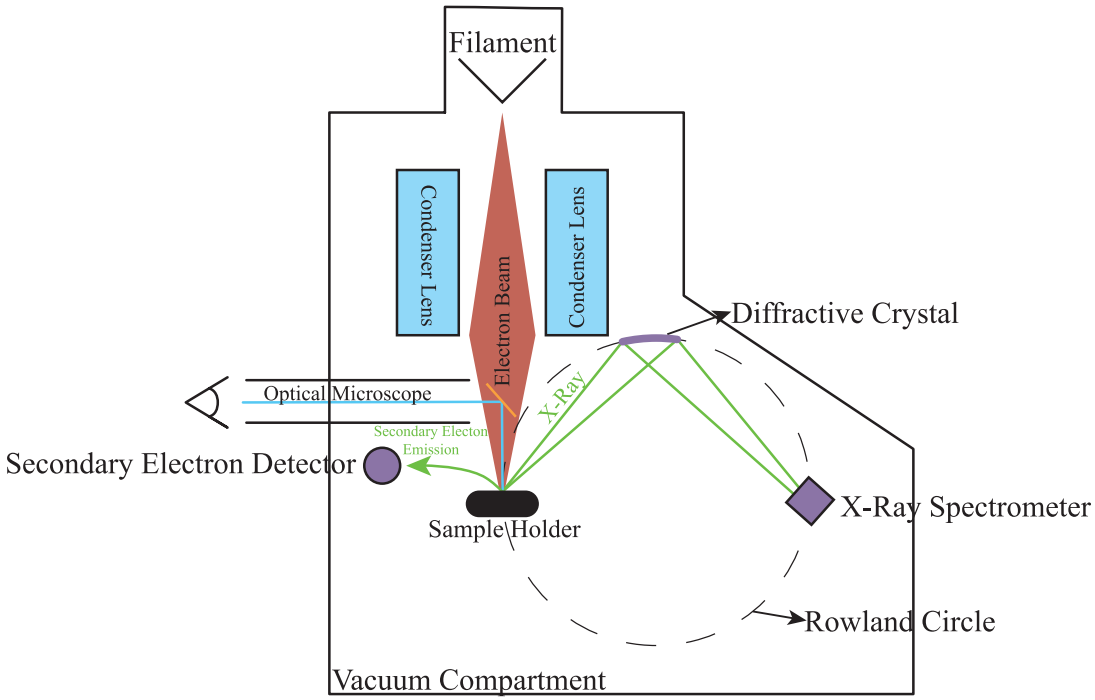

Figure 9: Schematic drawing of JEOL JXA 8600 Electron Microprobe.

Table 1: Measured oxides, used diffractive crystals and standards in AU-EMPA

	TAP1	TAP2	PET	LIF	Standard
Na_2O	X				Amelia Albite
MgO	X				Oliv_2566
Al_2O_3	X				Anorthite
SiO_2		X			Amelia Albite
K_2O			X		Microcline
CaO			X		Anorthite
TiO_2			X		Ilmenite
MnO				X	P-130
FeO				X	Fayalite

Standardization is a vital issue on EPMA and AU-EMPA laboratory has a wide selection of standards that allow representative selection for each target mineral. The method is calibrating all major oxides using a different standard that has a high abundance of that specific oxide. Calibration standards and diffractive crystals used can be seen in *Table 1*. Therefore, it requires moving back and forth between different standards until all the individual major oxide measurements are accurate and precise. Validation standards (that have similar composition with the sample) were measured after 15 to 20 sample measurements for quality assurance/quality control (QA/QC) purposes. For elemental mapping, 2.4μm pixel size and 20msec/pixel dwell was used and provided good results.

2.3 Whole-rock Sr-Nd Isotope Systematics

Cross-plot of $^{87}Sr/^{86}Sr$ (εSr) vs $^{143}Nd/^{144}Nd$ (εNd) isotope ratios is a widely used and accepted method to reveal source magma characteristics and tectonic environment of igneous rocks (Zou et al., 2000; 2010). Unlike major and trace element contents, isotope ratios such as $^{87}Sr/^{86}Sr$ and $^{143}Nd/^{144}Nd$ are not fractionated during partial melting, fractional crystallization and

post crystallization processes, therefore can reflect source characteristics accurately compared to other proxies. Two decay systems are used in this method are:

$$\left(\frac{^{143}Nd}{^{144}Nd}\right)_{measured} = \left(\frac{^{143}Nd}{^{144}Nd}\right)_{initial} + \left(\frac{^{147}Sm}{^{144}Nd}\right)\ \left(e^{\lambda t} - 1\right), \quad \lambda_{147Sm} = 6.54 * 10^{-12}$$

$$\left(\frac{^{87}Sr}{^{86}Sr}\right)_{measured} = \left(\frac{^{87}Sr}{^{86}Sr}\right)_{initial} + \left(\frac{^{87}Rb}{^{86}Sr}\right)\ \left(e^{\lambda t} - 1\right), \quad \lambda_{87Rb} = 1.42 * 10^{-11}\ yr$$

Sr-Nd isotope methods at Wuhan Sample Solution Analytical Technology has been documented in Guo and Zou (2021). Sr isotope method at Auburn University has been briefly documented in Gill et al. (2018) and is described in more details here. AU-ISOLAB is equipped with Finnigan MAT 262 thermal ionization mass spectrometer (TIMS) that has 8 Faraday Cups and a secondary electron multiplier *(Figure 10)*. TIMS ionizes the sample thermally using a filament that is subjected to current. These ions are then accelerated at 10 kV and focused using ion lens towards the magnetic field which separates them based on mass/charge ratio (m/z). Separated ions then go into multiple collectors and multiple isotope ratios are measured simultaneously. TIMS provides very precise results (±0.00001) for elements with high ionization potentials (e.g., Sr and Nd). Isobaric inferences are eliminated by using single element solutions that produce high precision/accuracy results, however, the sample preparation process is complex and time consuming.

Samples are powdered and ~80mg from each one was taken for acid dissolution. Sample dissolution is completed in three stages, each takes place on hot plate and ends with complete evaporation of used acid. The first stage involves 3:1 mixture of 29M HF and 14M HNO_3 and

hot plate treatment at 120 °C for three days. The second stage is dissolution in 6m HCl and direct evaporation at 100 °C, and the last stage is dissolution in 7M HNO_3 and direct evaporation at 100 °C. Lastly, a small amount of 2M HNO_3 is added, and samples are centrifuged for two minutes. Samples in 2M HNO_3 matrix are then ready for column chromatography.

Column chromatography begins with resin cleaning and conditioning, which is followed by sample loading. Sr is eluded using a single stage column through Sr. Spec resin. Nd is eluted in a two staged column, the first stage is elution of LREE using TRU. Spec. This resin holds LREE and then placed on top of Ln. Spec which elutes Nd from other LREE. HNO_3 and HCl with various molarities are used through this process and sample purification is completed. A slightly modified version of methods of Mikova and Denkova (2007) and Li et al. (2012) are used.

Purified Sr samples are picked up from Teflon beakers using dilute (0.25 N) HNO_3 and are mixed with 1 microliter TAPH solution (Zou, 1999; Zou et al., 2000). The mixture is then loaded onto degassed rhenium filaments for ionization. Sr samples on the single thin Re filaments that are dried at 0.7 ampere (A). The filament current is then slowly increased to 2.0 A until all H_3PO_4 is evaporated, and finally is flushed very briefly at 3.0 A. Filaments with Sr samples are then mounted to a sample magazine that can hold up to 13 samples. The magazine is loaded to the ion source of MAT-262. Vacuum in the ion source and mass analyzer of the mass spectrometer is kept at better than 10^{-7} mbar. Purified Sr samples are thermally ionized by passing a current through the filaments in the ion source. An accelerating voltage of 10 KV is used to accelerate Sr^+ ions from the ion source into the magnetic sector mass analyzer. Dynamic jumping mode is used for Sr isotope analyses. Sr isotopic compositions are normalized to $^{86}Sr/^{88}Sr$ of 0.1194. For Nd samples, the process is similar, however Nd ionization requires two

filaments, evaporation and ionization filaments due to its ionization character. Nd isotopic compositions are normalized to $^{146}Nd/^{144}Nd = 0.7219$.

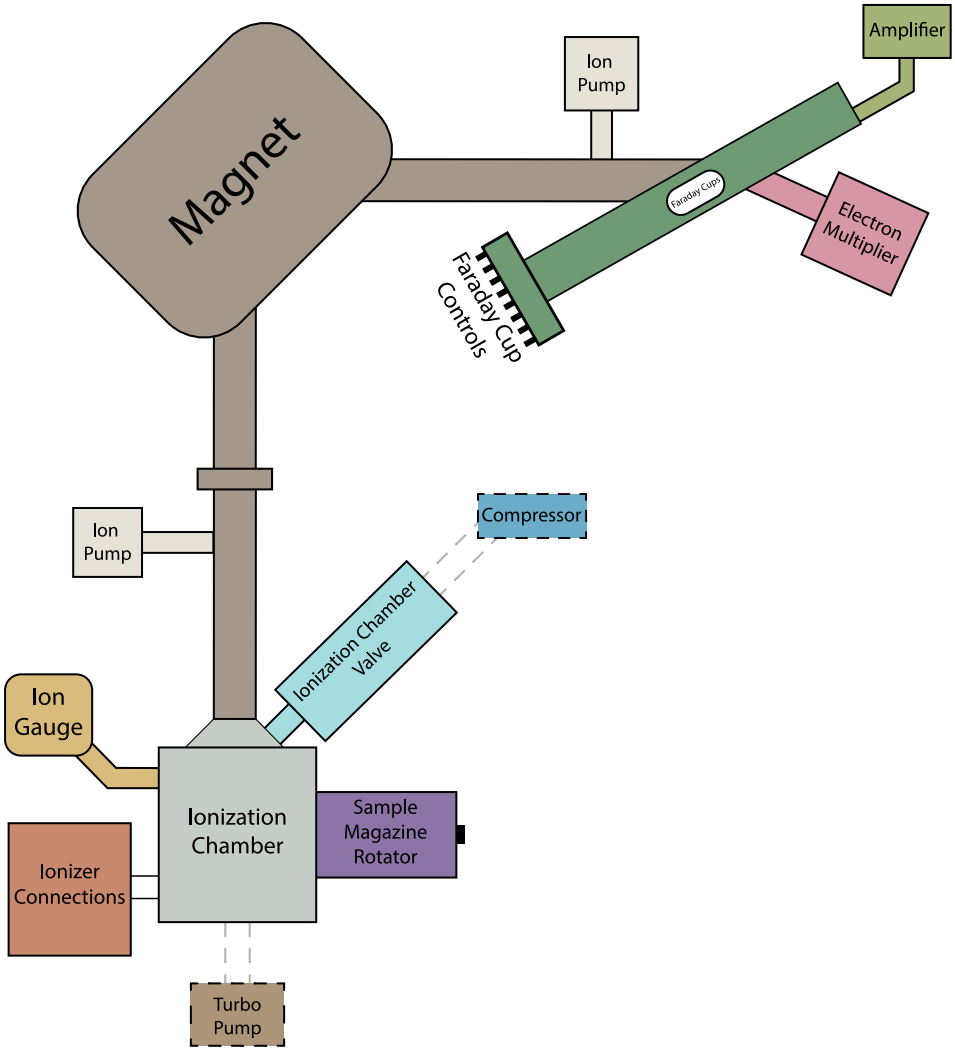

Figure 10: Schematic drawing of Finnigan Mat-262 TIMS

2.4 $^{40}Ar/^{39}Ar$ Geochronology

$^{40}Ar/^{39}Ar$ dating of K bearing mineral phases is a well-established and powerful geo/thermo-chronological method to reveal late/post-crystallization history of plutons. Data from different mineral phases with different closure temperatures can be used to understand the cooling history of the host rock (e.g., Armstrong, 1966; Krol et al., 1996; Kelley, 2002; Schaen et al., 2020). Furthermore, this data will be used in combination with crystallization ages from U-Pb zircon and monazite geochronology from the literature for complete understanding of later stages of evolution of Almond Trondhjemite.

$^{40}Ar/^{39}Ar$ (Merrihue and Turner, 1966) is the modified version of conventional $^{40}K/^{40}Ar$ method. It requires artificial production of ^{39}Ar from ^{39}K by neutron bombardment in a nuclear reactor. The fraction of produced ^{39}Ar from ^{39}K is monitored with flux monitors that are placed among samples, therefore initially present ^{40}K can be calculated entirely from Ar measurements (through so called "J value"), allowing measurement of both radiogenic and radioactive isotopes as a single aliquot in the same mass spectrometer (Clauer et al., 2013). More in-depth comparison of these two techniques can be found in Dalrymple and Lanphere (1971) and McDougall and Harrison (1999). Equations of J value and cooling age are:

$$J = \frac{e^{\lambda t_{monitor}} - 1}{\left(\frac{^{40}Ar}{^{39}Ar}\right)_{monitor}},$$

$$t = \frac{1}{\lambda} * \ln\left(\frac{^{40}Ar}{^{39}Ar} * J + 1\right)$$

$$\lambda = 5.463 \pm 0.107 \times 10^{10}\ yr^{-1}\ (Min\ et\ al., 2000)$$

Dates acquired by $^{40}Ar/^{39}Ar$ analysis may directly represents crystallization age for fast cooling volcanic rocks or low temperature systems, however, this is not the case for intrusive rocks. For intrusive rocks, there is generally a lag between crystallization and cessation of Ar diffusion (closure) in minerals because of high diffusibility of Ar and relatively slow cooling of these rocks. Therefore, determined age represents closure age of the mineral (Schaen et al., 2020). Muscovite was used in the study and its nominal closure temperature is ~390 C° (Grove and Harrison, 1996). Although closure temperature is a point, there is a range of temperature that transition from open to closed system occurs, and this varies with crystal size, diffusion geometry factor and cooling rate (Dodson, 1973).

Five samples were crushed, sieved and monomineralic muscovite grains were hand-picked from these and were loaded to irradiation disks to be sent to the USGS TRIGA Nuclear Reactor for irradiation with fast neutrons. Samples were irradiated for 16 hours with Cd shielding. The monitor to calculate J value was Fish Canyon sanidine (28.201 ± 0.046 Ma, Kuiper et al., 2008) and GA1550 Biotite (99.44 ± 0.17 Ma, Jourdan and Renne, 2007). Irradiated samples were then unpacked and measured in Auburn Noble Gas Isotope Mass Analysis Laboratory (ANIMAL). ANIMAL houses the GLM-110 *(Figure 11)* which is a 400cc volume, 90° magnetic sector mass spectrometer with 10 cm radius of curvature and a single electron multiplier detector. The extraction line is equipped with a 60W Synrad CO_2 laser for sample fusion/heating. Blanks were measured following every 5^{th} analysis. Blank corrections to ^{36}Ar measurements are based on an average or regression of several blanks measured for a given day of analysis. Air aliquots were typically analyzed 5 times per day to monitor mass discrimination,

generally at the beginning of the day. Data were reduced using an Excel spreadsheet and Isoplot (Ludwig, 2012).

Single crystals were first subjected to total fusion with total of 10 single crystals for each sample. In addition, one grain from each sample was used for step-heating measurements. Step heating releases argon isotopes incrementally as the laser power increases with every step until the sample degasses completely and fuses. When consecutive steps yield results that are statistically identical, they define a plateau age.

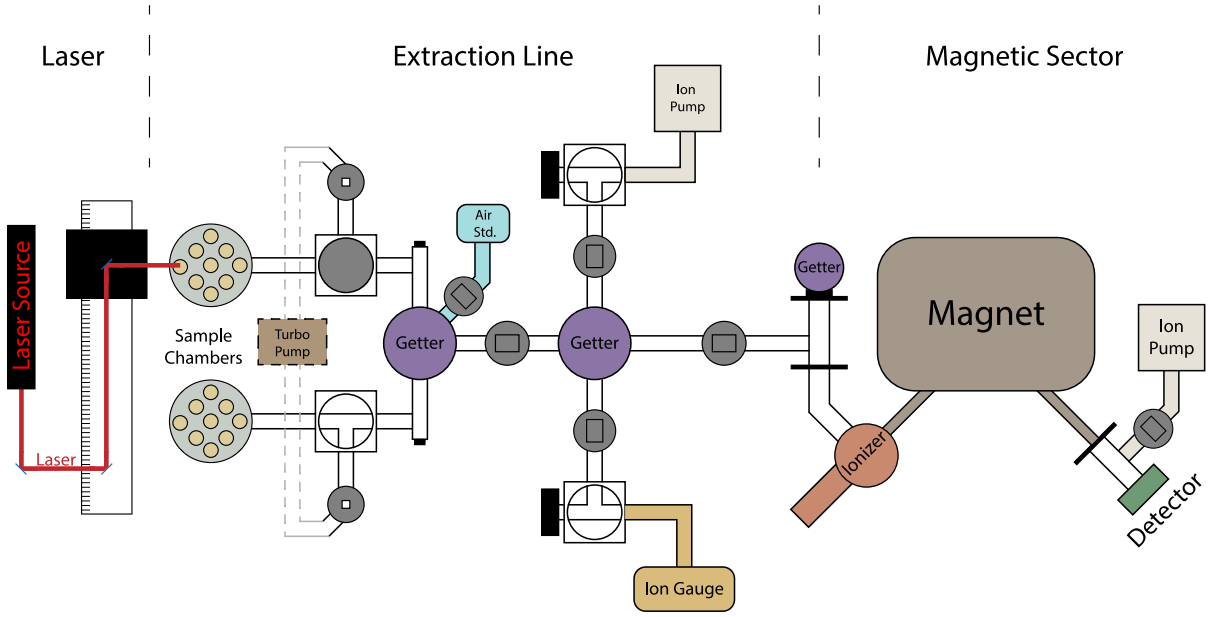

Figure 11: Schematic illustration of GLM-110 in ANIMAL.

3. Results

3.1 Petrography

AMD and AT samples show similar mineralogical and textural characters on their respective groups. Both groups are dominated by plagioclase and quartz. There are minor amounts of K-feldspar present in AMD samples, but these are even less in AT samples. All samples appear to be slightly deformed and show an intermediate/weak foliation that is primarily defined by mica assemblages. A number of garnet grains were observed on an AMD-3 thin section *(Figure 12)*, however, the garnets seem to not appear in polished sections that EPMA work was done on. In AMD samples, intermediate/weak foliation is defined by mainly muscovite-biotite micas, and trace amount of apatites. Muscovite seems to dominate the mica assemblage, rather than biotite. Quartz in AMD-1 and AMD-3 show polycrystalline texture which also indicates deformation. Zircon is present as disseminated and fine grained. AMD-3 also asymmetrically deformed mica formation *(Figure 12, green inlet)* and epidote replacement in these deformed micas. Trace amounts of secondary epidote replace micas on cleavage planes. AT samples have more biotite in foliation planes compared to AMD samples. Scarce epidote formation as cumulates is also seen on these, but no garnet has been observed *(Figure 13)*. This might be due to the general low abundance of garnet in the Almond Trondhjemite. AT-1 and 2 show cross-joints which are filled by fine grained muscovite micas and epidotes(?). These cross-joints look like cleavage planes on some plagioclases and make them appear as hornblende, however no hornblende was found in any of these samples, by optic microscopy or EPMA. Zircon morphology is similar to AMD samples, but no apatite was observed in AT samples. Although it was not detected in thin section petrography, presence of titanite as an accessory phase was confirmed using EPMA. A small amount of secondary calcite fillings was observed in

all the samples. Epidote grains are not euhedral, and their abundance is slightly higher in AT-1,2 samples, compared to AMD-2,3 samples.

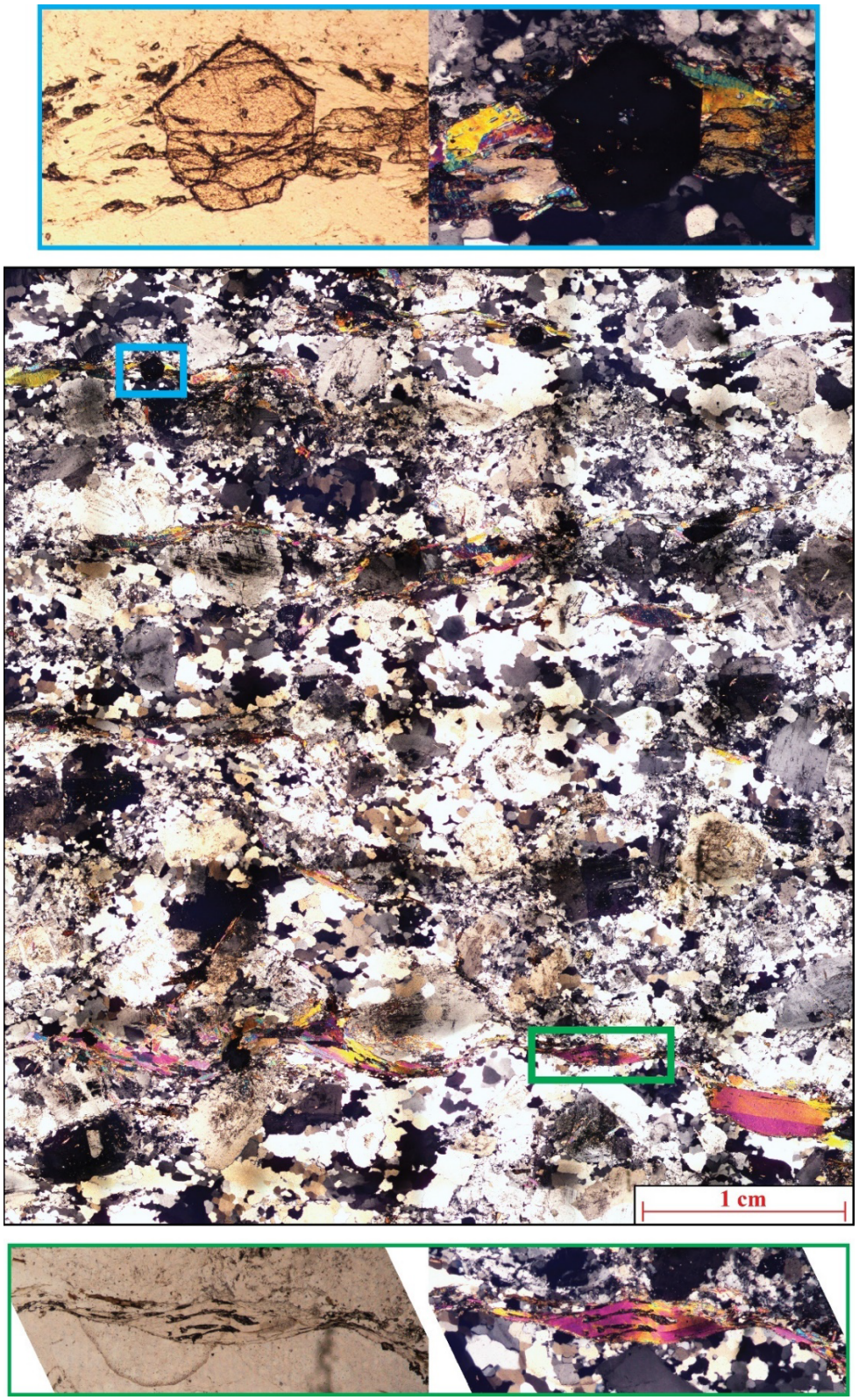

Figure 12: Photomicrograph of AMD-3. Blue inlet shows a garnet on foliation plane and green inlet shows a deformed mica with epidote replacing muscovite.

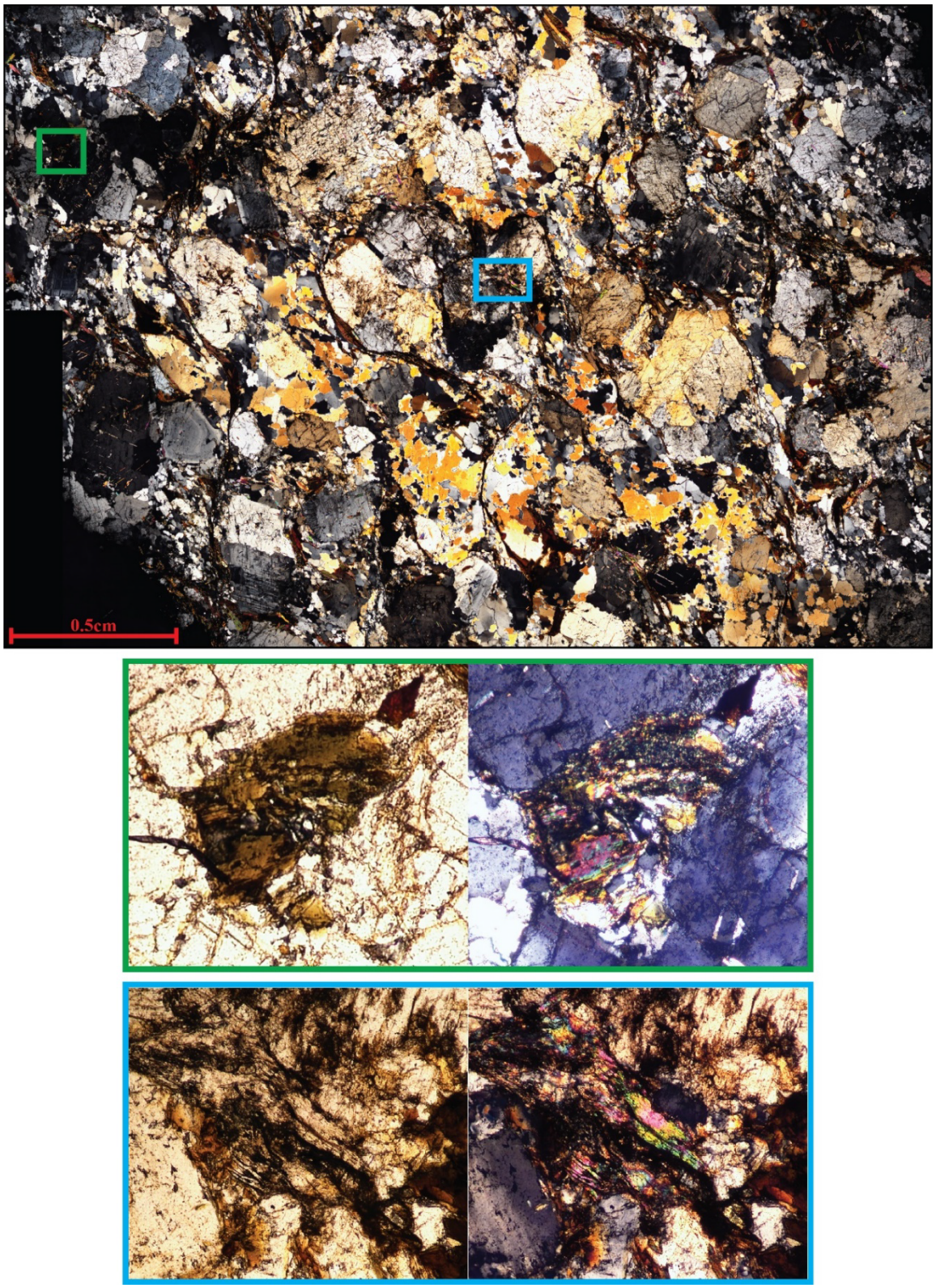

Figure 13: Photomicrograph of AT-1. Both inlets show epidote replacing micas along cleavage planes.

3.2 Whole Rock Geochemistry

3.2.1 Evaluation of Sample Quality

Sample freshness is a general concern/problem in Southern Appalachian studies, as discussed earlier. This makes it imperative to assess the collected data before using it. To evaluate the data, Loss on Ignition (LOI) is used. It is expected to be smaller than 1% for 'Dry' samples, those that are poor in hydrous phases such as amphibole group minerals. The expected 'Total' values for these samples are 99-101% (*Rollinson and Pease, 2021*). All samples show suitable LOI values with 0.99%, 0.73%, 0.55% and 0.79%, and totals of 100.2%, 99.96%, 101.18% and 100.07%, respectively.

3.2.2 Major Oxides

Samples have high silica contents ranging between 70.48 and 74.81 wt.% with minor/trace amounts of TiO_2 (0.07-0.29%), tFe_2O_3 (0.58-1.95%), MnO (0.022-0.039%) and MgO (0.14-0.74%). All of the samples have a relatively high ~15% Al_2O_3 content. A homogeneous distribution of major oxide content is observed in three samples. However, relatively more silica-rich (74.81%) AMD-3 has relatively less Mg, Al and Ca oxide contents and contains more Na and K oxides, which indicates it is slightly more evolved *(Figure 14,Table 2)*.

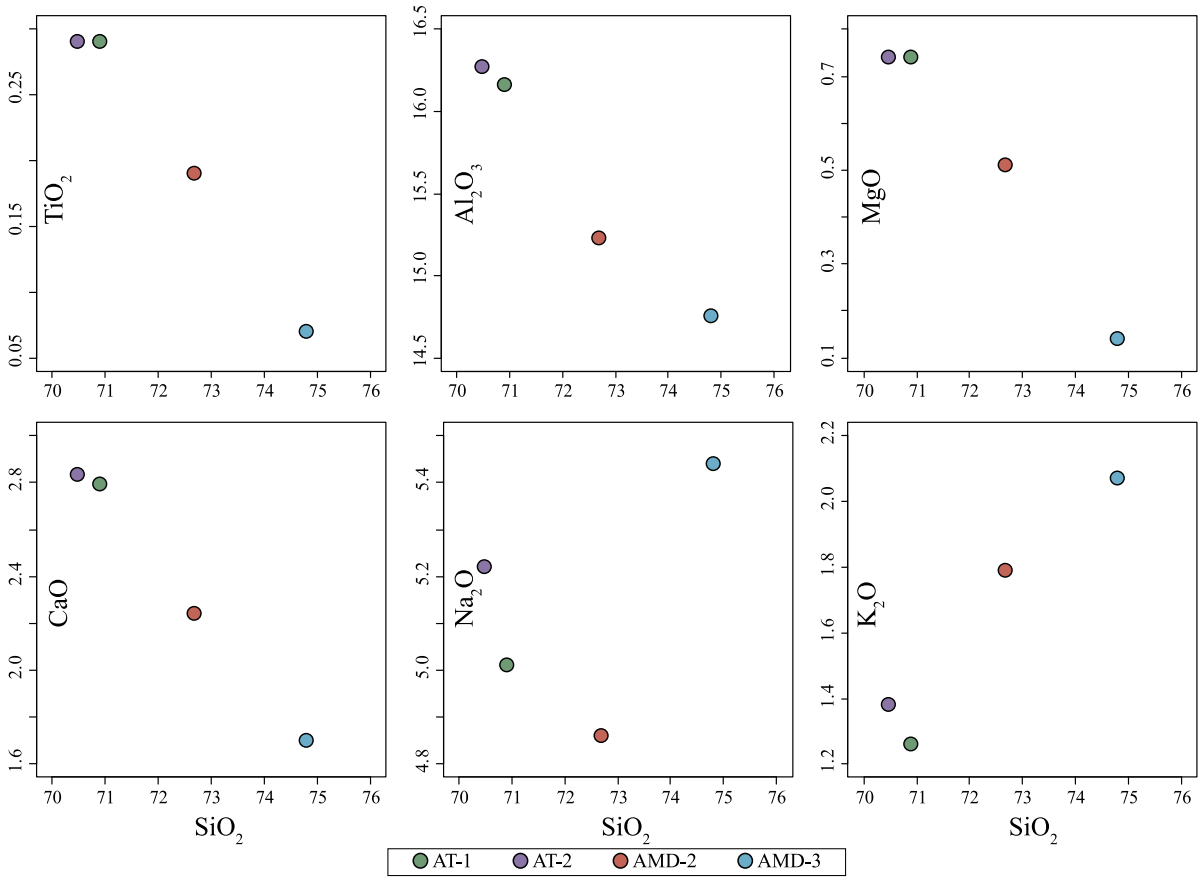

Figure 14: Bivariate diagrams of major oxide contents against silica content.

3.2.3 Trace Elements

Trace element distribution among samples is relatively homogeneous *(Table 2)*. Sr and Y abundances change between 468-574ppm and 5.45-8.33ppm, respectively and Sr/Y ratios are between 56.2 and 132.3. All samples have systematically low Ta, Yb and Nb abundances, 0.15-0.21ppm, 0.47-0.58ppm and 1.93-2.93ppm, respectively. Cr and Ni contents are in the lower side. For the less evolved, lower silica samples (AT-1 and AT-2) Cr and Ni abundances are ~11.9 and ~5.8ppm, respectively. By comparison, the more evolved, higher silica samples have lower Cr (1.50-3.85ppm) and lower Ni (0.84-2.24ppm).

Table 2: Whole rock major oxide (wt.%) and trace element contents (ppm) of the AT.

	AT-1	AT-2	AMD-2	AMD-3
SiO_2	70.91	70.48	72.69	74.81
TiO_2	0.29	0.29	0.19	0.07
Al_2O_3	16.16	16.27	15.23	14.75
TFe_2O_3	1.95	1.94	1.67	0.58
MnO	0.03	0.03	0.04	0.02
MgO	0.74	0.74	0.51	0.14
CaO	2.79	2.83	2.24	1.70
Na_2O	5.01	5.22	4.86	5.44
K_2O	1.26	1.38	1.79	2.07
P_2O_5	0.07	0.07	0.07	0.06
LOI	0.99	0.73	0.79	0.55
TOTAL	**100.20**	**99.96**	**100.07**	**100.18**
Li	21.30	19.10	24.20	20.20
Be	1.17	0.99	1.28	1.53
Sc	3.52	3.83	2.54	1.50
V	31.30	32.80	14.20	5.54
Cr	11.90	11.80	3.85	1.50
Co	4.89	4.59	2.15	0.66
Ni	5.93	5.72	2.24	0.84
Cu	8.71	8.87	3.02	5.52
Zn	38.30	40.90	39.30	24.40
Ga	18.60	19.40	17.90	17.30
Rb	39.70	33.80	41.50	49.50
Sr	552.00	574.00	468.00	527.00
Y	6.07	4.34	8.33	5.45
Zr	116.00	118.00	124.00	70.20
Nb	2.55	2.42	2.93	1.93
Sn	0.82	0.92	1.37	1.55
Cs	0.70	0.69	0.79	0.68
Ba	391.00	453.00	456.00	393.00
La	7.55	5.94	10.50	5.07
Ce	17.30	12.70	22.50	10.70
Pr	1.87	1.46	2.68	1.29
Nd	7.34	5.67	10.30	5.45
Sm	1.65	1.23	2.05	1.23
Eu	0.59	0.49	0.49	0.34
Gd	1.44	1.11	1.59	1.30
Tb	0.20	0.16	0.23	0.20
Dy	1.18	0.85	1.28	0.93
Ho	0.24	0.17	0.23	0.19
Er	0.65	0.42	0.65	0.47
Tm	0.08	0.06	0.09	0.07
Yb	0.56	0.46	0.58	0.47
Lu	0.08	0.07	0.09	0.06
Hf	3.10	3.07	3.29	2.31
Ta	0.16	0.15	0.21	0.21
Tl	0.20	0.23	0.24	0.25
Ti	1738.07	1738.07	1138.73	419.53
Pb	10.10	9.97	13.10	16.80
Th	1.73	1.45	2.84	1.56
U	0.58	0.64	0.65	0.58

Trace elements are normalized to and plotted against primitive mantle values of Sun and McDonough (1989), and REE are normalized to and plotted against primitive mantle values of McDonough and Sun (1995) in *Figure 15a and b*, respectively. In primitive mantle normalized diagram REE diagram, light rare earth elements (LREE) are enriched, without significant Eu anomalies. Heavy rare elements (HREE) make up a relatively flat pattern. In primitive mantle normalized multi-element diagram, samples have strongly positive K, Pb, Sr and Li anomalies, as well as negative Nb, Ta and Ti anomalies. Zr and Hf are also weakly enriched.

3.2.4 Classification and Tectonic Discrimination

Trace elements and REE were mostly not mobilized in samples, as shown by linear trends of immobile-mobile element pairs discussed earlier. Therefore, tectonic diagrams using these elements are safe to use. Samples have peraluminous characteristics according to Shand (1943) classification diagram with A/CNK index of 1.0-1.1. This suggests I-type characteristics with one sample (AT-1) on the I-S Type boundary. Aal samples plot in TTG/adakite field in La-Yb classification diagram of Martin (1986). To summarize, the AT is an I-type peraluminous trondhjemite. Lastly, all the samples fall into trondhjemite zone in feldspar-based classification of O'Connor (1965) *(Figure 16a, b and c, respectively)*.

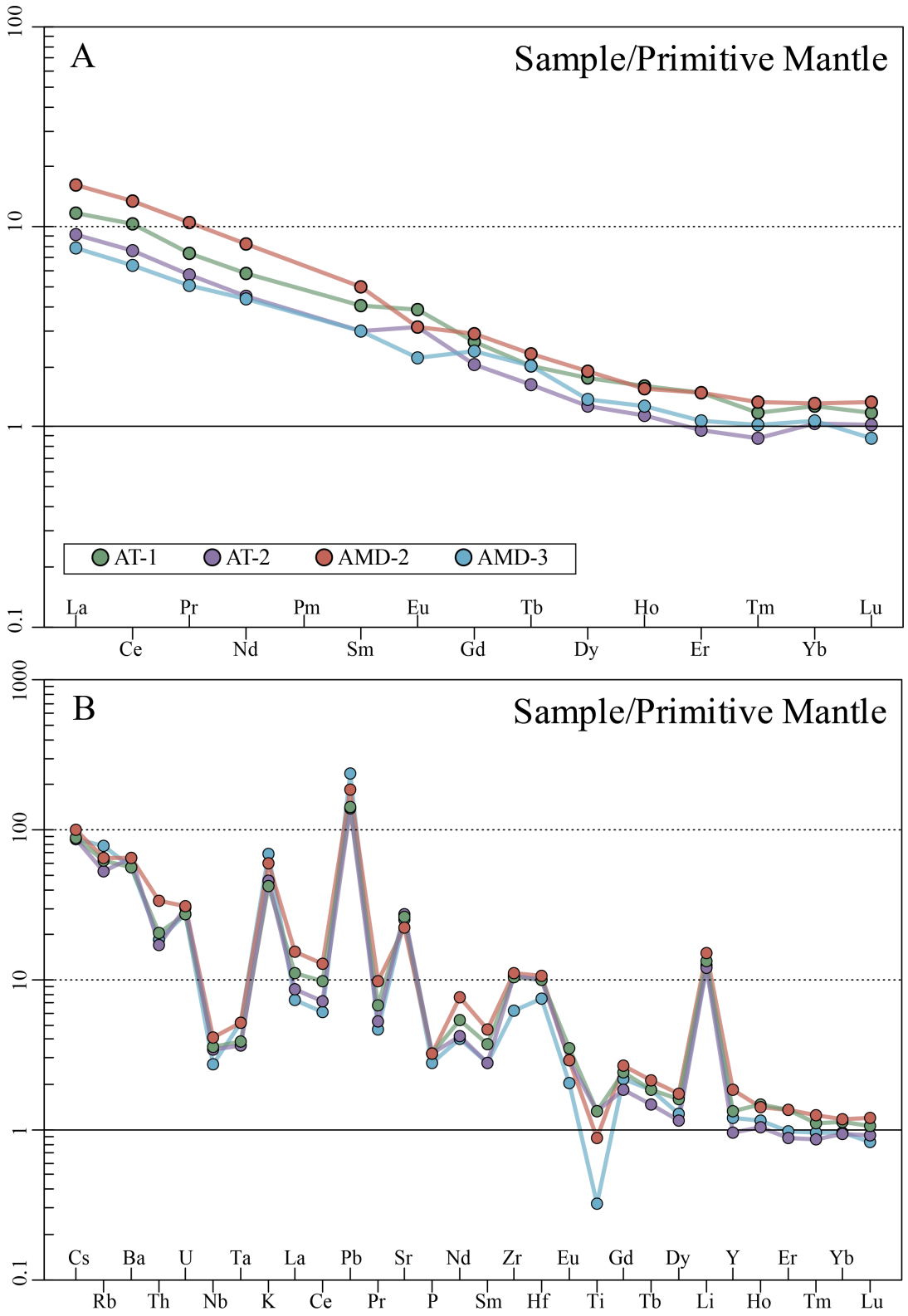

Figure 15: Primitive mantle normalized trace element and REE diagrams for the AT. *(Sun and McDonough 1989; McDonough and Sun, 1995).*

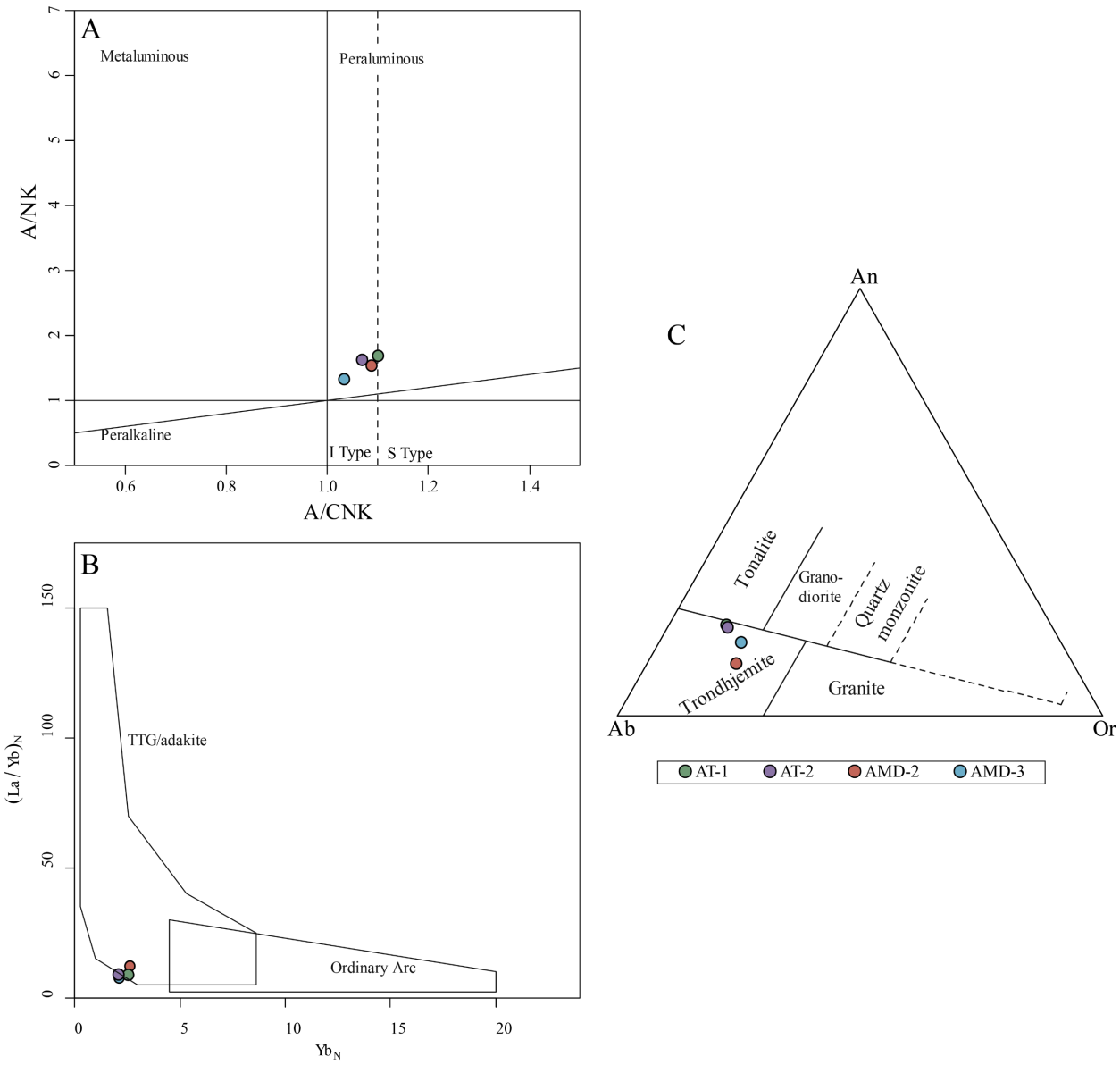

Figure 16: Discrimination diagrams for the AT. A) Shand, 1943. B) Martin, 1986. C) O'Connor, 1965.

3.3 Mineral Chemistry

EPMA was done on biotites, muscovites, plagioclases and titanites of three samples and mineral formulas were calculated for each element using oxide weight percentages. The focus of this manuscript is on biotite and plagioclase because of their usefulness in constraining magmatic

conditions. Moreover, titanite geobarometer results did not yield desired precession, hence excluded. 1771 point-measurements were done on biotite and plagioclase combined, including samples and standards. Data reduction was done according to total dry oxide percentages for each mineral as well as expected ranges for each oxide *(Table 3)*. For QA/QC, after every 15 to 20 sample points, standards were measured to assure the calibration was still good and recalibration was done if needed. Validation was done by one final QA/QC measurement between calibration and sample measurements and recorded to show accuracy of the data. *Table 4* shows the mean value of QA/QC measurements and expected values.

Table 3: Summary of biotite and plagioclase EPMA measurements.

	Total Measurements	Accepted Total % Range	Valid Measurements	QA/QC
Biotite	648	93.0-98.6	182	30
Plagioclase	1123	99.0-101.0	380	35
Σ	**1771**		**562**	**65**

Table 4: QA/QC outline for EPMA.

	Biotite13 Known	QA/QC Measurements	Amelia Albite Known	QA/QC Measurements
SiO_2	33.1	33.33	68.14	67.93
TiO_2	1.3	1.39	0	0
Al_2O_3	17.65	17.55	19.77	20.3
FeO	31.47	31.52	0.01	0.03
MnO	0.04	0.04	0	0.01
MgO	2.82	2.93	0	0
CaO	0.1	0.02	0.38	0.21
Na_2O	0.12	0.17	11.46	11.19
K_2O	9	9.12	0.23	0.15
Σ	**95.6**	**96.08**	**99.99**	**99.83**

Reduced data was used to calculate mineral formulas. Empirical mineral formulas used are:

Biotite → $K_2(Fe,Mg)_6(Al,Si_3)_2O_{12}(OH)_2$-$H_2O$ (22 Oxygens)
Plagioclase → $Na_2Ca_2Si_{12}Al_4O_{32}$ (32 Oxygens)

Calculated plagioclase compositions are mostly oligoclase with some showing albitic composition *(Figure 17)*. High number of measurements was done on plagioclases using line traverses and very weak compositional zoning is observed in some crystals (An content varies by ~5%).

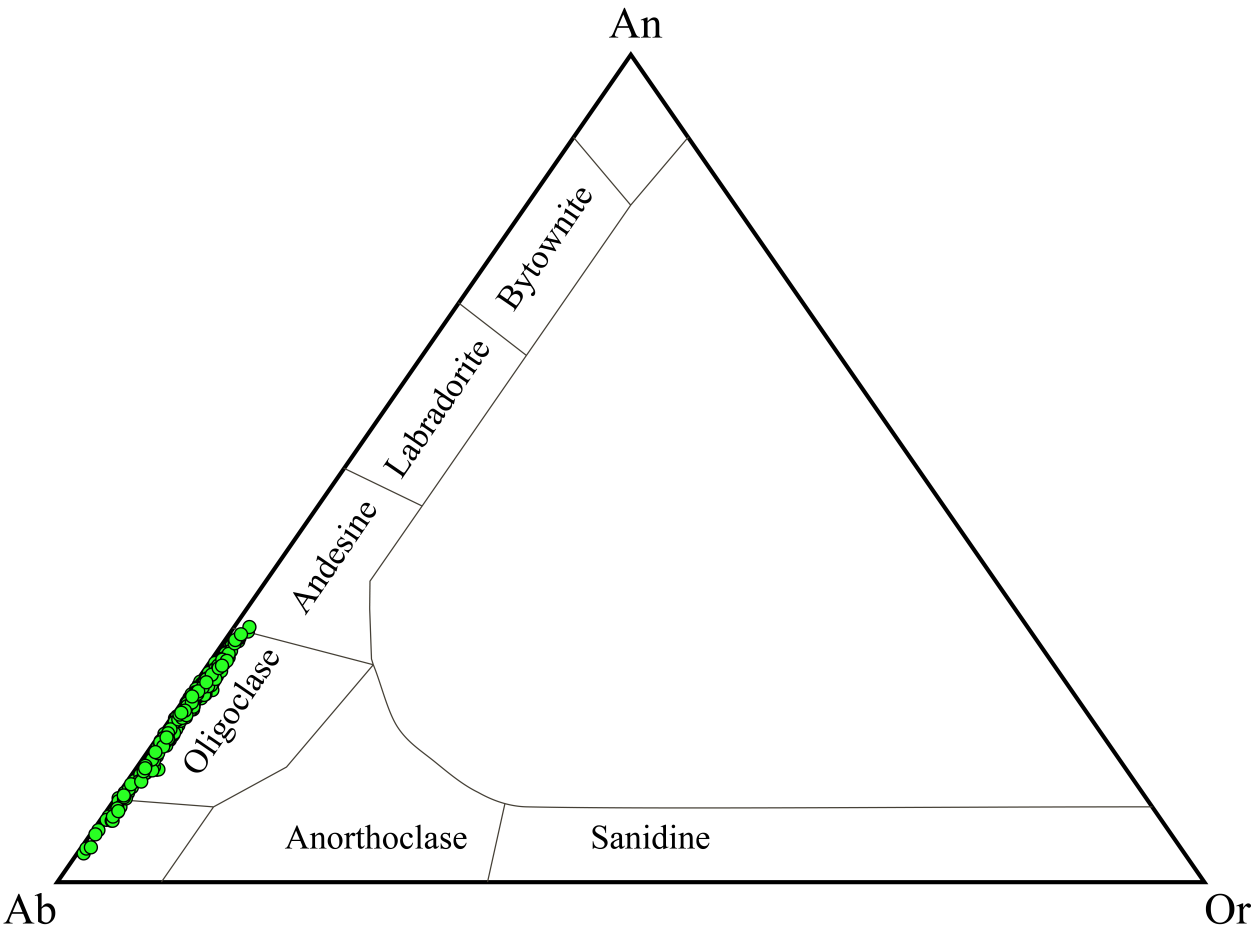

Figure 17: Plagioclase compositions of the AT.

Biotites of AT have ferribiotite-annite character *(Figure 18a)* and their crystallization temperatures were calculated using equation of Luhr et al. (1984). Calculated temperatures have a mean value of 630±24 (1σ) °C *(Figure 18b)*. These values are relatively low for expected biotite crystallization, and this can be explained by repeated cycles of heating and H_2O flux (Challener and Glazner, 2017: Shellnutt et al., 2020). Biotite can also be used as a geobarometer using the equation of Uchida et al. (2007). This geobarometer was calibrated using hornblende and sphalerite geobarometers. Calculated pressures were used to calculate a crystallization depth, assuming a uniform average crustal density of 2.8g/cm^3 and the results yield mean depth of 14.1 ±2.3(1σ) km *(Figure 18b and Appendix B)*. For titanite, measurements did not yield any reliable results as the standard deviation was much greater than desirable. I think this is related to the newly developing nature of this geobarometer and it needs more calibration with natural and experimental confirmation (Erdmann et al., 2018).

$$T\ (C°) = \frac{838}{1.0337 - \frac{Ti}{Fe^{2+}}}$$ (Luhr et al., 1984)

$$P\ (kbar) = 3.33 * Al^T - 6.53\ (\pm 0.33)$$ (Uchida et al., 2007)

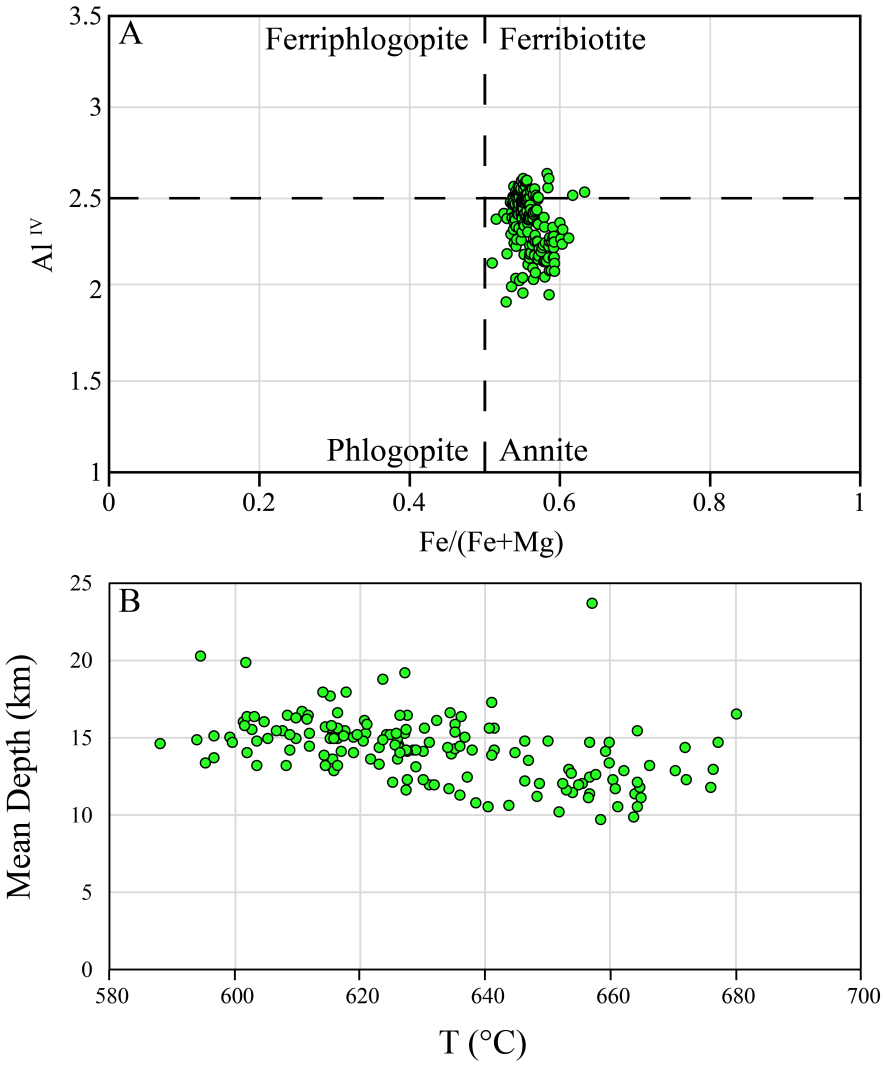

Figure 18: Crystallization temperatures and depths of biotites from the AT A) Calculated with equation of Luhr et al., 1984. B) Calculated with equation of Uchida et al. (2007) and average crustal density of 2.8g/cm^3.

BSE images were taken for elemental mapping. *Appendix C* shows BSE image and element abundance maps for four different elements. It is important to note that color scales are unique to each map, and do not show abundance relative to one another. Quartz and plagioclase are the most abundant minerals as expected. Biotite and muscovite follow these in terms of abundance. In the BSE image, one muscovite crystal is marked with an asterisk (*). This crystal

shows no cleavage because it was cut along the cleavage plane. It is inferred as muscovite because of its elemental compositions. The small mineral in the top portion has a very high Al abundance and low Fe, K and Mg abundance and it is topaz. All biotites and plagioclases, regarding their different morphologies, show relatively homogeneous distribution of elements.

3.4 Sr-Nd Isotope Geochemistry

$^{87}Sr/^{86}Sr$ and $^{143}Nd/^{144}Nd$ ratios were measured as 0.705862-0.707167 and 0.512366-0.512439, respectively *(Table 5)*. It should be noted that these data are robust as evidenced by significantly small 2σ values as shown in the same table.

Table 5: Result of Sr-Nd isotope analysis.

	($^{87}Sr/^{86}Sr$)	**2σ**	**($^{143}Nd/^{144}Nd$)**	**2σ**
AT-1	0.705862	0.000010	0.512400	0.000006
AT-2	0.705720	0.000009	0.512425	0.000006
AMD-2	0.706719	0.000007	0.512366	0.000005
AMD-3	0.706225	0.000008	0.512439	0.000008
AMD-1	0.707167	0.000011		

After the measurements are done, initial values for these isotopic ratios should be calculated using the age of the rock, natural abundances of different isotopes of Rb, Sr, Sm and Nd elements, as well as abundances (in ppm) of these elements in subject rocks. The former is taken from the measured whole rock trace and REE data. The latter is taken from The Commission on Isotopic Abundances and Atomic Weights (CIAAW) of International Union of Pure and Applied Chemistry (IUPAC) (Meija et al., 2013) *(Table 6)*. The age of this intrusion is taken as 340Myr (Stowell et al., 2019) for all calculations.

Table 6: Atomic masses and abundances used in calculation of Sr-Nd isotopes, from Meija et al., (2013).

λ_{Rb-Sr}	$1.42*10^{-11}$
Age	340 Myr
$(^{87}Rb/^{86}Sr)_{BE}$	0.7048
$(Rb/Sr)_{BE}$	0.03

	Mass	**Abundance**
^{85}**Rb**	84.91179	0.721654
^{87}**Rb**	86.90918	0.278346
A.W.	85.4678	

	Mass	**Abundance**
^{84}**Sr**	83.91343	0.005574
^{86}**Sr**	85.90926	0.098566
^{87}**Sr**	86.90888	0.070015
^{88}**Sr**	87.90561	0.825845
A.W.	87.62	

	Mass	**Abundance**
^{142}**Nd**	141.9077	0.27153
^{143}**Nd**	142.9098	0.12173
^{144}**Nd**	143.9101	0.23798
^{145}**Nd**	144.9126	0.08293
^{146}**Nd**	145.9131	0.17189
^{148}**Nd**	147.9169	0.05756
^{150}**Nd**	149.9209	0.05638
A.W.	144.242	

λ_{Sm-Nd}	$6.54*10^{-12}$
Age	340 Myr
$(^{147}Sm/^{144}Nd)_{CHUR}$	0.512638
$(Sm/Nd)_{CHUR}$	0.1966

	Mass	**Abundance**
^{144}**Sm**	143.912	0.03078
^{147}**Sm**	146.9149	0.15004
^{148}**Sm**	147.9148	0.11248
^{149}**Sm**	148.9172	0.13824
^{150}**Sm**	149.9173	0.07365
^{152}**Sm**	151.9197	0.2674
^{154}**Sm**	153.9222	0.22741
A.W.	150.36	

Using these, $(^{87}Sr/^{86}Sr)_i$ and $(^{143}Nd/^{144}Nd)_i$ were calculated and the results can be seen in *Table 7*. By tradition, $^{143}Nd/^{144}Nd$ data is shown as εNd_i, which requires normalization to Chondrite Uniform Reservoir (CHUR) value of the same age. These values were calculated and presented on *Table 7*, using $(^{143}Nd/^{144}Nd)_{CHUR} = 0.512638$ and $(^{147}Sm/^{144}Nd)_{CHUR} = 0.1966$ (Bouvier et al., 2008).

Table 7: Initial Sr-Nd values for the AT.

	AT-1	AT-2	AMD-2	AMD-3
$^{87}Sr/^{86}Sr$	0.7058620	0.7057200	0.7067190	0.7062250
$^{87}Rb/^{86}Sr$	0.2082635	0.1707029	0.2565759	0.2719683
$(^{87}Sr/^{86}Sr)_i$	**0.7053984**	**0.70534**	**0.7054773**	**0.7056196**
$^{143}Nd/^{144}Nd$	0.5124000	0.5124250	0.5123660	0.5124390
$^{144}Nd/^{147}Sm$	0.1361971	0.1308731	0.1206573	0.1368166
$(^{143}Nd/^{144}Nd)_i$	**0.5124000**	**0.5124250**	**0.5123660**	**0.5124390**
$(^{143}Nd/^{144}Nd)_{CHUR,i}$	0.5120968	0.5121337	0.5120974	0.5121344
εNd_i	**-1.89**	**-1.17**	**-1.88**	**-1.16**
T_{DM}	**1.26**	**1.13**	**1.11**	**1.19**

εNd ages of the AT were also calculated to identify crustal residency time. This calculation assumes (nearly)-constant $^{147}Sm/^{144}Nd$ ratios because of their similar atomic structure and reveals last time the sample was in equilibrium with the mantle reservoir. This reservoir is selected as depleted mantle of DePaolo (1981) and the calculated age is T_{DM}. Bea et al. (2023) discussed this technique is susceptible to error, especially in high silica, peraluminous granitoids. The potential error occurs because these granitoids are susceptible to changes in $^{147}Sm/^{144}Nd$ through fractionation of monazite, xenotime, apatite and garnet. Low $^{147}Sm/^{144}Nd$ ratios (<0.08) yield anomalously low T_{DM} ages, whereas high $^{147}Sm/^{144}Nd$ ratios (>0.165) yield anomalously high T_{DM} ages (Stern, 2002) and two-stage T_{DM} calculation (DePaolo, 1991) should be used to attenuate these errors. For the AT, $^{147}Sm/^{144}Nd$ ratio changes between 0.121 and 0.137, which are suitable for one-step T_{DM} calculation. Calculated values are given in *Table 7 and Figure 19*.

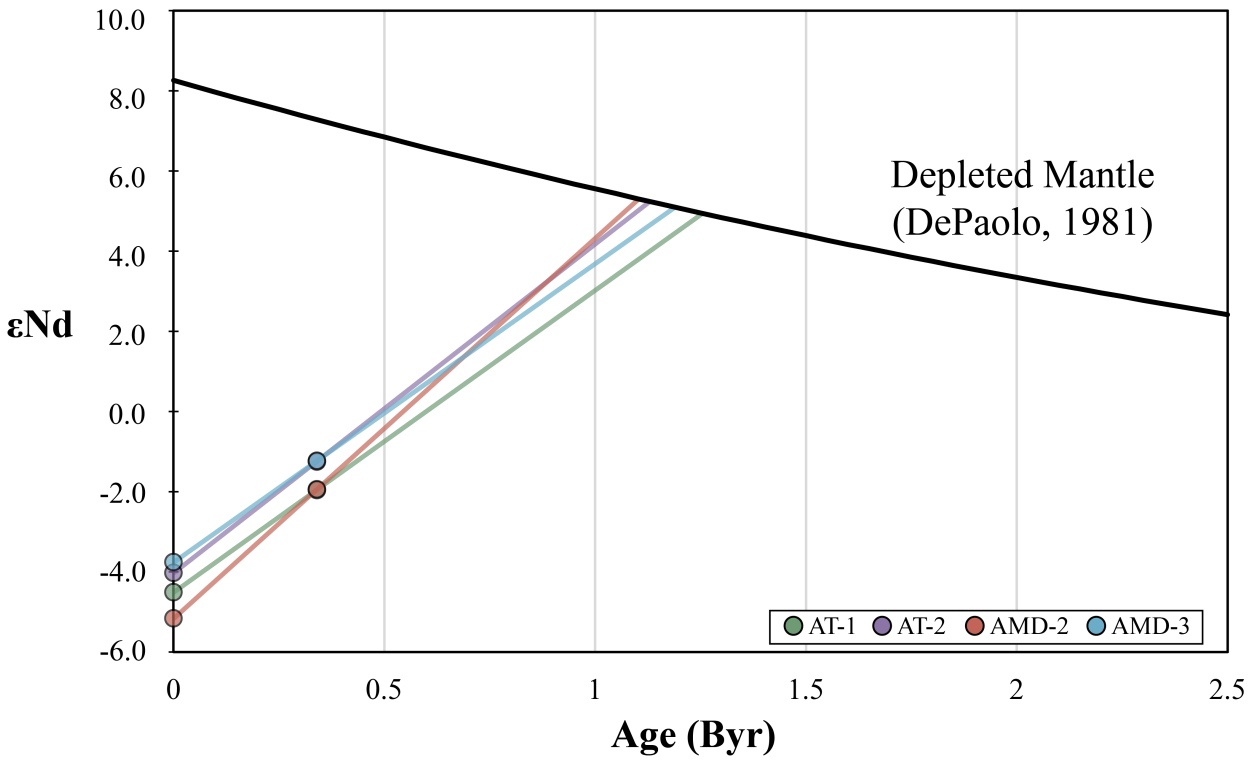

Figure 19: Single-step T_{DM} ages for the AT.

3.5 $^{40}Ar/^{39}Ar$ Thermochronology

$^{40}Ar/^{39}Ar$ step heating and total fusion ages are presented in *Figure 20* a *to e and f*, respectively and the full data can be seen in *Appendix D*. In step-heated samples, plateau ages were defined with a slightly modified version of criteria suggested by Schaen et al. (2020). Used criteria are: 1) at least three consecutive steps that with each other in 1σ error, 2) plateau steps should include at least 60% of total extracted ^{39}Ar gas. Box heights are 1σ for step-heating and all ages are given in 2σ error.

Step-heated muscovite samples yield consistent plateau ages of 317-320 Ma for AT-1, 2 and AMD-1 samples and slightly older 321-322 Ma for AMD-2 and 3. AMD-3 shows excess ^{40}Ar in the first couple of steps. The excess argon is likely to result from argon retention in lattice defects that are results of deformation (Cosca et al., 2011), similar to the deformed mica in *Figure 12*. In the histogram of single crystal total fusion ages *(Figure 20f)*, muscovite ages cluster around 320Ma and they are consistent with step-heating results. The younger peak observed in AT-2 muscovites (~140Mya) attributed to "less radiogenic" sample (as explained in Hames, 2020). When the ^{39}Ar signal is too low compared to ^{36}Ar, applied atmospheric correction may yield erroneous ages (Appendix D).

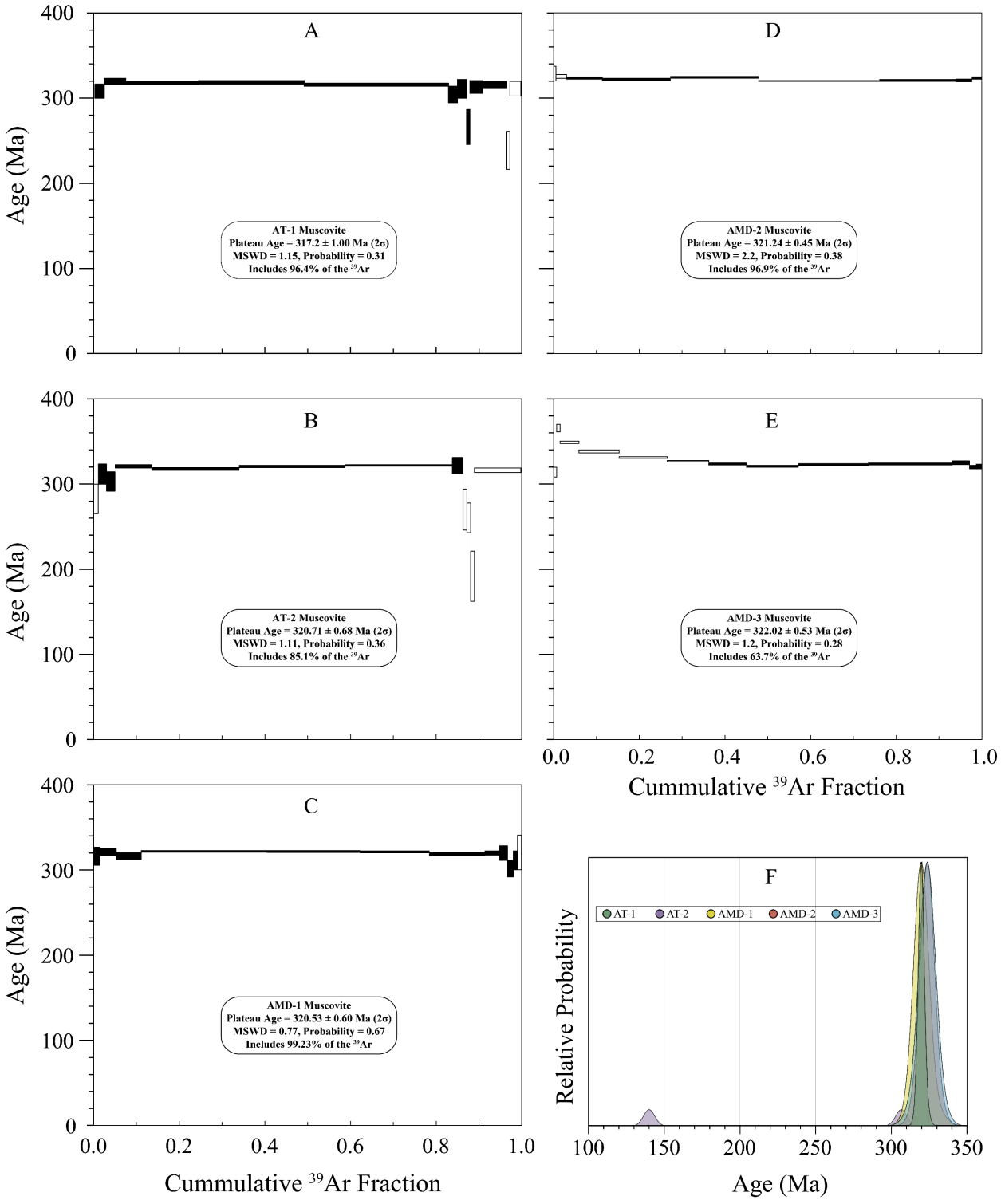

Figure 20: Results of muscovite $^{40}Ar/^{39}Ar$ step heating (A-E) and total fusion (F) ages.

4. Discussion

4.1 Petrogenesis

For discussion, data from eleven papers which contain 188 data points in total were selected to be plotted against the AT in a number of diagrams. During this selection, care was taken to evaluate the data quality of said papers. Another criterion was to be published in top journals such as Lithos, Geochimica and Cosmochimica Acta, Chemical Geology etc. These papers were grouped according to their proposed magma sources as subducting oceanic crust related ones and mafic lower crust related ones. Mafic lower crust related ones are further divided into three groups (MLC I, II and III) according to their Sr-Nd isotopic values *(Figure 21)*. Although all of these were proposed to be sourced from lower crustal material, their Sr-Nd isotope values have major differences. The difference between these groups is the relative amount of upper crustal contamination as more contaminated rocks have more enriched $^{87}Sr/^{86}Sr$ ratios and εNd values. It should be noted that all authors support their chemical interpretations with regional geological evidence but not all the details will be provided in this manuscript. For more details, the reader is referred to original articles.

Subducting oceanic crust related adakite data are coming from Aguillón-Robles et al. (2001) and Gomez-Tuena et al. (2008). Both papers report work from Mexico and the former deals with Late Miocene adakites of Vizcaino Peninsula whereas the latter deals with Miocene high-silica Chalcatzingo trondhjemites. Both papers present MORB-like Sr-Nd data and low K_2O values *(Figure 21-Figure 22)*. Although these rocks still have MgO values less than 3wt%, as original adakite proposition, they are characterized by higher MgO contents with respect to other groups *(Figure 22)*. Gomez-Tuena et al. (2008) also argues low Cr-Ni abundances and high

Mg# also supports slab melting hypothesis *(Figure 20)*. Both papers explain the required shallow slab melting with initiation of ridge subduction.

Mafic lower crust related adakitic rocks of Group I were taken from Quaternary adakites of Anar Region of Iran (Pang et al., 2016) and Miocene adakitic dacites of Eastern Pontides of Turkiye (Eyuboglu et al., 2012) and these rocks show minimal to no upper crustal contamination according to these authors. Both rocks are characterized by low MgO and intermediate K_2O abundances *(Figure 22)*. Moreover, their low Cr-Ni abundances are also in accordance with a crustal source *(Figure 23)*.

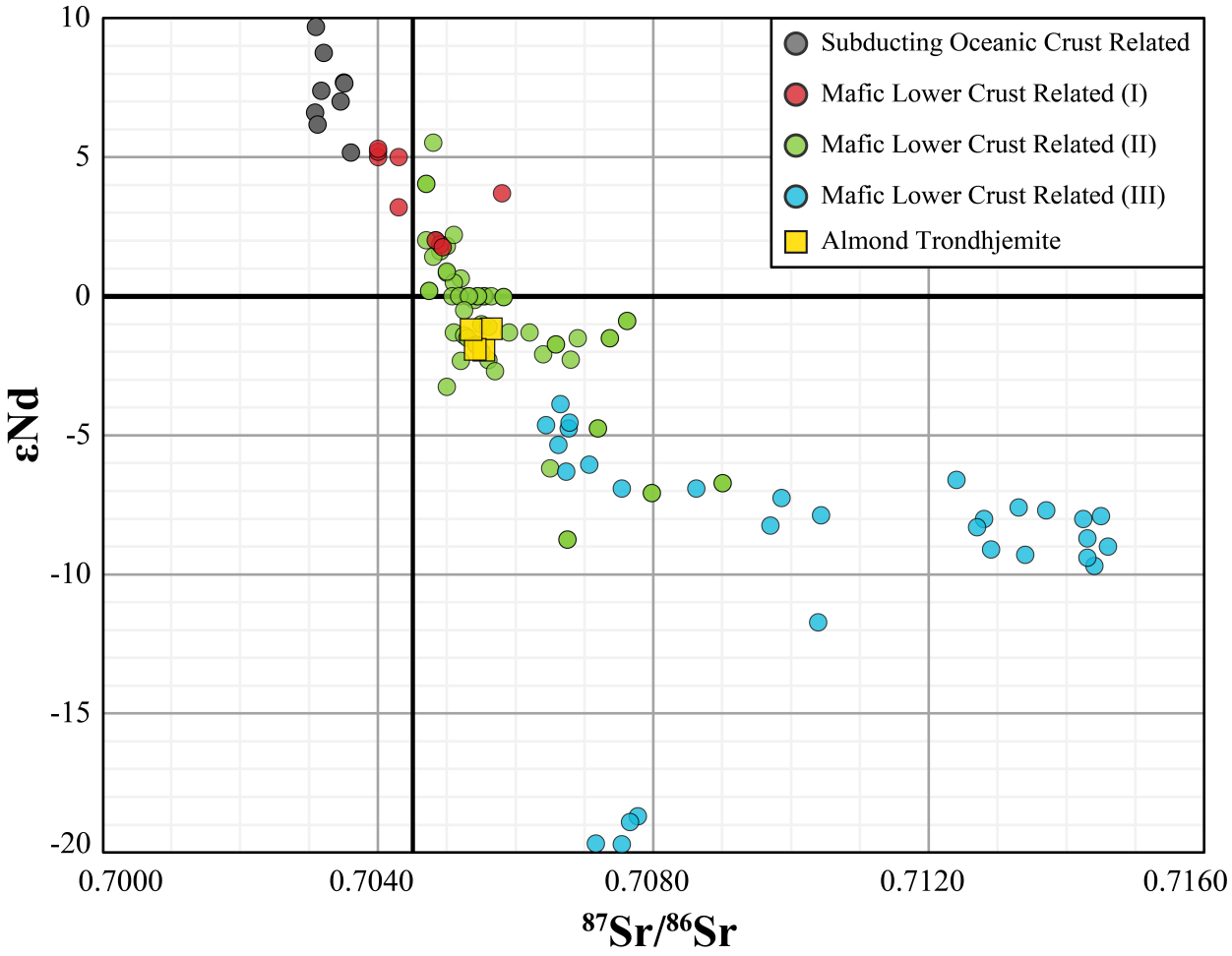

Figure 21: Sr-Nd isotope characteristic of selected adakitic rocks and the AT. See text for references of background data.

Group II data was taken from different parts of Miocene Lhasa Terrane (Tibet) (Hou et al., 2004; Guo et al., 2007) Eocene Eastern Pontides (Turkiye) (Topuz et al., 2005) and Miocene Cordillera Blanca (Peru) (Petford and Atherton, 1996). Rocks of this group show intermediate upper crustal contamination after generation by partial melting of lower crust. The rocks of this group show more variation in all aspects of their geochemistry compared to the previous two groups because of this contamination.

The last group (III) were selected from the most upper-crust contaminated lower-crust sourced adakitic rocks. Data of this group is coming from Miocene Lhasa Terrane (Tibet) (Hao et al., 2021), Devonian Alxa Block (China) (Zhou et al., 2016), and Neoproterozoic Huangling (China) (Zhao et al., 2013). The biggest spread of data is seen in this group since they all are deemed to have been formed by combination of juvenile crust, ultrapotassic-potassic basalts and lower crust. High MgO samples of this group and group II can be explained by some samples interacting with mantle *(Figure 22)*.

Differently sourced adakitic rocks that have different levels of crustal contamination don't seem to have a clear distinction in between. Silica content does not seem to differ because higher silica content can be achieved through assimilation and/or fractionation. From other major oxide wt. percentages, K_2O seems to be the most distinct among different groups. If the K_2O content of adakitic melts are almost entirely controlled by the source rocks (Wang et al., 2022 *and references therein*), the small variation is consistent with proposed MORB and lower crust chemistry. Average MORB K_2O content is 0.16 wt% (Winter, 2013). For lower crust, chemical composition is a bit more debatable since it cannot be sampled directly, but relies on data from exposed terrains, xenoliths and geophysics. *Figure 24* shows different lower crust K_2O abundance estimates from three groups, and it changes between 0.6 to 1.5 wt%. Nonetheless,

lower crust is most likely to have slightly higher K_2O content than MORB and this source effect is somehow seen on K_2O content of different adakite groups.

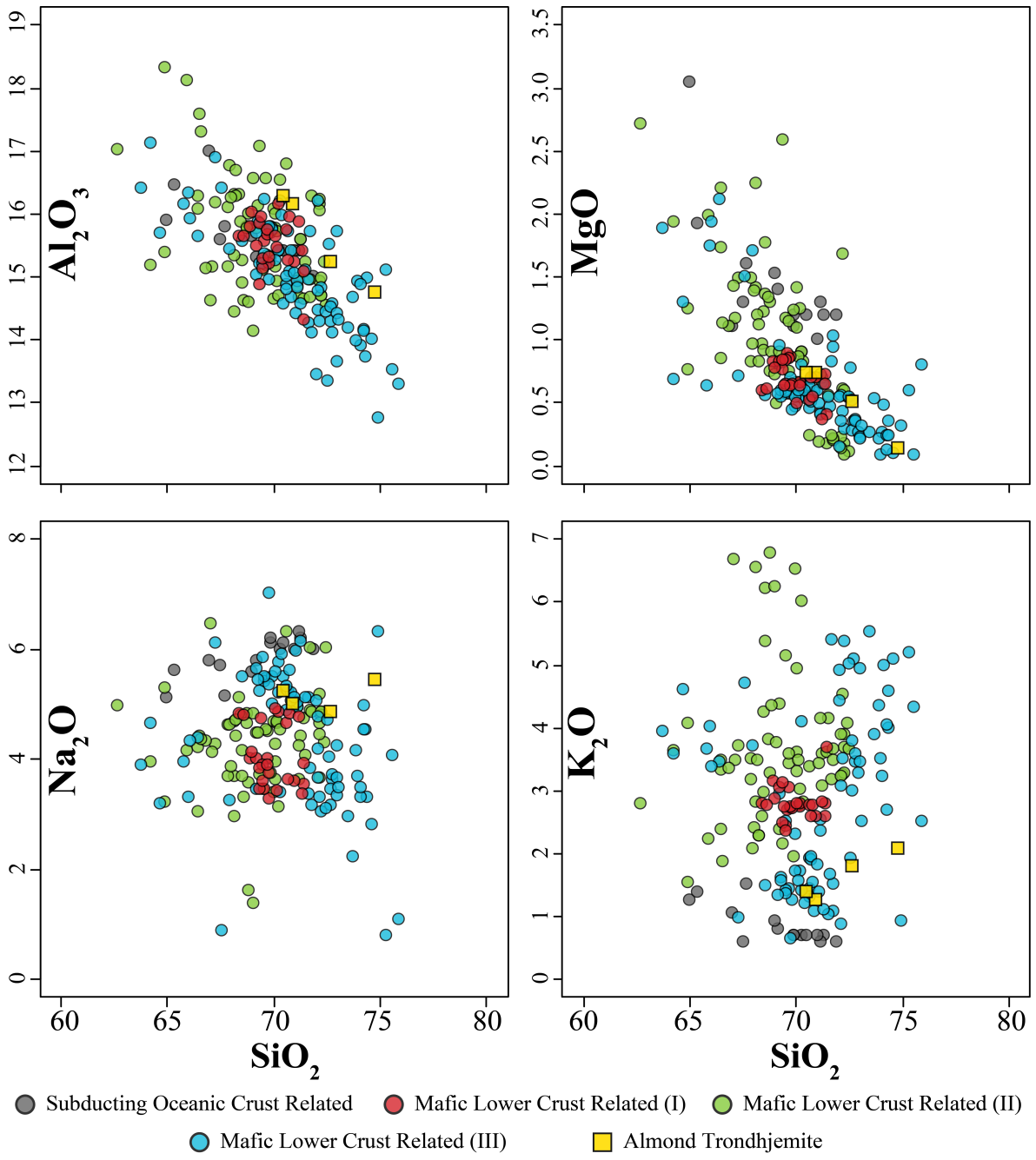

Figure 22: Selected Harker diagrams for the AT and other adakitic groups. All abundances are in wt%.

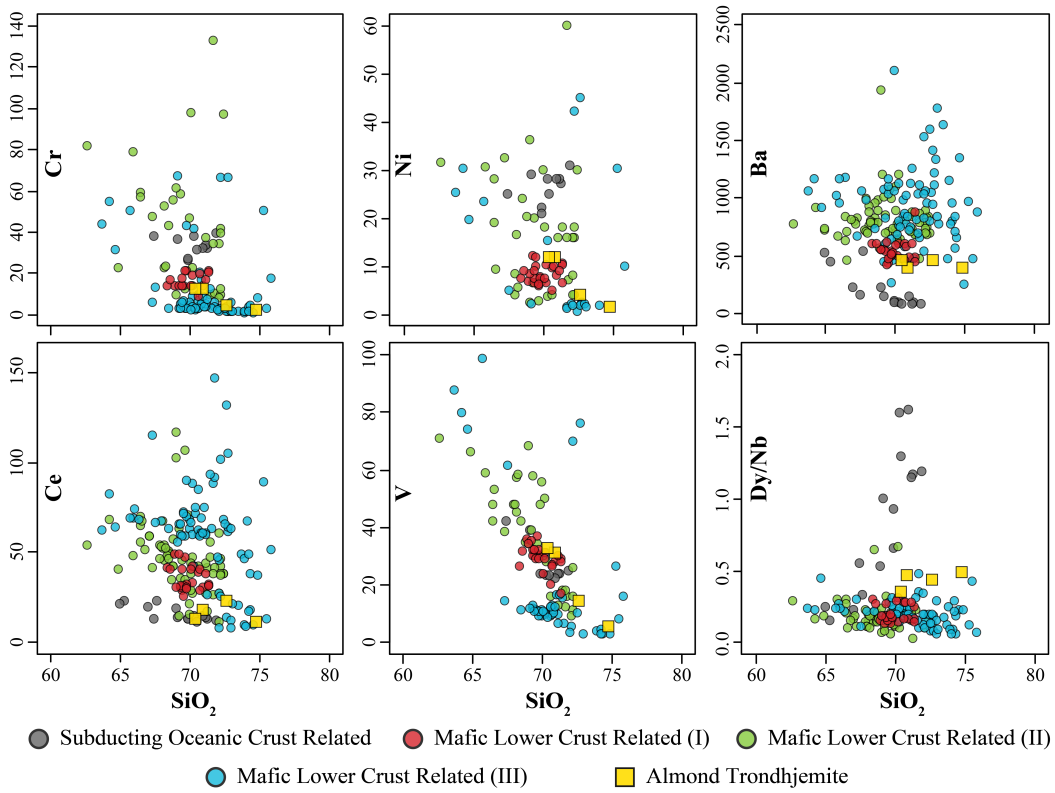

Figure 23: Selected trace element diagrams the AT and other adakitic groups. X axes are wt% and Y axes are ppm.

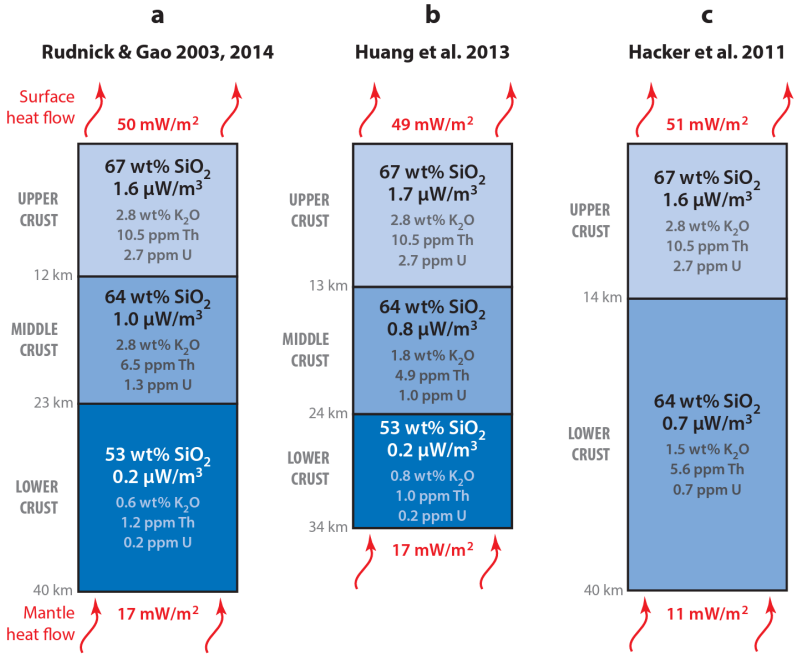

Figure 24: Crustal compositions calculated by three groups. From Hacker et al. (2015).

As mentioned in Castillo (2012), MgO content can be used to discriminate between different adakite sources. the AT is a thick lower crust-derived adakite according to its MgO-SiO_2 content *(Figure 25)*. However, this diagram should be used with caution because of significant overlapping areas between zones.

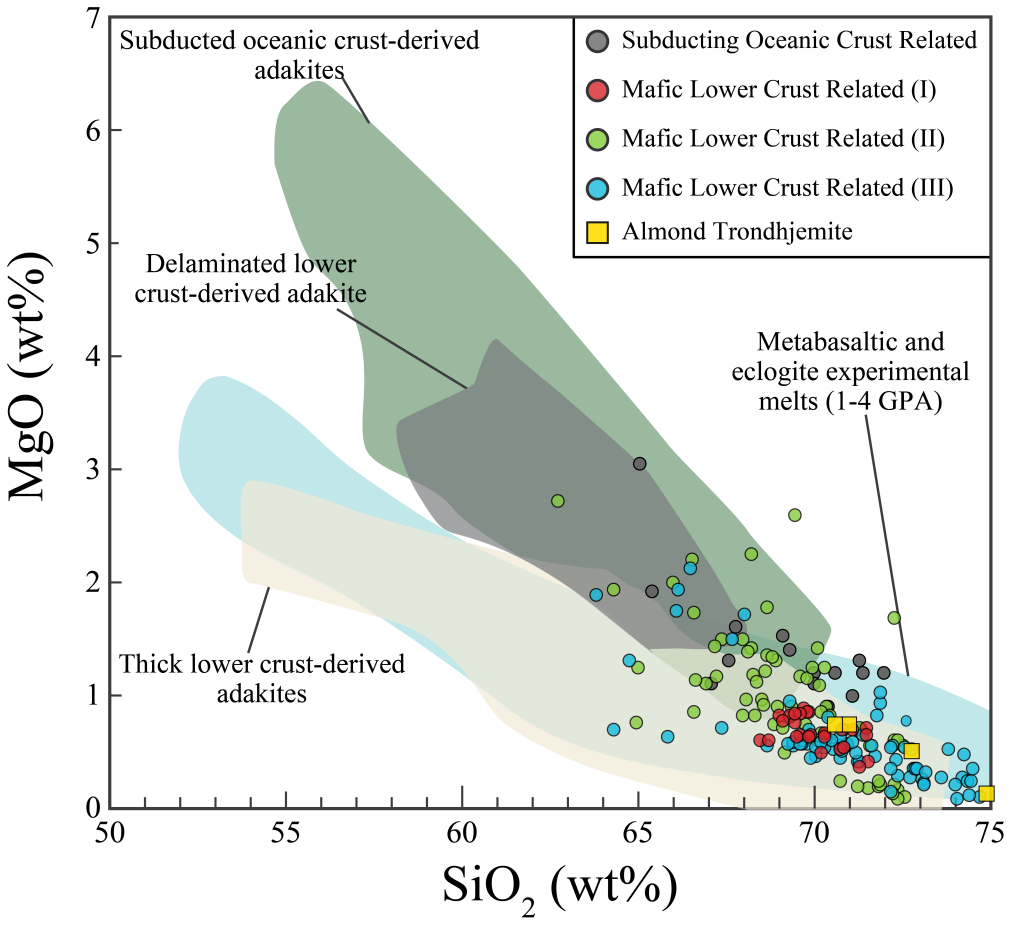

Figure 25: Source discrimination diagram for adakitic rocks. Background data from He et al. (2018) and references therein.

Cr and Ni content seem to be somehow distinct between different sources with the effect of mantle involvement. Mantle can be involved in adakite petrogenesis in two ways: 1) melts generated by anatexis of subducting slab interacts with the mantle wedge and 2) melts generated

by lower crustal anatexis that interacts and equilibrates with mantle via delamination or underplating. The former also get complicated by amount of subduction modification on the mantle wedge and sediment input on melting. Sediment affects silica content of the melt, which effects viscosity of the magma, hence its capacity of interaction with the mantle wedge. In the latter, the amount of interaction can also vary depending on the amount of mantle interaction. Furthermore, these differences may not ensure clear distinction because of their incompatibility with felsic melt. Therefore, Cr and Ni cannot be used as a singular proxy, but as a supporting factor.

When plotted on primitive mantle normalized multi-element and REE diagrams (Sun and McDonough, 1989; McDonough and Sun, 1995; respectively), all groups have similar patterns *(Figure 26)*. They all show strongly positive K, Pb, Sr and Li anomalies, as well as negative Nb, Ta and Ti anomalies. Zr and Hf are also weakly enriched. Some samples of group III (those that are from Zhou et al., 2006) show slightly enriched Ba content. The same samples show positive Eu anomaly in REE diagram which indicates fluid-present melting and no residual plagioclase in the source whereas the AT does not show any prominent anomaly in REE content (Moyen and Stevens, 2006). LREE/HREE ratio is highest in group I samples which show smaller degrees of partial melting and all others are showing higher degrees of partial melting and almost flat HREE patterns.

In selected discrimination diagrams, no prominent difference between groups were observed *(Figure 27)*. All groups fall along metaluminous-peraluminous boundary with no obvious grouping. The small number of S-type group II and III samples can be explained by the crustal components of these melts. H_2O saturated melting of lower crustal was demonstrated to create peraluminous granites (Patino Douce and Beard, 1995; Ratajeski et. al., 2005).

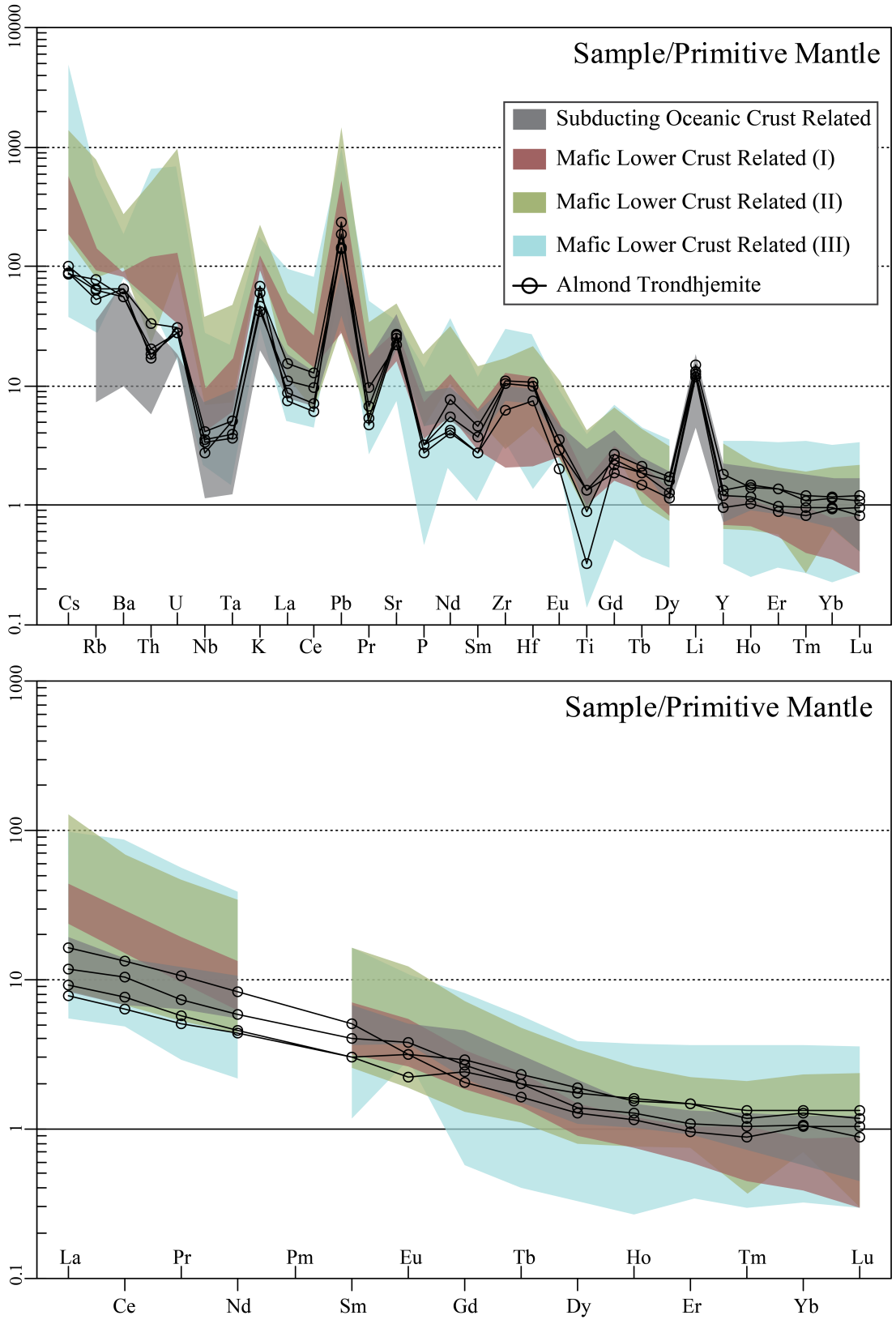

Figure 26: Trace element and REE diagrams for the AT and other adakitic groups.

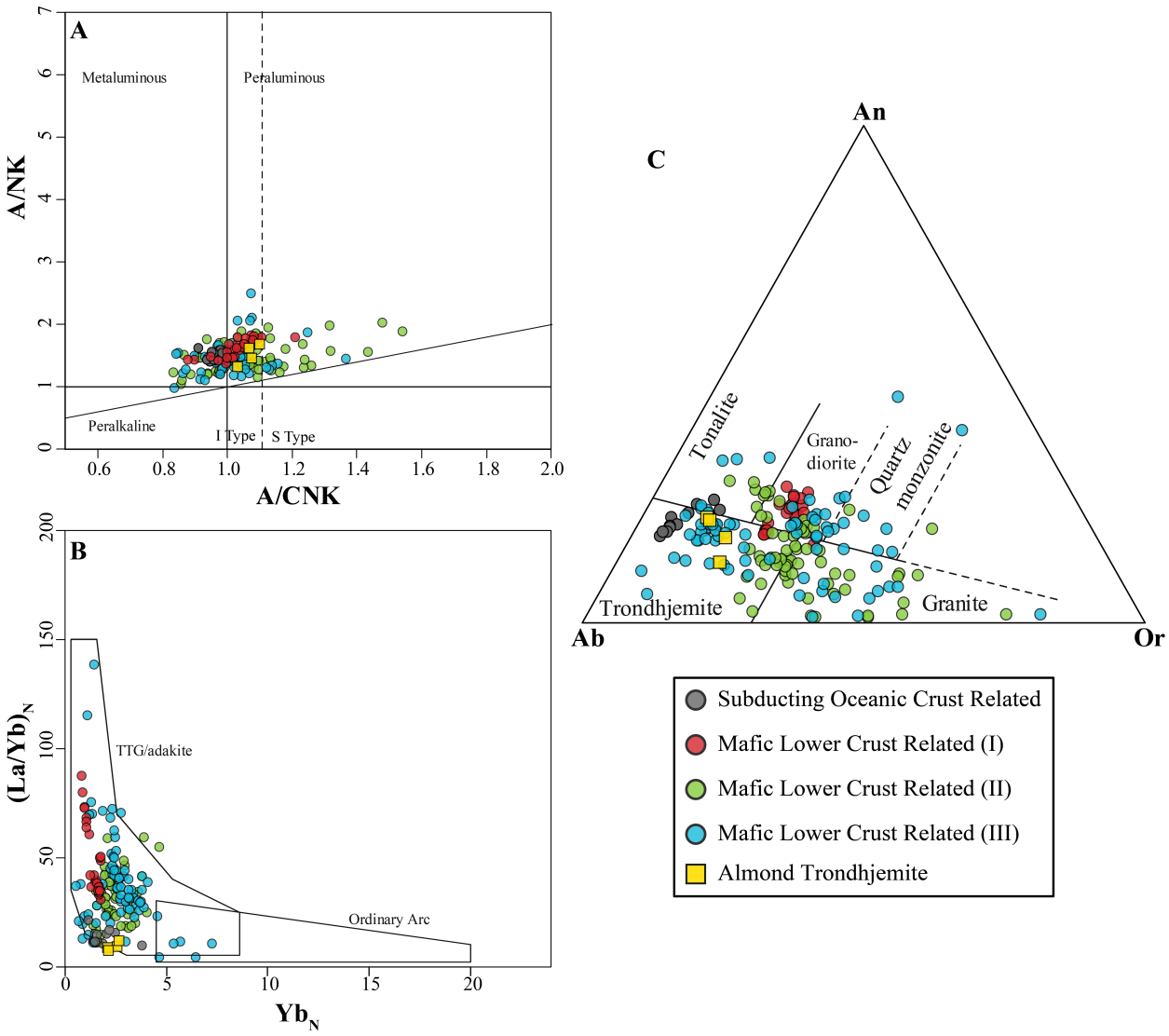

Figure 27: Discrimination diagrams for the AT other adakitic groups. A) Shand, 1943. B) Martin, 1986. C) O'Connor, 1965

From the EPMA data, biotite can be used in a discrimination diagram *(Figure 28).* All biotites are Fe-rich character (i.e., ferribiotite) and they all plot on intensely contaminated reduced I-type (I-SCR) biotite zone with a small number of data plot exclusively in S-type zone. The presence of topaz as an accessory phase is also supporting whole rock analysis of peraluminous character of this pluton and indicate extreme fractionation (Konyshev et al., 2020). However, abundance of it needs to be considered while discussing its implications, which is only

in trace amounts. Moreover, extremely fractionated topaz bearing granites are also expected to be rich in Li bearing white micas such as zinnwaldite and/or lepidolite (Manning and Hill, 1990; Frindt et al., 2004; Barker and Reed 2010). It has been argued that topaz bearing granites may be generated by partial melting of lower crustal material and through fractionation, However, no Li bearing white mica was observed by EPMA, all measured white micas are muscovite. In this regard, the AT is not similar to these topaz granites. Nonetheless, the AT could have been produced this way but have not fractionated as much as these topaz bearing granites.

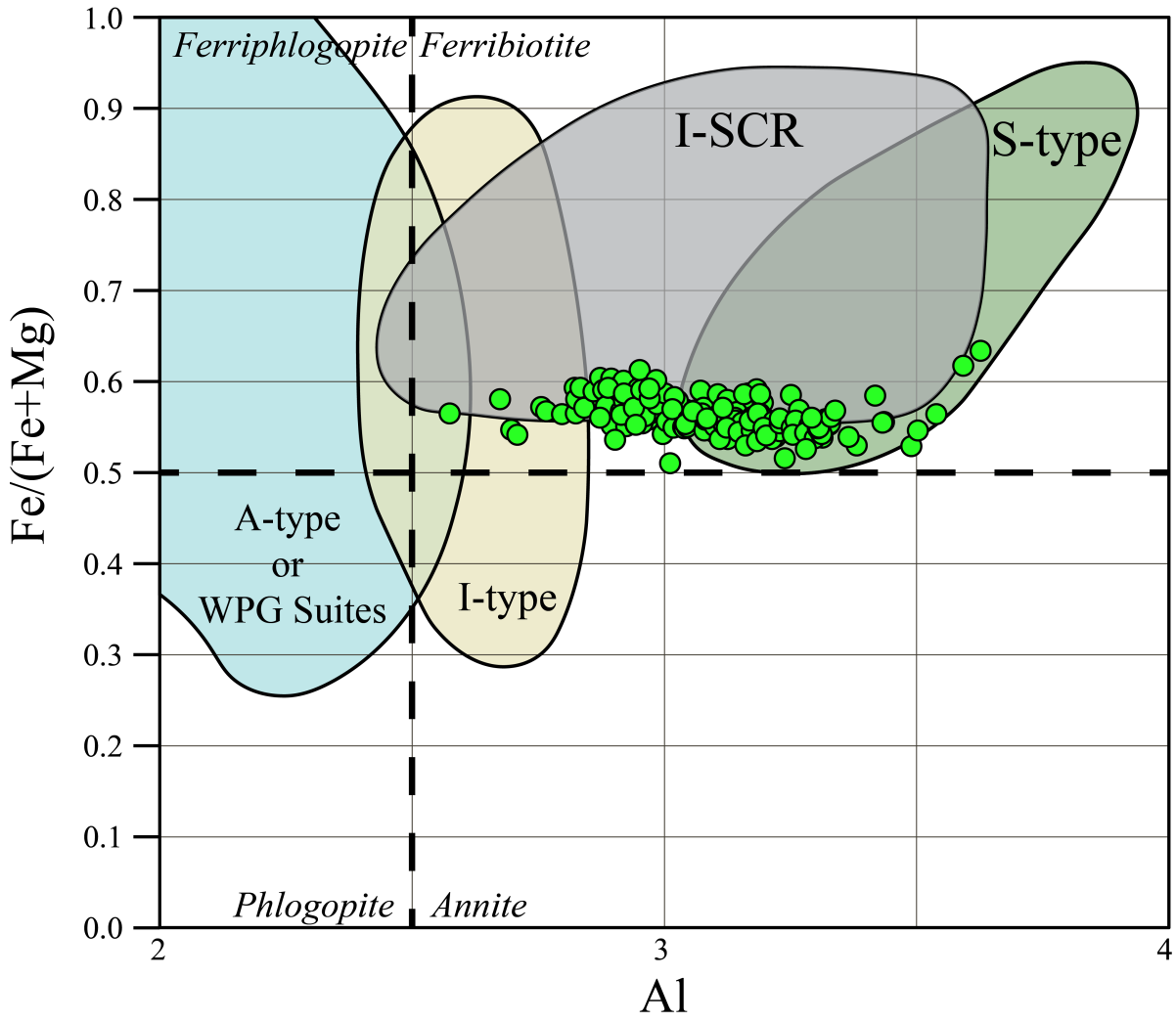

Figure 28: Biotite classification and source diagram (Shabani et al., 2003).

Apart from the small overlap between different sources, the best way to discriminate different adakitic/trondhjemitic sources seem to be through K_2O and Rb contents, as originally proposed by Drummond et al. (1996) *(Figure 29)*. Although none of these lines of evidence is enough for a comprehensive interpretation alone, when all of them are combined, lower crustal origin for the AT with garnet-amphibolite residue is the most likely scenario. Upper crustal contamination on this magma is present but not extensive as evidenced by Sr-Nd isotope systematics.

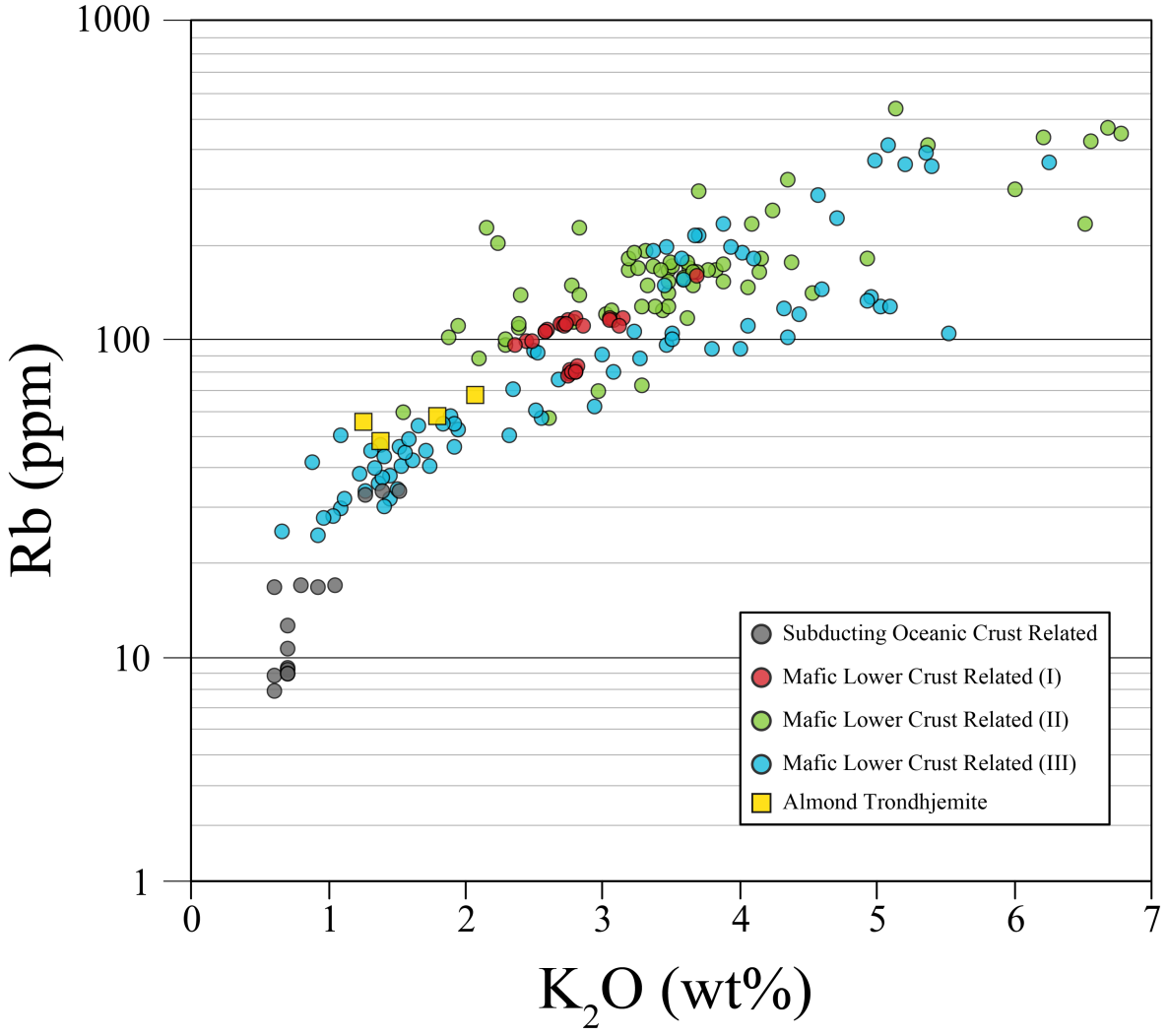

Figure 29: K_2O vs Rb graph for different groups of adakitic/trondhjemitic rocks.

4.2 Implications for Southernmost Appalachian Tectonics

The great difference between Nd modal ages and zircon ages proves that the crustal residence age of the AT is much older than crystallization age. Although it crystallized during the Alleghenian orogeny, its source is not juvenile Appalachian crust, but reworked Grenville crust. Such affiliation is observed in Mexico (Oaxaca Terrane: Yáñez et al., 1991), through Texas (Llano uplift: Mosher, 1998), Alabama (Pine Mountain Window: Steltenpohl et al., 2004), Carolinas (Tallulah Falls Dome, Toxaway Dome and Trimont Ridge: Hatcher et al. 2004), Virginia (Goochland Terrane: Owens and Samson, 2004) and all the way up to New York (Adirondack Massif: McLelland et al., 1993). *Figure 30* shows a compilation of Grenvillian T_{DM} data from these locations.

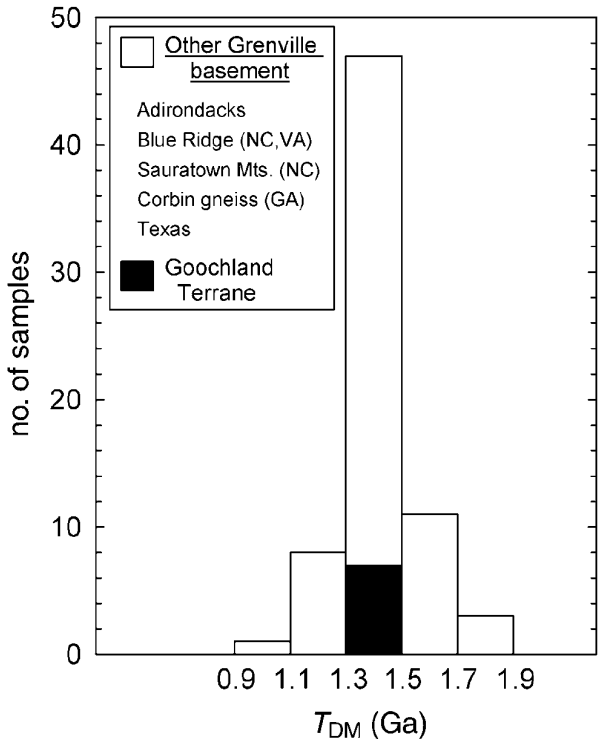

Figure 30: Compiled T_{DM} for Grenvillian basement rocks. The data is compiled by Owens and Samson (2004) and their compilation includes data from Pettingill et al. (1984), Patchett and Ruiz (1989), Daly and McLelland (1991), McLelland et al. (1993), Heatherington et al. (1996), Fullagar et al. (1997).

Adakite/trondhjemite generation is generally accompanied by potassic-ultrapotassic magmas nearby (e.g., Hou et al., 2004; Guo et al., 2007; Pang et al., 2016; Hao et al., 2021). These potassic magmas are mantle sourced basalts. They are thought to be products of the underplating and the source of heat for the adakite/trondhjemite generation. However, no broadly coeval mantle related basic rock have been reported in southernmost Appalachians. If the intrusion depth for the AT is 14km, as calculated with EPMA here, these mantle related rocks may have been eroded away or not present at all. Therefore, it is not possible to discuss the lower crustal origin in relation to nearby rocks which undermines the asthenospheric upwelling scenario. According to these, generation of the AT may be the result of crustal thickening and anatexis without an external heat source such as underplating. Proposed minimum thickness for southern Appalachians during Neoacadian (27-39 km, Stowell et al., 2019) are sufficient for adakite generation based on the study of Qian and Hermann (2013).

During the beginning of collision, partial melting of middle-lower crustal metasediments can generate low Sr/Y plutons without any mantle involvement. The availability of water is the key factor that controls the generation of these magmas. The required water may be supplied externally by subducting (most likely still intact) slab, or internally through dehydration of metasediments in crust (England and Thompson, 1986). At this time, the crust is not thick enough to extend beyond garnet-in depth and generated magmas will not show adakitic character. With more thickening later, the crust reaches to a sufficient thickness for lower portions to reach garnet stability depths that allows generation of high Sr/Y magmas. This type of paired high-low Sr/Y plutons were also documented in Baja-California and New Zealand by Tulloch and Kimbrough (2003 and references therein). They show that 30-40 Myr of low Sr/Y was followed by 15-20 Myr of quiescence in igneous activity (i.e., magmatic lull) and later

development of high Sr/Y magmas in 15-20 Myr. Igneous quiescence, coeval thrusting and crustal thickening was argued to be controlled by flattening of subducting slab. Both Baja-California and New Zealand show clear boundaries between continental inward high Sr/Y and outward low Sr/Y suits due to slab flattening between emplacement of these suits. This model is consistent with the southernmost Appalachians when the ages of low and high Sr/Y plutons are considered (390-365Ma and 349-335Ma, respectively) (Stowell et al., 2019). The transition between these was marked by a ~16Myr igneous quiescence, assuming rocks that were eroded away or that are still not exposed don't include an intrusive body of either type. This duration seems enough for crustal thickening required to produce adakitic magmas. Reported thrust stacking during 360-345 Ma (Gastaldo et al., 1993; Merschat et al., 2005) in the southern Appalachians shows this thickening was not only through thermal processes, but also mechanically supported. The involvement of slab geometry change (i.e., flattening, rollback) is not clear in the study region because high-low Sr/Y rocks do not show a clear orogen-parallel boundary as in paired plutonic belts model of Tulloch and Kimbrough (2003) *(Figure 3)*. The model also requires a slab geometry modification since it does not end with continental collision. However, Alleghenian orogeny ended in continental collision and formation of Pangea (Hatcher, 2010), which necessitates a slab breakoff.

The slab breakoff (or slab-failure magmatism) results in a distinct chemical characteristics (no Eu anomalies, low Y, depleted heavy REE, Nb/Y>0.4, La/Yb>10, Gd/Yb>2.0, Sm/Yb>2.5 and Sr/Y>10) as outlined in Hildebrand et al. (2018), Hildebrand and Whalen (2021) and Kusky and Wang (2022) *and references therein*. In this model, high Sr/Y magmas may result from either partial melting of the garnetiferous plagioclase-free metabasalts from detached slab or melting of partly subducted continental crust on the down-going passive

margin. During the former, they may still yield old crustal Sr-Nd isotopic signatures through assimilation (Hildebrand and Whalen, 2021). The AT has similar characteristics to these slab failure rocks. However, I think the option of partial melting of detached slab assimilating old Grenvillian crust and completely mimicking its isotopic signature (e.g.; Hildebrand and Whalen, 2021) is unlikely. In this case, seeing mixed T_{DM} ages would be more plausible whereas AT is showing strong Grenvillian crustal character based on crustal residence age (T_{DM}). However, melting of partially subducted lower crust ~17Myr after the collision was shown in numerical model of Freeburn et al. (2017)(Figure 31), and it explains Grenvillian crustal signatures, ~15Myr igneous quiescence between high-low Sr/Y magmas and established source characteristics. With that said, the scope of this project does not include a wide selection of data from different plutonic bodies of southernmost Appalachians and the problems of existing data was previously discussed. Thus, more data on Neoacadian-Alleghenian granitoids are needed to construct better subduction-collision models in Southern Appalachians.

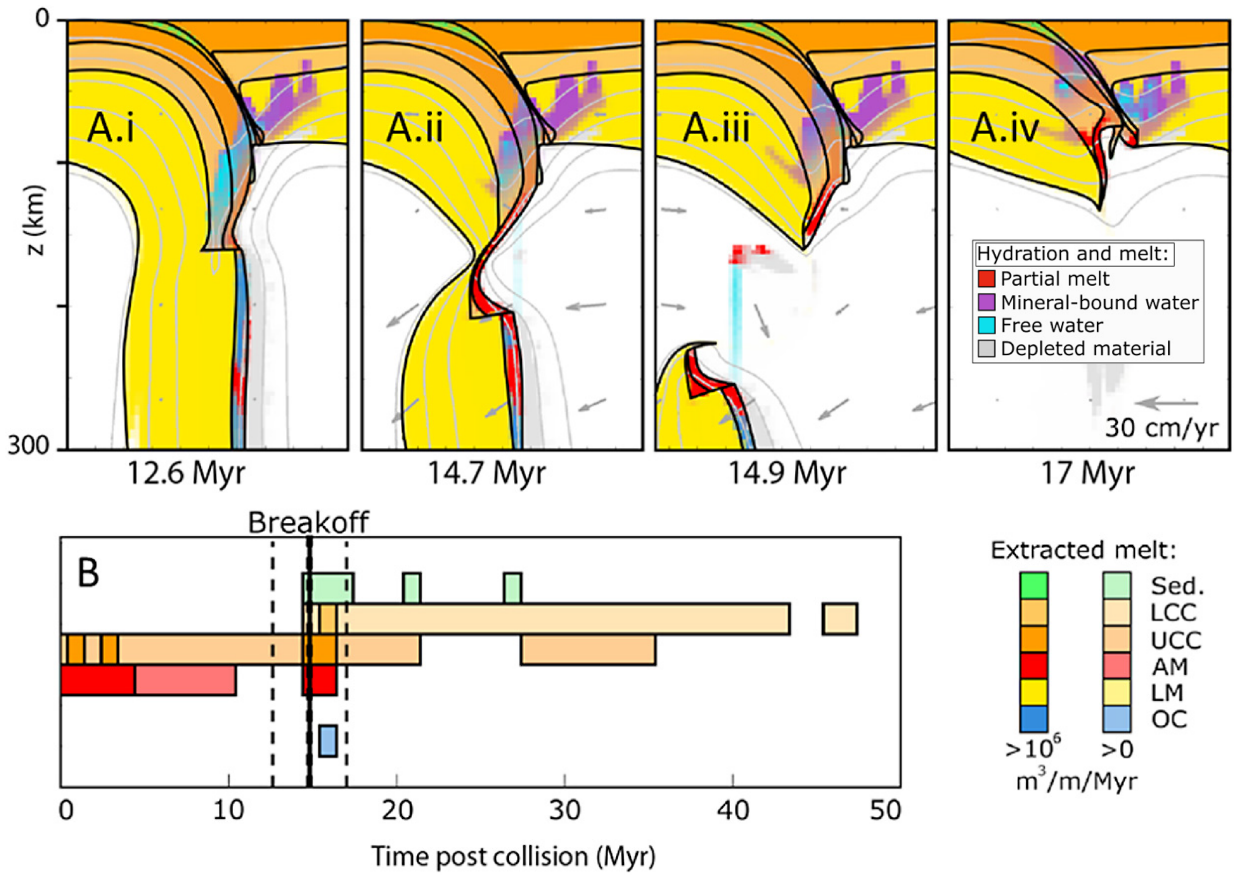

*Figure 31: Numerical model of slab detachment magmatism by Freeburn et al. (2017). *Sed: Sediments, LLC: Lower Continental Crust, UCC: Upper Continental Crust, AM: Asthenospheric Mantle, LM: Lithospheric Mantle, OC: Oceanic Crust.*

Another issue with high Sr/Y granites in Alabama is their genetic relations with each other (Drummond et al., 1984, 1997; Stowell et al., 2019). The problems of compiled dataset from high Sr/Y magmas of southernmost Appalachians were discussed earlier, however, they may still suggest a potential correlation. *Figure 32* shows Harker diagrams for high Sr/Y magmas of southernmost Appalachians. Although some correlations seem to be weak (especially

Na_2O seems problematic), this data shows a genetic relationship between these rocks. The presence, but weakness of correlation can be attributed to the questionable nature of earlier data.

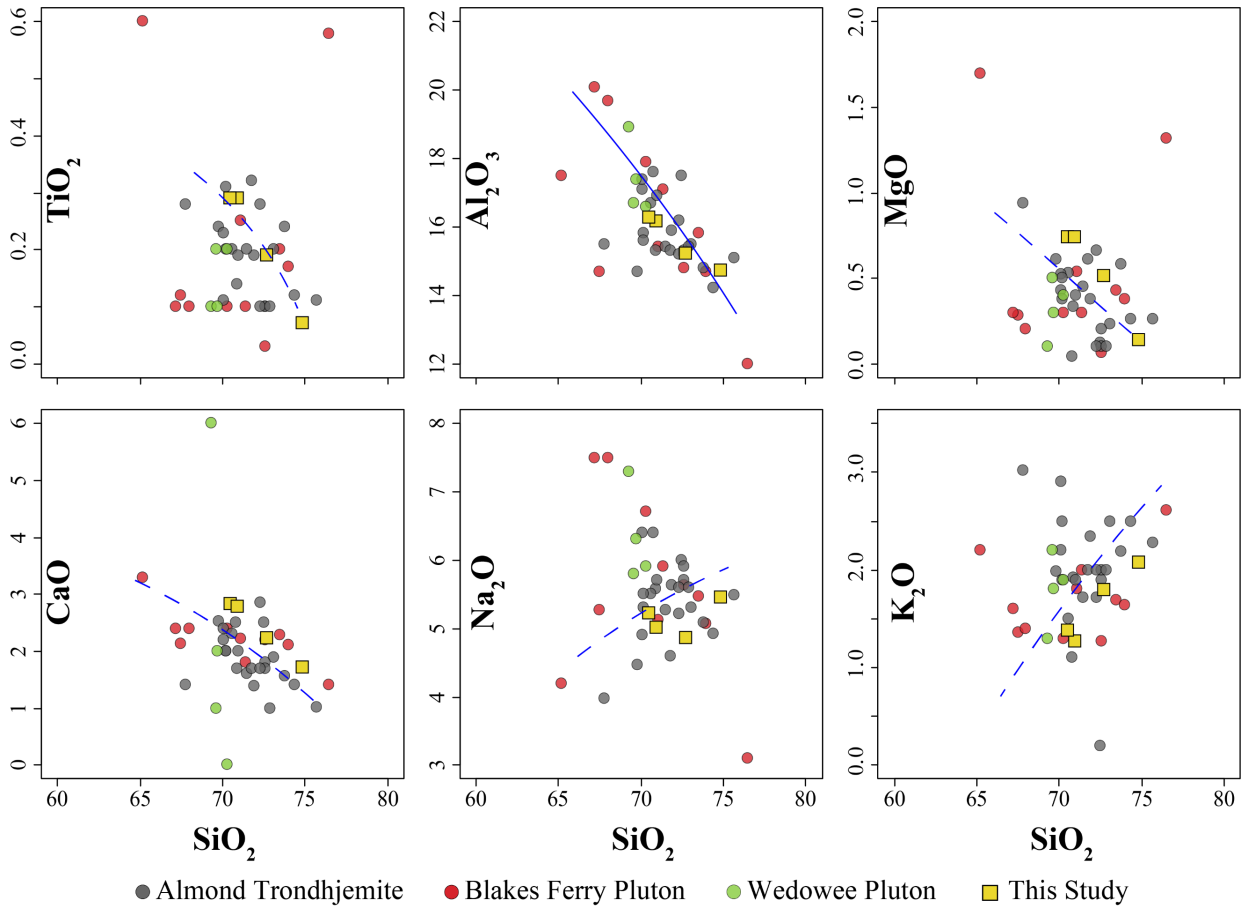

Figure 32: Harker diagrams for high Sr/Y plutons of southernmost Appalachians. Data from Deininger et al. (1973), Size and Dean (1987) and Ingram (2012). Solid and dashed blue lines show stronger and weaker trends, respectively. All abundances are in wt%.

4.3 Post Crystallization

The ~20 Myr difference in U-Pb zircon age and $^{40}Ar/^{39}Ar$ muscovite age shows that muscovite cooling should be related to translation towards shallower depths after magma crystallization.

The age of cooling event possibly corresponds to the activity of the Alexander City Fault (ACF) that was associated with greenschist facies ductile shearing. It was proposed as a south-dipping dextral-normal shear zone that formed along brittle-ductile transition zone, but it also shows minor reverse slip features. It results in mylonite zones that show drastic thickness changes along-strike. In southern portions, AMD-1, 3 sample locations, close to where the mylonite zone is the thickest (Steltenpohl et al., 2013) *(Figure 3)*. Two garnetiferous phyllonite samples from this thicker zone yield muscovite $^{40}Ar/^{39}Ar$ ages of 317.22 ± 0.61 and 317.31 ± 0.45 Ma and these were interpreted as last mid-crustal level deformation in the basis of recrystallization and internal deformation of muscovites (Poole, 2015). Although deformation is present, AT does not show complete recrystallization of micas, therefore presented ages here does not represent the deformation age. $^{40}Ar/^{39}Ar$ ages presented here represents the regional cooling, which was suggested to get progressively older from SE to NW in the area (Poole, 2015: Ma et al., 2019. This was explained with rolling-hinge type core complex exhumation by Ma et al. (2019) using a compilation of $^{40}Ar/^{39}Ar$ ages, as well as new their novel data from Georgia and Alabama. According to this configuration, AT is located on the footwall of this exhumation and the muscovite $^{40}Ar/^{39}Ar$ ages reported here are consistent with what was predicted by muscovite cooling age contours (Figure 2b of Ma et al., 2019).

5. Conclusions

Almond Trondhjemite of southernmost Appalachians lacked solid data to answer fundamental questions: 1) what is the source of its parent magma? 2)what was its emplacement conditions in terms of pressure and temperature? 3)what is its post-crystallization story? The first question was answered through Sr-Nd isotopic analyses, whole rock and mineral chemistry. The second question was answered with mineral chemistry and the last one was answered with $^{40}Ar/^{39}Ar$ thermochronology. Answering all these questions also shed light on the place of Almond Trondhjemite in Paleozoic and Mesozoic Appalachian tectonics and the following conclusions were drawn from the results.

- Almond Trondhjemite is a weakly foliated, high Sr/Y rock with adakitic character and its mineral assemblage is quartz+plagioclase (mostly oligoclase)+muscovite+biotite with trace amounts of zircon+apatite and secondary epidote+calcite.
- The magma source for Almond Trondhjemite is anatexis of orogenically thickened lower crustal mafic material as evidenced by Sr-Nd isotope systematics and geochemistry. Crustal material in the source is reworked Grenvillian crust, rather than juvenile Appalachian crust and the mid-upper crustal contamination is limited. Whether this anatexis was aided by mantle upwelling is unclear because the associated mantle related rocks are either absent or eroded away.
- Biotites of Almond Trondhjemite crystallized at mean temperature of 630 °C that shows the magma had experienced H_2O flux during crystallization. Biotite geobarometer yield mean crystallization depth of 14.1 km. No amphibole was found for further geobarometric calculations.

- Muscovite $^{40}Ar/^{39}Ar$ ages of Almond Trondhjemite are consistent with the regional core complex-style cooling event that was suggested to get younger from NW to SE.
- Although southernmost Appalachian granites were subject to number of studies and review papers, accumulated data on these rocks have problems. Accumulation of new and high-quality data will allow further discussions on problems that were discussed here.
- Petrogenesis of adakite/trondhjemite rocks is not rigorously constrained in the literature and more robust proxies should be developed to better constrain the source of these magmas. Their relation to slab-failure magmatism and whether they represent the same geodynamic events with 'classical' adakite/trondhjemite magmas should be further discovered.

6. References

Aguillón-Robles, A., Calmus, T., Benoit, M., Bellon, H., Maury, R. C., Cotten, J., ... & Michaud, F. (2001). Late Miocene adakites and Nb-enriched basalts from Vizcaino Peninsula, Mexico: indicators of East Pacific rise subduction below southern Baja California?. Geology, 29(6), 531-534.

Annen, C.,Blundy, J.D., Sparks,R.S.J., 2006. The genesis of intermediate and silicic magmas in deep crustal hot zones. J. Petrol. 47, 505–539.

Armstrong RL (1966) K–Ar dating of plutonic and volcanic rocks in orogenic belts. In: Schaeffer OA and Za¨hringer J (eds.) Potassium–Argon Dating, pp. 117–133. Berlin: Springer-Verlag.

Barker, C.A., Secor, D.T., Pray, J.R., and Wright, J.E., 1998, Age and deformation of the Longtown metagranite, South Carolina Piedmont—A possible constraint on the origin of the Carolina terrane: The Journal of Geology, v. 106, p. 713–725, doi: 10.1086/516055.

Barker, D. S., & Reed, R. M. (2010). Proterozoic granites of the Llano Uplift, Texas: A collision–related suite containing rapakivi and topaz granites. GSA Bulletin, 122(1-2), 253-264.

Barker, F., 1979, Trondhjemite: definition, environment and hypotheses of origin, in Barker, F., ed., Trondhjemites, dacites, and related rocks: New York, Elsevier, p. 1–12.

Bea, F., Montero, P., Barcos, L., Cambeses, A., Molina, J. F., & Morales, I. (2023). Understanding Nd model ages of granite rocks: The effects of the $^{147}Sm/^{144}Nd$ variability during partial melting and crystallization. Lithos, 436, 106940.

Blackburn, T. J., Olsen, P. E., Bowring, S. A., McLean, N. M., Kent, D. V., Puffer, J., ... & Et-

Touhami, M. (2013). Zircon U-Pb geochronology links the end-Triassic extinction with the Central Atlantic Magmatic Province. Science, 340(6135), 941-945.

Bouvier, A., Vervoort, J. D., & Patchett, P. J. (2008). The Lu–Hf and Sm–Nd isotopic composition of CHUR: constraints from unequilibrated chondrites and implications for the bulk composition of terrestrial planets. Earth and Planetary Science Letters, 273(1-2), 48-57.

Bream, B. R., Hatcher, R. D., Miller, C. F., Fullagar, P. D., Tollo, R. P., McLelland, J., ... & Bartholomew, M. J. (2004). Detrital zircon ages and Nd isotopic data from the southern Appalachian crystalline core, Georgia, South Carolina, North Carolina, and Tennessee: New provenance constraints for part of the Laurentian margin. Memoirs-Geological Society of America, 459-476.

Briggs, P. H., & Meier, A. L. (1999). The determination of forty two elements in geological materials by inductively coupled plasma-mass spectrometry (p. 15). Denver, CO, USA: US Department of the Interior, US Geological Survey.

Castillo, P. R. (2012). Adakite petrogenesis. Lithos, 134, 304-316.

Castillo, P. R., Janney, P. E., & Solidum, R. U. (1999). Petrology and geochemistry of Camiguin Island, southern Philippines: insights to the source of adakites and other lavas in a complex arc setting. Contributions to mineralogy and petrology, 134(1), 33-51.

Cawood, P., Kroner, A., Collins, W., *Kusky, T.M.*, Mooney, W.D., and Windley, B.F., 2009, Earth Accretionary Orogens in Space and Time, Geological Society of London Special Publication, 318, 1–36. DOI: 10.1144/SP318.1

Challener, S. C., and Glazner, A. F. (2017). Igneous or metamorphic? Hornblende phenocrysts as

greenschist facies reaction cells in the half dome granodiorite, California. Am. Mineral. 102, 436–444. doi: 10.2138/am-2017-5864.

Christiansen, E. H., Haapala, I., & Hart, G. L. (2007). Are Cenozoic topaz rhyolites the erupted equivalents of Proterozoic rapakivi granites? Examples from the western United States and Finland. Lithos, 97(1-2), 219-246.

Clauer, N., 2013, The K-Ar and $^{40}Ar/^{39}Ar$ methods revisited for dating fine-grained K-bearing clay minerals: Chemical Geology, v. 354, p. 163–185, https://doi.org/10.1016/j.chemgeo.2013.05.030.

Dalrymple, G. B., & Lanphere, M. A. (1971). 40Ar/39Ar technique of KAr dating: a comparison with the conventional technique. Earth and Planetary Science Letters, 12(3), 300-308.

Daly, J.S., and McLelland, J.M., 1991, Juvenile Middle Proterozoic crust in the Adirondack Highlands, Grenville province, northeastern North America: Geology, v. 19, p. 119–122.

Deer, R. A., Howie, R.A., Zussman, J. (2013). Introduction to the Rock-ForminMinerals (Third ed.). Mineralogical Society of Great Britain and Ireland.

Defant, M. J., Drummond, M. S., Arthur, J. D., Ragland, P. C., & Green, N. L. (1987). The petrogenesis of the Blakes Ferry pluton, Randolph County, Alabama. Granites of Alabama: Alabama Geological Survey Bulletin, 128, 97-116.

Defant, M. J., & Drummond, M. S. (1990). Derivation of some modern arc magmas by melting of young subducted lithosphere. *Nature*, *347*(6294), 662-665.

Deininger, R. W., Neathery, T. L., & Bentley, R. D. (1973). Genetic relationships among granitic rocks in the northern Alabama Piedmont. Alabama Geological Survey Open-File Report, 18.

DePaolo, D. J. (1981). Trace element and isotopic effects of combined wallrock assimilation and fractional crystallization. Earth and planetary science letters, 53(2), 189-202.

DePaolo, D. J., Linn, A. M., & Schubert, G. (1991). The continental crustal age distribution: Methods of determining mantle separation ages from Sm-Nd isotopic data and application to the southwestern United States. Journal of Geophysical Research: Solid Earth, 96(B2), 2071-2088.

Dodson, M. H. (1973). Closure temperature in cooling geochronological and petrological systems. Contributions to Mineralogy and Petrology, 40(3), 259-274.

Dostal, J., & Chatterjee, A. K. (1995). Origin of topaz-bearing and related peraluminous granites of the Late Devonian Davis Lake pluton, Nova Scotia, Canada: crystal versus fluid fractionation. Chemical Geology, 123(1-4), 67-88.

Drummond, M. S., Green, N. L., & Neilson, M. J. (1987). THE GRANITES OF ALABAMA, Road Logs.(1987).

Drummond, M.S., Neilson, M.J., Allison, D.T., and Tull, J.F., 1997, Igneous petrogenesis and tectonic setting of granitic rocks from the eastern Blue Ridge and Inner Piedmont, Alabama Appalachians, in Sinha, A.K., Whalen, J.B., and Hogan, J.P., eds., The Nature of Magmatism in the Appalachian Orogen: Geological Society of America Memoir 191, p. 147–164.

England, P. C., & Thompson, A. (1986). Some thermal and tectonic models for crustal melting in continental collision zones. Geological Society, London, Special Publications, 19(1), 83-94.

Erdmann, S., Wang, R., Huang, F., Scaillet, B., Zhao, K., Liu, H., ... & Faure, M. (2019).

Titanite: A potential solidus barometer for granitic magma systems. Comptes Rendus Geoscience, 351(8), 551-561.

Eyuboglu, Y., Dudás, F. Ö., Zhu, D. C., Santosh, M., Liu, Z., Chatterjee, N., & Yi, K. (2021). Late Cretaceous alkaline magmas of the Eastern Pontides Orogenic Belt (NE Turkey): A review with new geological, geochemical and geochronological data. Gondwana Research, 97, 204-239.

Floyd, P. A., & Winchester, J. A. (1978). Identification and discrimination of altered and metamorphosed volcanic rocks using immobile elements. Chemical Geology, 21(3-4), 291-306.

Freeburn R, Bouilhol P, Maunder B, Magni V, van Hunen J. 2017. Numerical models of the magmatic processes induced by slab breakoff. Earth Planet Sci Lett, 478: 203–213.

Frindt, S., Trumbull, R. B., & Romer, R. L. (2004). Petrogenesis of the Gross Spitzkoppe topaz granite, central western Namibia: a geochemical and Nd–Sr–Pb isotope study. Chemical Geology, 206(1-2), 43-71.

Fullagar, P.D., Goldberg, S.A., and Butler, J.R., 1997, Nd and Sr isotopic characterization of crystalline rocks from the Southern Appalachian Piedmont and Blue Ridge, North and South Carolina, in Sinha, A.K., et al., eds., The nature of magmatism in the Appalachian orogen: Boulder, Colorado, Geological Society of America Memoir 191, p. 165–179.

Gastaldo, R.A., Guthrie, G.M., and Steltenpohl, M.G., 1993, Mississippian fossils from Southern Appalachian metamorphic rocks and their implications for late Paleozoic tectonic evolution: Science, v. 262, p. 732–734, https:// doi .org /10 .1126 /science .262 .5134 .732 .

Gill, K.K., King, D.T.J., Zou, H.B., Smith, F., 2018. Sedimentary Facies Analysis and Strontium-Isotope Stratigraphy of the Hillbank and Yalbac Formations, Corozal Basin, Belize. Gulf Coast Association of Geological Societies Transactions, 68: 229-254.

Grove, M., and Harrison, T.M., 1996, ^{40}Ar* diffusion in Fe rich biotite: American Mineralogist, v. 81, p. 940–951.

Guo, Z.F., Wilson, M., Liu, J.Q., 2007. Post-collisional adakites in south Tibet: products of partial melting of subduction-modified lower crust. Lithos 96, 205–224.

Guo, Z.P., Zou, H.B., 2021. Decoupled whole-rock and zircon Hf isotopes in young evolved post-collisional lavas from Dayingshan (SE Tibet): Evidence for open-system magmatic processes. Lithos, 400-401: 106393.

Hacker, B. R., Kelemen, P. B., & Behn, M. D. (2015). Continental lower crust. Annual Review of Earth and Planetary Sciences, 43, 167-205.

Hames, W. E., Renne, P. R., & Ruppel, C. (2000). New evidence for geologically instantaneous emplacement of earliest Jurassic Central Atlantic magmatic province basalts on the North American margin. Geology, 28(9), 859-862.

Hames, W. E. (2020). K/Ar and 40Ar/39Ar dating methods. Reference Module in Earth Systems and Environmental Sciences.

Hao, L. L., Wang, Q., Kerr, A. C., Yang, J. H., Ma, L., Qi, Y., ... & Ou, Q. (2021). Post-collisional crustal thickening and plateau uplift of southern Tibet: Insights from Cenozoic magmatism in the Wuyu area of the eastern Lhasa block. GSA Bulletin, 133(7-8), 1634-1648.

Harrison, T.M., Celerier, J., Aikman, A.B., Hermann, J., and Heizler, M.T., 2009, Diffusion of

40Ar in muscovite: Geochimica et Cosmochimica Acta, v. 73, no. 4, p. 1039–1051, https://doi.org/10.1016/j.gca.2008.09.038.

Hatcher, R.D., Jr., 2010, The Appalachian orogen: A brief summary, in Tollo, R.P., Bartholomew, M.J., Hibbard, J.P., and Karabinos, P.M., eds., From Rodinia to Pangea: The Lithotectonic Record of the Appalachian Region: Geological Society of America Memoir 206, p. 1–19, doi: 10.1130/2010.1206(01).

He, Y., Li, S., Hoefs, J., Huang, F., Liu, S.-A., Hou, Z., 2011. Post-collisional granitoids from the Dabie orogen: new evidence for partial melting of a thickened continental crust. Geochimica et Cosmochimica Acta 75, 3815–3838

Heatherington, A.L., Mueller, P.A., Smith, M.S., and Nutman, A.P., 1996, The Corbin Gneiss: Evidence for Grenvillian magmatism and older continental basement in the southernmost Blue Ridge: Southeastern Geology, v. 36, p. 15–25.

Henderson, B. J., Collins, W. J., Murphy, J. B., & Hand, M. (2018). A hafnium isotopic record of magmatic arcs and continental growth in the Iapetus Ocean: The contrasting evolution of Ganderia and the peri-Laurentian margin. Gondwana Research, 58, 141-160.

Hibbard, J.P., van Staal, C.R., Rankin, D.W., 2010. Comparative analysis of the geological evolution of the northern and southern Appalachian orogen: Late Ordovician-Permian. Geological Society of America Memoirs 206, 51–69.

Hildebrand R S, Whalen J B, Bowring S A. 2018. Resolving the crustal composition paradox by 3.8 billion years of slab failure magmatism and collisional recycling of continental crust. Tectonophysics, 734-735: 69–88.

Hildebrand R S, Whalen J B. 2021. Arc and slab-failure magmatism of the Taconic orogeny,

western New England, USA. Geol Soc Lond Spec Publ, 503: 409–422.

Horton, J.D., 2017, The State Geologic Map Compilation (SGMC) geodatabase of the conterminous United States (ver. 1.1, August 2017): U.S. Geological Survey data release.

Ingram III, S. B. (2012). U-Pb zircon and monazite geochronology and hafnium isotopic geochemistry of Neoacadian and Early Alleghanian plutonic rocks in the Alabama Eastern Blue Ridge, Southern Appalachian Mountains. [Unpublished M.Sc. Thesis] The University of Alabama.

Jessberger, E. K., Huneke, J. C., Podosek, F. A., & Wasserburg, G. J. (1974). High resolution argon analysis of neutron-irradiated Apollo 16 rocks and separated minerals. In In: Lunar Science Conference, 5th, Houston, Tex., March 18-22, 1974, Proceedings. Volume 2.(A75-39540 19-91) New York, Pergamon Press, Inc., 1974, p. 1419-1449. Research supported by the Bundesministerium für Forschung und Technologie and National Research Council (Vol. 5, pp. 1419-1449).

Jourdan, F., and Renne, P.R., 2007, Age calibration of the Fish Canyon sanidine $^{40}Ar/^{39}Ar$ dating standard using primary K-Ar standards: Geochimica et Cosmochimica Acta, v. 71, p. 387–402, https://doi.org/10.1016/j. gca.2006.09.002.

Kay SM, Ramos VA, Marquez M (1993) Evidence in Cerro Pampa volcanic rocks of slab melting prior to ridge trench collision in southern South America. J Geol 101:703–714.

Kay, R.W., 1978. Aleutian magnesian andesites: melts from subducted Pacific Ocean crust. Journal of Volcanology and Geothermal Research 4, 117–132.

Kay, R.W., Kay, S.M., 1993. Delamination and delamination magmatism. Tectonophysics 219, 177–189.

Kelley, S. (2002). K-Ar and Ar-Ar dating. Reviews in Mineralogy and Geochemistry, 47(1), 785-818.

Konyshev, A. A., Chevychelov, V. Y., & Shapovalov, Y. B. (2020). Two types of highly differentiated topaz-bearing granites of the Salmi batholith, Southern Karelia. Geochemistry International, 58(1), 11-26.

Krol MA, Zeitler PK, Poupeau G, and Peˆcher A (1996) Temporal variations in the cooling and denudation history of the Hunza plutonic complex, Karakoram Batholith, revealed by 40Ar/39Ar thermochronology. Tectonics 15: 403–415.

Kuiper, K. F., Deino, A., Hilgen, F. J., Krijgsman, W., Renne, P. R., & Wijbrans, A. J. (2008). Synchronizing rock clocks of Earth history. science, 320(5875), 500-504.

Kusky, T., & Wang, L. (2022). Growth of continental crust in intra-oceanic and continental-margin arc systems: Analogs for Archean systems. Science China Earth Sciences, 65(9), 1615-1645.

Kusky, T.M., and Şengör, A.M.C., 2023, Comparative orotomy of the Archean Superior and Phanerozoic Altaid orogenic systems, *National Science Review*, 10: nwac235, 2023. invited, https://doi.org/10.1093/nsr/nwac235.

Kusky, T.M., and Wang, L., 2022, Growth of continental crust in intra-oceanic and continental margin arc systems: analogs for Archean systems, Science China Earth Sciences 65, 1615-1645. https://doi.org/10.1007/s11430-021-9964-1.

Kusky, T.M., Polat, A., Windley, B.F., Burke, K.C., Dewey, J.F., Kidd, W.S.F., Maruyama, S., Wang, J.P., Deng, H., Wang, Z.S. Wang, C., Fu, D., Li, X.W., and Peng, H.T., 2016, Insights into the tectonic evolution of the North China Craton through comparative

tectonic analysis: A record of outward growth of Precambrian continents, INVITED REVIEW, Earth Science Reviews, 162, 387-432, http://dx.doi.org/10.1016/j.earscirev.2016.09.002

Labails, C., Olivet, J. L., Aslanian, D., & Roest, W. R. (2010). An alternative early opening scenario for the Central Atlantic Ocean. Earth and Planetary Science Letters, 297(3-4), 355-368.

Li, C. F., Li, X. H., Li, Q. L., Guo, J. H., Li, X. H., & Yang, Y. H. (2012). Rapid and precise determination of Sr and Nd isotopic ratios in geological samples from the same filament loading by thermal ionization mass spectrometry employing a single-step separation scheme. Analytica chimica acta, 727, 54-60.

Ludwig, K. R. (2012). User's manual for Isoplot 3.75: A geochronological toolkit for Microsoft Excel. Berkeley Geochronology Center Special Publication, 5, 75.

Luhr, J. F., Carmichael, I. S.E., Varekamp, C. (1984). The 1982 eruptions of el chichon volcano, Chiapas, Mexico: Mineralogy and petrology of the anhydrite bearing pumices. Journal of Volcanology and Geothermal Research 23,69-108.

Ma, C., Foster, D. A., Hames, W. E., Mueller, P. A., & Steltenpohl, M. G. (2019). From the Alleghanian to the Atlantic: Extensional collapse of the southernmost Appalachian orogen. Geology, 47(4), 367-370.

Manning, D. A. C., & Hill, P. I. (1990). The petrogenetic and metallogenetic significance of topaz granite from the southwest England orefield.

Martin, H. (1986). Effect of steeper Archean geothermal gradient on geochemistry of subduction-zone magmas. Geology, 14(9), 753-756.

Martin, H., Smithies, R. H., Rapp, R., Moyen, J. F., & Champion, D. (2005). An overview of adakite, tonalite–trondhjemite–granodiorite (TTG), and sanukitoid: relationships and some implications for crustal evolution. Lithos, 79(1-2), 1-24.

McDonough, W. F., & Sun, S. S. (1995). The composition of the Earth. Chemical geology, 120(3-4), 223-253.

McDougall, I., Harrison, T.M., 1999. Geochronology and Thermochronology by the40Ar/39Ar method. Oxford University Press, Oxford (269 pp.).

McLelland, J.M., Daly, J.S., and Chiarenzelli, J., 1993, Sm-Nd and U-Pb isotopic evidence of juvenile crust in the Adirondack lowlands and implications for the evolution of the Adirondack Mts.: Journal of Geology, v. 101, p. 97–105

Meija, J., Coplen, T. B., Berglund, M., Brand, W. A., De Bièvre, P., Gröning, M., ... & Prohaska, T. (2016). Isotopic compositions of the elements 2013 (IUPAC Technical Report). Pure and Applied Chemistry, 88(3), 293-306.

Merrihue, C.M., and Turner, G., 1966, Potassium-argon dating by activation with fast neutrons: Journal of Geophysical Research, v. 71, p. 2852–2857, https://doi.org/10.1029/JZ071i011p02852.

Merschat, A. J., & Hatcher, R. D. (2007). The Cat Square terrane: possible Siluro-Devonian remnant ocean basin in the Inner Piedmont, southern Appalachians, USA.

Merschat, A.J., Hatcher, R.D., Jr, and Davis, T.L., 2005, The northern Inner Piedmont, southern Appalachians, USA: Kinematics of transpression and SW-directed mid-crustal flow. Journal of Structural Geology, v. 27 p. 1252-1281 doi: 10.1016/j.jsg.2004.08.005.

Míková, J. and Denková, P., 2007, Modified Chromatographic Separation Scheme for Sr and Nd

Isotope Analysis in Geological Silicate Samples. Journal of Geosciences, vol. 52, no. 3–4, pp. 221–26, https://doi.org/10.3190/jgeosci.015.

Miller, B. V., Fetter, A. H., & Stewart, K. G. (2006). Plutonism in three orogenic pulses, eastern Blue Ridge Province, southern Appalachians. Geological Society of America Bulletin, 118(1-2), 171-184.

Miller, B. V., Stewart, K. G., & Whitney, D. L. (2010). Three tectonothermal pulses recorded in eclogite and amphibolite of the Eastern Blue Ridge, southern Appalachians. Geological Society of America Memoirs, 206, 701-724.

Min, K., Mundil, R., Renne, P.R., and Ludwig, K.R., 2000, A test for systematic errors in 40Ar/39Ar geochronology through comparison with U/Pb analysis of a 1.1-Ga rhyolite: Geochimica et Cosmochimica Acta, v. 64, p. 73– 98, https://doi.org/10.1016/S0016-7037(99)00204

Moecher, D. P., Samson, S. D., and Miller, C. F., 2004, Precise time and conditions of peak Taconian granulite facies metamorphism in the Southern Appalachian Orogen, USA, with implications for zircon behavior during crustal melting events: The Journal of Geology, v. 112, n. 3, p. 289–304, https://doi.org/10.1086/382760

Mosher, S. (1998). Tectonic evolution of the southern Laurentian Grenville orogenic belt. Geological Society of America Bulletin, 110(11), 1357-1375.

Moyen, J. F. (2009). High Sr/Y and La/Yb ratios: the meaning of the “adakitic signature”. Lithos, 112(3-4), 556-574.

Moyen, J. F., Stevens, G., Kisters, A. F., & Belcher, R. W. (2007). TTG plutons of the Barberton granitoid-greenstone terrain, South Africa. Developments in Precambrian Geology, 15,

607-667.

Moyen, J., & Stevens, G. (2006). Experimental constraints on TTG petrogenesis: implications for Archean geodynamics. Geophysical Monograph-American Geophysical Union, 164, 149.

Moyen, J.F., Martin, H., 2012. Forty years of TTG research. Lithos148, 312–336. https://doi .org /10 .1016 /j .lithos .2012 .06 .010.

Nakamura, N. (1974). Determination of REE, Ba, Fe, Mg, Na and K in carbonaceous and ordinary chondrites. Geochimica et cosmochimica acta, 38(5), 757-775.

Nakamura, N. (1974). Determination of REE, Ba, Fe, Mg, Na and K in carbonaceous and ordinary chondrites. Geochimica et cosmochimica acta, 38(5), 757-775.

O'connor, J. T. (1965). A classification for quartz-rich igneous rocks based on feldspar ratios. US Geological Survey, Professional Papers 525B, B79-B84.

Owens, B. E., & Samson, S. D. (2004). Nd isotopic constraints on the magmatic history of the Goochland terrane, easternmost Grenvillian crust in the southern Appalachians.

Parsons I, Gerald JDF, Lee JKW, Ivanic T, and Golla-Schindler U (2010) Time–temperature evolution of microtextures and contained fluids in a plutonic alkali feldspar during heating. Contributions to Mineralogy and Petrology 160: 155–180.

Patchett, P.J., and Ruiz, J., 1989, Nd isotopes and the origin of Grenville-age rocks in Texas: Implications for Proterozoic evolution of the United States Mid-continent region: Journal of Geology, v. 97, p. 685–695.

Patiño Douce, A. E. and Beard, J. S. (1995). Dehydration-melting of biotite gneiss and quartz amphibolite from 3 to 15 kbar. Journal of Petrology, 36(3), 707-738.

Petford, N., & Atherton, M. (1996). Na-rich partial melts from newly underplated basaltic crust: the Cordillera Blanca Batholith, Peru. Journal of petrology, 37(6), 1491-1521.

Pettingill, H.S., Sinha, A.K., and Tatsumoto, M., 1984, Age and origin of anorthosites, charnockites, and granulites in the central Virginia Blue Ridge: Nd and Sr isotopic evidence: Contributions to Mineralogy and Petrology, v. 85, p. 279–291.

Poole, J. D. (2015). Geology of the Jacksons Gap, Alabama, 7.5-Minute Quadrangle: Implications for the Evolution of the Brevard Fault Zone Unpublished M.Sc. Thesis, Auburn University).

Pushkov, V.N., 1997, Structure and geodynamics of the Uralian orogen, in Burg, J.-P., and Ford, M., eds., Orogeny through Time: Geological Society of London Special Publication 121, p. 201–236.

Qian, Q., Hermann, J., 2013. Partial melting of lower crust at 10–15 kbar: constraints on adakite and TTG formation. Contrib. Mineral. Petrol.165, 1195–1224. https://doi .org /10 .1007 /s00410 -013 -0854 -9.

Qu, X., Hou, Z., and Li, Y., 2004, Melt components derived from a subducted slab in late orogenic ore-bearing porphyries in the Gangdese copper belt, southern Tibetan plateau: Lithos, v. 74, p. 131–148, https://doi. org/10.1016/j.lithos.2004.01.003.

R.P. Rapp, E.B. Watson, Dehydration melting of metabasalts at 8-32 kbar: implications for continental growth and crust-mantle recycling, J. Petrol. 36 (1995) 891-931.

Rast, N., and Skehan, J.W., 1983, The evolution of the Avalonian plate: Tectonophysics, v. 100, p. 257–286, doi: 10.1016/0040-1951(83)90191-9.

Ratajeski, K., Sisson, T. W., & Glazner, A. F. (2005). Experimental and geochemical evidence

for derivation of the El Capitan Granite, California, by partial melting of hydrous gabbroic lower crust. Contributions to Mineralogy and Petrology, 149, 713-734.

Reichardt, H.,Weinberg, R.F., 2012. Hornblende chemistry in meta- and diatexites and its retention in the source of leucogranites: an example fromthe KarakoramShear Zone, NW India. J. Petrol. 53, 1287–1318.

Robinson, P., Tucker, R.D., Bradley, D., Berry, H.N., IV, and Osberg, P.H., 1998, Paleozoic orogens in New England, USA: Geologiska Föreningensi Stockholm Förhandlingar, v. 120, p. 119–148.

Rollinson, H. R., & Pease, V. (2021). Using geochemical data: To understand geological processes. Cambridge University Press.

Rudnick RL, Gao S (2003) Composition of the continental crust. In: Rudnick RL, Holland HD, Turekian KK (eds) Treatise on geochemistry, vol 3, the crust, Elsevier, pp 1–64

Russell, G. S., 1978, U-Pb, Rb-Sr, and K-Ar isotopic studies bearing on the tectonic development of the southernmost Appalachian orogen, Alabama [Ph.D.]: Tallahassee, Florida State University, 196 p.

Russell, G.S., Odom, A.L., and Russell, C.W., 1987, U-Pb and Rb-Sr isotopic evidence for the age and origin of granitic rocks in the northern Alabama Piedmont in Drummond, M.S., and Green, N.L., eds., Granites of Alabama: Alabama Geological Survey Special Volume, p. 239- 249.

Schaen, A. J., Jicha, B. R., Hodges, K. V., Vermeesch, P., Stelten, M. E., Mercer, C. M., ... & Singer, B. S. (2021). Interpreting and reporting 40Ar/39Ar geochronologic data. GSA Bulletin, 133(3-4), 461-487.

Scotese, C.R., 2004. A continental drift flipbook. Journal of Geology 112, 729–741. Sevastjanova, I., Clements, B., Hall, R., Belousova, E.A., Griffin,W.L., Pearson, N., 2011. Granitic magmatism, basement ages, and provenance indicators in the Malay Peninsula: insights from detrital zircon U–Pb and Hf-isotope data. Gondwana Research 19, 1024–1039.

Shabani, A. A. T., Lalonde, A., and Whalen, J. B. (2003). Composition of biotite from granitic rocks of the canadian appalachian orogen: a potential tectonomagmatic indicator.

Shand, S. J. (1943). The Eruptive Rocks. New York, NY: John Wiley Publishers. p. 444.

Shellnutt, J. G., Vaughan, M. W., Lee, H. Y., & Iizuka, Y. (2020). Late Jurassic Leucogranites of Macau (SE China): A record of crustal recycling during the early Yanshanian Orogeny. Frontiers in Earth Science, 8, 311.

Size, W. B., and Dean, L. S., 1987, Structural petrology and petrogenesis of trondhjemite, northern Alabama Piedmont, in Drummond, M. S., and Green, N. L., eds., Granites of Alabama: Tuscaloosa, Geological Survey of Alabama, Special Publication, p. 73–96.

Skehan, J.W., and Rast, N., 1990, Pre-Mesozoic evolution of Avalon terranes of southern New England, in Socci, A.D., Skehan, J.W., and Smith, G.W., eds., Geology of the Composite Avalon Terrane of Southern New England : Geological Society of America Special Paper 245, p. 13–53.

Stampfli, G.M., Hochard, C., Vérard, C., Wilhem, C., 2013. The formation of Pangea. Tectonophysics 593, 1–19.

Steltenpohl, M. G., Schwartz, J. J., & Miller, B. V. (2013). Late to post-Appalachian strain partitioning and extension in the Blue Ridge of Alabama and Georgia. Geosphere, 9(3),

647-666.

Stern, R. J. (2002). Crustal evolution in the East African Orogen: a neodymium isotopic perspective. Journal of African Earth Sciences, 34(3-4), 109-117.

Stowell, H. H., Schwartz, J. J., Ingram III, S. B., Madden, J., Jernigan, C., Steltenpohl, M., & Mueller, P. (2019). Linking metamorphism, magma generation, and synorogenic sedimentation to crustal thickening during Southern Appalachian mountain building, USA. Lithosphere, 11(5), 722-749.

Sun, S. S., & McDonough, W. F. (1989). Chemical and isotopic systematics of oceanic basalts: implications for mantle composition and processes. Geological Society, London, Special Publications, 42(1), 313-345.

Thomas, W. A. (1977). Evolution of Appalachian-Ouachita salients and recesses from reentrants and promontories in the continental margin. American Journal of Science, Haque, Z., & Uddin, A. (2017). Carboniferous history from coarse detritus of the Appalachian-Cahaba system: Conglomerate clasts from the Upper Pottsville Formation, Cahaba Synclinorium, Alabama. The Journal of Geology, 125(1), 45-63. 277(10), 1233-1278.

Tollo, R. P., McLelland, J., Corriveau, L., & Bartholomew, M. J. (2004). Proterozoic tectonic evolution of the Grenville orogen in North America.

Tull, J. F., 1978, Structural development of the Alabama Piedmont northwest of the Brevard zone: American Journal of Science, v. 278, p. 442–460, doi: 10 .2475 /ajs.278 .4 .442.

Tull, J. F., Mueller, P. A., Farris, D. W., & Davis, B. L. (2018). Taconic suprasubduction zone magmatism in southern Laurentia: Evidence from the Dadeville Complex. Bulletin, 130(7-8), 1339-1354.

Tulloch, A. J., & Kimbrough, D. L. (2003). Paired plutonic belts in convergent margins and the development of high Sr/Y magmatism: Peninsular Ranges Batholith of Baja California and Median Batholith of New Zealand.

Turner, G. (1968). The distribution of potassium and argon in chondrites. In Origin and Distribution of the Elements (pp. 387-398). Pergamon.

Uchida, E., Endo, S., and Makino, M. (2007). Relationship between solidification depth of granitic rocks and formation of hydrothermal ore deposits. Resour. Geol. 57, 47–56. doi: 10.1111/j.1751-3928.2006.00004.x

Uchida, E., Endo, S., and Makino, M. (2007). Relationship between solidification depth of granitic rocks and formation of hydrothermal ore deposits. Resource Geol. 57, 47–56. doi: 10.1111/j.1751-3928.2006.00004.x

van Staal, C.R., MacNiocall, V., Valverde-Vaquero, P., Barr, S.M., Fyffe, L.R., and Reusch, D.N., 2004, Ganderia, Avalonia, and the Salinic and Acadian orogenies: Geological Society of America Abstracts with Programs, v. 36, no. 2, p. 128–129.

Walker, D., Driese, S. G., & Hatcher Jr, R. D. (1989). Paleotectonic significance of the quartzite of the Sauratown Mountains window, North Carolina. Geology, 17(10), 913-917.

Walther, C., & Wendt, K. (2020). Radioisotope mass spectrometry. In Handbook of Radioactivity Analysis (pp. 861-898). Academic Press.

Wang, J., Jiang, K., Xiao, D., Li, F., Li, F., Li, X., ... & Tao, G. (2022). Mineral Chemistry of Biotite and Its Petrogenesis Implications in ca. 2.5 Ga Wangjiazhuang Granitic Pluton, North China Craton. Journal of Earth Science, 1-14.

Wang, Q., Xu, J.-F., Jian, P., Bao, Z.-W., Zhao, Z.-H., Li, C.-F., Xiong, X.-L., Ma, J.-L., 2006.

Petrogenesis of adakitic porphyries in an extensional tectonic setting, Dexing, South China: implications for the genesis of porphyry copper mineralization. Journal of Petrology 47, 119–144.

Wang, X., Sun, M., Weinberg, R. F., Cai, K., Zhao, G., Xia, X., ... & Liu, X. (2022). Adakite generation as a result of fluid-fluxed melting at normal lower crustal pressures. Earth and Planetary Science Letters, 594, 117744.

Winter, J. D. (2013). Principles of igneous and metamorphic petrology. Pearson education.

Wones, D. R. (1981). Mafic silicates as indicators of intensive variables in granitic magmas. Mining Geology, 31(168), 191-212.

Yáñez, P., Ruiz, J., Patchett, P. J., Ortega-Gutiérrez, F., & Gehrels, G. E. (1991). Isotopic studies of the Acatlán Complex, southern Mexico: implications for Paleozoic North American tectonics. Geological Society of America Bulletin, 103(6), 817-828.

Zhao, J. H., Zhou, M. F., Zheng, J. P., & Griffin, W. L. (2013). Neoproterozoic tonalite and trondhjemite in the Huangling complex, South China: Crustal growth and reworking in a continental arc environment. American Journal of Science, 313(6), 540-583.

Zhou, X. C., Zhang, H. F., Luo, B. J., Pan, F. B., Zhang, S. S., & Guo, L. (2016). Origin of high Sr/Y-type granitic magmatism in the southwestern of the Alxa Block, Northwest China. Lithos, 256, 211-227.

Zou, H. (1999). Studies of mantle melting process and compositions using major and trace elements, neodymium-strontium-lead isotopic systematics, and uranium series disequilibria: mathematical modeling and experimental analyses. The Florida State University (Ph.D. Thesis).

Zou, H., Fan, Q., Schmitt, A. K., & Sui, J. (2010). U–Th dating of zircons from Holocene potassic andesites (Maanshan volcano, Tengchong, SE Tibetan Plateau) by depth profiling: time scales and nature of magma storage. Lithos, 118(1-2), 202-210.

Zou, H., Zindler, A., Xu, X., & Qi, Q. (2000). Major, trace element, and Nd, Sr and Pb isotope studies of Cenozoic basalts in SE China: mantle sources, regional variations, and tectonic significance. Chemical Geology, 171(1-2), 33-47.

7. Appendices

Appendix A: Compiled dataset for high Sr/Y EBR plutons. BF: Blakes Ferry, ALM: Almond W: Wedowee.

1: Deininger et al. (1973), 2: Size and Dean (1987), 3: Ingram (2012).

	1	1	1	1	1	1	1	1	1	1	2	2	2	2	2	2
Name	ALM	ALM	ALM	ALM	ALM	ALM	ALM	ALM	ALM	ALM	ALM	ALM	ALM	ALM	ALM	ALM
SiO_2	70.2	70.1	72.5	71.0	70.2	70.1	70.8	70.6	71.8	73.1	72.3	71.9	73.8	75.7	70.9	71.5
TiO_2	0.2	0.2		0.2	0.3	0.1		0.2	0.3	0.2	0.3	0.2	0.2	0.1	0.1	0.2
Al_2O_3	15.8	17.4	17.5	16.9	15.6	17.1	17.6	16.7	15.3	15.5	16.2	15.9	14.8	15.1	15.3	15.4
$Fe_2O_3\_t$	1.6	2.0	1.3	2.1	2.3	0.9	0.1	1.1	2.3	0.8	1.9	1.4	1.8	0.9	1.3	1.7
MnO	0.0	0.1	0.0	0.0	0.0	0.0	0.0	0.0	0.0	0.0	0.0	0.0	0.0	0.0	0.0	0.0
MgO	0.4	0.5	0.1	0.4	0.5	0.4	0.0	0.5	0.6	0.2	0.7	0.4	0.6	0.3	0.3	0.5
CaO	2.0	2.2	2.5	2.0	2.0	2.4	2.5	2.3	1.7	1.9	2.9	1.4	1.6	1.0	1.7	1.6
Na_2O	5.5	4.9	6.0	5.7	5.3	6.4	6.4	5.5	4.6	5.3	5.2	5.6	5.1	5.5	5.6	5.3
K_2O	1.9	2.2	0.2	1.9	2.5	2.9	1.1	1.5	2.0	2.5	1.7	2.3	2.2	2.3	1.9	1.7
P_2O_5	1.3	0.7	0.1	0.2	0.8	0.4	1.0	0.6	1.0	0.7	0.1	0.0	0.1	0.1	0.1	0.1
LOI	1.3	0.7	0.1	0.2	0.8	0.4	1.0	0.6	1.0	0.7	1.0	0.7	1.0	1.4	1.8	0.8
Total	98.9	100.2	100.2	100.4	98.4	100.8	99.9	98.9	99.6	100.3	102.2	99.8	101.1	102.3	99.0	98.7
V											29.5	17.4	22.0	11.6	12.0	17.3
Cr											108.0	120.0	13.9	7.1	98.0	11.0
Ni											12.0	6.0	9.0	8.0	6.0	8.0
Cu											11.4	10.8	5.9	10.7	33.9	14.8
Zn											39.0	44.0	48.0	29.0	39.0	44.0
Rb											30.0	31.0	45.0	47.0	39.0	36.0
Sr											558.0	549.0	499.0	409.0	320.0	458.0
Y																
Zr											17.0	29.0	30.0	28.0	27.0	26.0
Nb																
Ba											504.0		569.0	594.0		
Mo																
Pb											10.0	10.0	10.0	20.0	10.0	10.0
Th											4.4			2.1	2.0	
U											0.6			0.8	1.4	
La											20.0			10.0	8.7	
Ce											46.0			20.0	20.0	
Pr																
Nd											23.0			11.0	9.0	
Sm											4.0			2.3	2.0	
Eu											2.1			0.6	0.4	
Gd																
Tb											0.5			0.4	0.3	
Dy											0.9			1.7	1.3	
Ho																
Er																
Tm																
Yb											1.5			0.7	0.7	
Lu											0.2			0.1	0.1	
Tl																
Ta																
Sn																
Li																
Be											0.9	1.0	1.3	1.5	1.5	1.3
Co													58.0	66.0		
Cs																
Ga																
Hf																

	2	2	2	3	3	3	3	2	2	2	2	2	2	3	3	3
Name	ALM	ALM	ALM	ALM	ALM	ALM	ALM	BF	BF	BF	BF	BF	BF	BF	BF	BF
SiO_2	74.4	69.8	67.8	72.9	72.6	72.6	72.3	76.5	73.5	67.5	71.1	74.0	72.6	68.0	71.4	65.2
TiO_2	0.1	0.2	0.3	0.1	0.1	0.1	0.1	0.6	0.2	0.1	0.3	0.2	0.0	0.1	0.1	0.6
Al_2O_3	14.2	14.7	15.5	15.4	15.2	15.3	15.2	12.0	15.8	14.7	15.4	14.7	14.8	19.7	17.1	17.5
Fe_2O_3_t	1.0	2.1	3.2	0.5	0.6	0.5	0.4	3.5	1.2	0.8	1.6	1.1	0.2	0.6	1.3	5.1
MnO	0.0	0.0	0.1	0.0	0.0	0.0	0.0	0.0	0.0	0.0	0.0	0.0	0.0		0.0	0.1
MgO	0.3	0.6	0.9	0.1	0.2	0.1	0.1	1.3	0.4	0.3	0.5	0.4	0.1	0.2	0.3	1.7
CaO	1.4	2.5	1.4	1.0	1.8	1.7	1.7	1.4	2.3	2.1	2.2	2.1	2.2	2.4	1.8	3.3
Na_2O	4.9	4.5	4.0	5.6	5.9	5.7	5.6	3.1	5.5	5.3	5.1	5.1	5.6	7.5	5.9	4.2
K_2O	2.5	2.0	3.0	2.0	1.9	2.0	2.0	2.6	1.7	1.4	1.8	1.6	1.3	1.4	2.0	2.2
P_2O_5	0.1	0.1	0.0	0.0	0.1	0.1	0.0	0.1	0.1	0.0	0.1	0.0	0.0	0.0	0.1	0.1
LOI	1.6	0.7	1.8	1.6	1.6	1.9	2.5	1.2	0.5	0.1	0.3	0.5	0.3	0.0	0.0	0.0
Total	100.5	97.2	98.1	99.2	100.0	100.0	99.9	102.4	101.1	92.4	98.4	99.7	97.1	99.9	100.0	100.0
V	11.3	23.5	25.2	10.4	10.2	29.4	9.0	43.4	14.7	10.4	18.9	13.5	4.4	14.2	12.0	11.8
Cr	8.4	16.5	87.5					19.5	8.9	4.9	10.8	9.8	4.0			
Ni	6.0	9.0	9.0	2.0	2.4	3.8	1.6	8.0	8.0	7.0	6.0	5.0	8.0	2.4	2.2	2.4
Cu	6.8	5.7	595.0	4.4	2.8	8.4	3.8	2.8	2.3		2.8	3.5	3.7	13.4	2.6	7.0
Zn	29.0	48.0	80.0	18.2	20.8	47.2	18.2	138.0	54.0	35.0	61.0	55.0	11.0	33.2	31.2	23.4
Rb	51.0	35.0	78.0	42.8	39.8	39.6	45.8	57.0	29.0	20.0	32.0	24.0	10.0	20.0	24.6	20.4
Sr	325.0	481.0	274.0	568.2	589.2	529.2	516.2	471.0	807.0	759.0	769.0	769.0	787.0	925.4	999.2	1017.4
Y				3.2	4.0	6.2	3.6							1.8	1.0	12.0
Zr	24.0	27.0	38.0	98.6	116.8	152.2	88.0	44.0	33.0	30.0	37.0	35.0	27.0	155.6	153.6	156.2
Nb				3.2	3.0	4.2	3.0							2.2	2.2	2.0
Ba	594.0	344.0		390.0	339.6	434.4	391.0	728.0	544.0	417.0	562.0	514.0	450.0	501.8	563.2	545.8
Mo				11.0	11.0	8.0	11.0							11.0	11.0	11.0
Pb	15.0	10.0	10.0	9.9	11.3	10.5	13.2	5.0	5.0	10.0	5.0	5.0	10.0	10.8	10.3	9.6
Th				0.2	0.4	4.2	0.5	3.2	1.9			1.3		1.1	0.6	0.6
U				5.0	5.0	4.0	5.0	0.6	0.7			5.0		0.4	0.2	0.2
La				1.1	4.4	16.7	2.5	14.0	7.9			6.3		6.9	5.7	4.8
Ce				5.2	9.3	34.8	6.9	28.0	16.0			12.0		11.9	9.0	8.0
Pr				0.3	1.1	4.1	0.6							1.4	1.1	0.9
Nd				1.1	4.5	16.0	2.5	15.0	10.0			5.0		5.2	4.1	3.5
Sm				0.1	0.8	0.6	0.4	2.7	1.6			1.2		1.0	0.7	0.6
Eu				0.0	0.3	2.7	0.1	0.4	0.7			0.7		0.5	0.5	0.4
Gd																
Tb				0.0	0.1	0.2	0.1	0.2	0.2			0.2		0.1	0.1	0.1
Dy				0.2	0.7	1.3	0.4	0.6	0.8			0.5		0.3	0.3	0.3
Ho				0.0	0.1	0.2	0.1							0.1	0.0	0.0
Er				0.1	0.4	0.6	0.2							0.1	0.1	0.1
Tm																
Yb				0.1	0.3	0.5	0.1	0.4	0.3			0.3		0.1	0.1	0.1
Lu				0.0	0.0	0.1	0.0	0.0	0.0			0.0		0.0	0.0	0.0
Tl																
Ta																
Sn																
Li								46.0	54.0	63.0	38.0	32.0	50.0			
Be	1.5	0.9	1.6					2.3	2.1	4.8	2.2	3.2	1.9			
Co	61.0	58.0	10.0					42.0	43.0	45.0	43.0	38.0	40.0			
Cs																
Ga																
Hf																

	3	3	3	3	3	3
Name	BF	BF	W	W	W	W
SiO_2	67.2	70.3	69.3	69.7	70.3	69.6
TiO_2	0.1	0.1	0.1	0.1	0.2	0.2
Al_2O_3	20.1	17.9	18.9	17.4	16.6	16.7
Fe_2O_3_t	0.8	0.9	0.4	1.0	1.3	1.2
MnO				0.0	0.0	0.0
MgO	0.3	0.3	0.1	0.3	0.4	0.5
CaO	2.4	2.4	6.0	2.0	0.0	1.0
Na_2O	7.5	6.7	7.3	6.3	5.9	5.8
K_2O	1.6	1.3	1.3	1.8	1.9	2.2
P_2O_5	0.0	0.0	0.0	0.1	0.1	0.1
LOI	0.0	0.0	0.0	1.0	1.4	1.7
Total	100.0	99.9	103.4	99.7	98.1	99.0
V	9.8	16.2	16.4	17.2	19.2	17.2
Cr						
Ni	1.8	2.0	2.6	2.8	2.6	2.6
Cu	5.2	2.8	5.2	4.8	6.0	8.2
Zn	17.0	38.0	31.2	29.4	34.2	33.6
Rb	15.2	23.8	50.0	41.0	44.0	49.8
Sr	995.2	989.8	491.8	520.6	527.4	503.8
Y	1.2	2.0	7.4	4.6	5.8	6.4
Zr	148.0	159.2	107.4	108.2	113.0	107.4
Nb	1.8	2.2	3.8	3.2	3.2	4.0
Ba	499.6	545.8	592.0	570.2	555.2	434.4
Mo	12.0	10.0	10.0	10.0	9.6	11.0
Pb			10.7	14.7	14.9	15.6
Th			1.5	2.4	2.2	2.3
U			0.4	1.0	0.8	0.8
La			10.7	9.7	9.0	9.4
Ce			18.9	21.1	19.5	20.0
Pr			2.2	2.5	2.3	2.4
Nd			8.4	9.8	9.1	9.2
Sm			1.8	1.8	1.6	1.7
Eu			0.5	0.4	0.4	0.4
Gd						
Tb			0.2	0.2	0.2	0.2
Dy			0.9	1.2	1.0	1.3
Ho			0.2	0.2	0.2	0.2
Er			0.4	0.5	0.4	0.6
Tm						
Yb			0.3	0.4	0.4	0.6
Lu			0.1	0.1	0.1	0.1
Tl						
Ta						
Sn						
Li						
Be						
Co						
Cs						
Ga						
Hf						

Appendix B: Selected few of biotite EPMA data.

Measured (wt %)	SiO2	39.74	36.44	36.42	36.40	36.37	36.31	36.31	36.30	36.05	36.03	35.94	35.93	35.92	36.29	36.27	36.26	39.09	38.48
	TiO2	1.81	2.93	3.14	3.20	2.23	2.17	2.39	2.39	2.42	2.21	2.12	2.40	2.47	2.05	2.06	1.71	3.00	2.81
	Al2O3	16.36	16.28	17.61	16.13	18.70	17.88	18.70	18.34	17.32	19.85	17.20	17.79	17.74	17.68	17.71	18.47	16.89	15.84
	FeO	18.71	20.54	20.92	20.51	20.87	20.70	19.49	20.88	19.39	19.28	20.61	19.44	20.75	20.32	20.50	20.22	19.23	19.88
	MnO	0.54	0.25	0.18	0.18	0.19	0.29	0.31	0.24	0.28	0.23	0.26	0.21	0.23	0.18	0.24	0.21	0.59	0.50
	MgO	9.09	9.08	9.03	8.91	9.51	9.19	8.87	9.61	9.07	8.37	9.33	9.33	9.67	8.91	9.01	9.30	7.61	7.78
	CaO	0.35	0.00	0.02	0.03	0.17	0.06	0.30	0.09	0.31	0.32	0.06	0.14	0.16	0.12	0.12	0.09	0.16	0.09
	Na2O	0.13	0.03	0.00	0.06	0.14	0.16	0.72	0.69	0.32	0.49	0.00	0.00	0.17	0.12	0.09	0.33	0.08	0.00
	K2O	7.60	9.58	10.11	9.67	9.75	9.80	8.84	10.04	8.97	8.35	9.63	9.04	9.53	9.36	9.68	8.95	8.06	8.87
	Σ	**94.32**	**95.13**	**97.43**	**95.09**	**97.93**	**96.57**	**95.93**	**98.59**	**94.12**	**95.13**	**95.15**	**94.28**	**96.63**	**95.03**	**95.69**	**95.54**	**94.71**	**94.25**
T	Si	5.98	5.60	5.48	5.60	5.43	5.50	5.48	5.40	5.56	5.45	5.53	5.52	5.44	5.56	5.54	5.51	5.90	5.90
	Al (IV)	2.02	2.40	2.52	2.40	2.57	2.50	2.52	2.60	2.44	2.55	2.47	2.48	2.56	2.44	2.46	2.49	2.10	2.10
	Σ	**8.00**	**8.00**	**8.00**	**8.00**	**8.00**	**8.00**	**8.00**	**8.00**	**8.00**	**8.00**	**8.00**	**8.00**	**8.00**	**8.00**	**8.00**	**8.00**	**8.00**	**8.00**
M	Al (VI)	0.89	0.55	0.60	0.53	0.71	0.69	0.81	0.62	0.71	0.99	0.65	0.74	0.61	0.75	0.72	0.82	0.90	0.76
	Ti	0.20	0.34	0.36	0.37	0.25	0.25	0.27	0.27	0.28	0.25	0.24	0.28	0.28	0.24	0.24	0.20	0.34	0.32
	Fe	2.36	2.64	2.63	2.64	2.60	2.62	2.46	2.60	2.50	2.44	2.65	2.50	2.63	2.60	2.62	2.57	2.43	2.55
	Mn	0.07	0.03	0.02	0.02	0.02	0.04	0.04	0.03	0.04	0.03	0.03	0.03	0.03	0.02	0.03	0.03	0.07	0.06
	Mg	2.04	2.08	2.02	2.04	2.11	2.08	2.00	2.13	2.08	1.89	2.14	2.14	2.18	2.04	2.05	2.11	1.71	1.78
	Σ	**5.56**	**5.64**	**5.63**	**5.60**	**5.71**	**5.67**	**5.58**	**5.65**	**5.61**	**5.60**	**5.71**	**5.68**	**5.73**	**5.65**	**5.66**	**5.71**	**5.45**	**5.47**
I	Ca	0.06	0.00	0.00	0.00	0.03	0.01	0.05	0.01	0.05	0.05	0.01	0.02	0.03	0.02	0.02	0.01	0.03	0.02
	Na	0.04	0.01	0.00	0.02	0.04	0.05	0.21	0.20	0.09	0.14	0.00	0.00	0.05	0.04	0.03	0.10	0.02	0.00
	K	1.46	1.88	1.94	1.90	1.86	1.89	1.70	1.91	1.76	1.61	1.89	1.77	1.84	1.83	1.88	1.73	1.55	1.73
	Σ	**1.55**	**1.89**	**1.94**	**1.92**	**1.92**	**1.95**	**1.96**	**2.12**	**1.91**	**1.81**	**1.90**	**1.79**	**1.92**	**1.88**	**1.93**	**1.85**	**1.60**	**1.75**
	Fe/(Fe+Mg)	0.54	0.56	0.57	0.56	0.55	0.56	0.55	0.55	0.55	0.56	0.55	0.54	0.55	0.56	0.56	0.55	0.59	0.59
	Al (Total)	2.90	2.95	3.12	2.93	3.29	3.19	3.33	3.22	3.15	3.54	3.12	3.22	3.17	3.19	3.19	3.31	3.00	2.86
	T (C°)	611.97	652.51	659.32	664.88	620.83	618.99	634.55	627.27	636.15	627.35	617.11	635.27	631.14	615.44	615.40	601.96	664.86	651.20
	Mean Depth	11.42	11.98	14.07	11.69	16.08	14.92	16.56	15.23	14.38	19.13	14.02	15.28	14.61	14.94	14.85	16.31	12.62	10.90

Measured (wt %)	SiO2	38.32	38.29	38.24	38.23	37.99	37.95	37.94	37.94	37.91	37.90	37.76	37.75	37.70	37.66	37.65	37.63	37.63
	TiO2	2.29	1.96	1.67	2.17	2.12	2.20	2.75	1.25	2.87	2.75	2.34	1.73	3.09	1.52	1.91	2.63	2.40
	Al2O3	17.25	18.13	19.00	18.04	19.13	17.85	15.31	17.53	15.94	15.65	17.48	17.95	15.22	16.82	18.98	15.44	17.68
	FeO	19.72	18.70	19.65	18.98	18.19	19.44	19.32	18.59	19.90	20.61	20.70	19.90	19.94	19.94	20.04	20.33	19.10
	MnO	0.29	0.23	0.23	0.26	0.24	0.24	0.51	0.43	0.50	0.62	0.32	0.20	0.56	0.46	0.22	0.43	0.48
	MgO	9.10	8.96	8.40	9.25	8.74	8.92	8.37	9.25	7.66	7.94	8.71	9.29	8.55	8.55	8.80	8.25	7.87
	CaO	0.06	0.16	0.26	0.06	0.19	0.04	0.22	0.23	0.26	0.09	0.18	0.14	0.20	0.14	0.18	0.25	0.27
	Na2O	0.14	0.31	0.00	0.40	0.61	0.32	0.02	0.08	0.04	0.10	0.26	0.03	0.12	0.07	0.00	0.03	0.16
	K2O	9.49	8.43	8.67	8.93	8.08	9.38	8.61	7.84	8.24	9.08	9.88	9.38	8.58	8.29	9.04	8.16	7.48
	Σ	**96.65**	**95.16**	**96.12**	**96.32**	**95.29**	**96.35**	**93.05**	**93.15**	**93.32**	**94.73**	**97.63**	**96.36**	**93.95**	**93.46**	**96.82**	**93.15**	**93.07**
T	Si	5.73	5.75	5.70	5.70	5.67	5.68	5.88	5.81	5.86	5.82	5.64	5.66	5.81	5.81	5.61	5.84	5.77
	Al (IV)	2.27	2.25	2.30	2.30	2.33	2.32	2.12	2.19	2.14	2.18	2.36	2.34	2.19	2.19	2.39	2.16	2.23
	Σ	**8.00**	**8.00**	**8.00**	**8.00**	**8.00**	**8.00**	**8.00**	**8.00**	**8.00**	**8.00**	**8.00**	**8.00**	**8.00**	**8.00**	**8.00**	**8.00**	**8.00**
M	Al (VI)	0.77	0.95	1.04	0.86	1.04	0.84	0.68	0.97	0.76	0.66	0.72	0.84	0.58	0.86	0.94	0.67	0.97
	Ti	0.26	0.22	0.19	0.24	0.24	0.25	0.32	0.14	0.33	0.32	0.26	0.19	0.36	0.18	0.21	0.31	0.28
	Fe	2.47	2.35	2.45	2.36	2.27	2.44	2.50	2.38	2.57	2.65	2.59	2.50	2.57	2.57	2.50	2.64	2.45
	Mn	0.04	0.03	0.03	0.03	0.03	0.03	0.07	0.06	0.07	0.08	0.04	0.03	0.07	0.06	0.03	0.06	0.06
	Mg	2.03	2.00	1.87	2.05	1.95	1.99	1.93	2.11	1.76	1.82	1.94	2.08	1.97	1.97	1.95	1.91	1.80
	Σ	**5.56**	**5.55**	**5.58**	**5.56**	**5.52**	**5.54**	**5.51**	**5.65**	**5.50**	**5.52**	**5.55**	**5.63**	**5.55**	**5.64**	**5.63**	**5.58**	**5.55**
I	Ca	0.01	0.02	0.04	0.01	0.03	0.01	0.04	0.04	0.04	0.01	0.03	0.02	0.03	0.02	0.03	0.04	0.05
	Na	0.04	0.09	0.00	0.12	0.18	0.09	0.01	0.02	0.01	0.03	0.07	0.01	0.04	0.02	0.00	0.01	0.05
	K	1.81	1.61	1.65	1.70	1.54	1.79	1.70	1.53	1.62	1.78	1.88	1.80	1.69	1.63	1.72	1.62	1.46
	Σ	**1.86**	**1.73**	**1.69**	**1.82**	**1.75**	**1.89**	**1.75**	**1.59**	**1.68**	**1.82**	**1.99**	**1.82**	**1.76**	**1.67**	**1.75**	**1.67**	**1.56**
	Fe/(Fe+Mg)	0.55	0.54	0.57	0.54	0.54	0.55	0.56	0.53	0.59	0.59	0.57	0.55	0.57	0.57	0.56	0.58	0.58
	Al (Total)	3.04	3.21	3.34	3.17	3.37	3.15	2.80	3.16	2.90	2.83	3.08	3.17	2.77	3.06	3.33	2.83	3.20
	T (C°)	628.71	618.83	602.35	626.92	629.08	626.24	651.98	588.11	654.06	643.97	626.07	603.69	663.88	595.30	610.76	640.49	636.91
	Mean Depth	13.08	15.10	16.71	14.63	17.03	14.43	10.14	14.55	11.42	10.58	13.54	14.70	9.76	13.29	16.61	10.48	14.97

Appendix C: BSE and elemental abundance maps from the sample AMD-2.

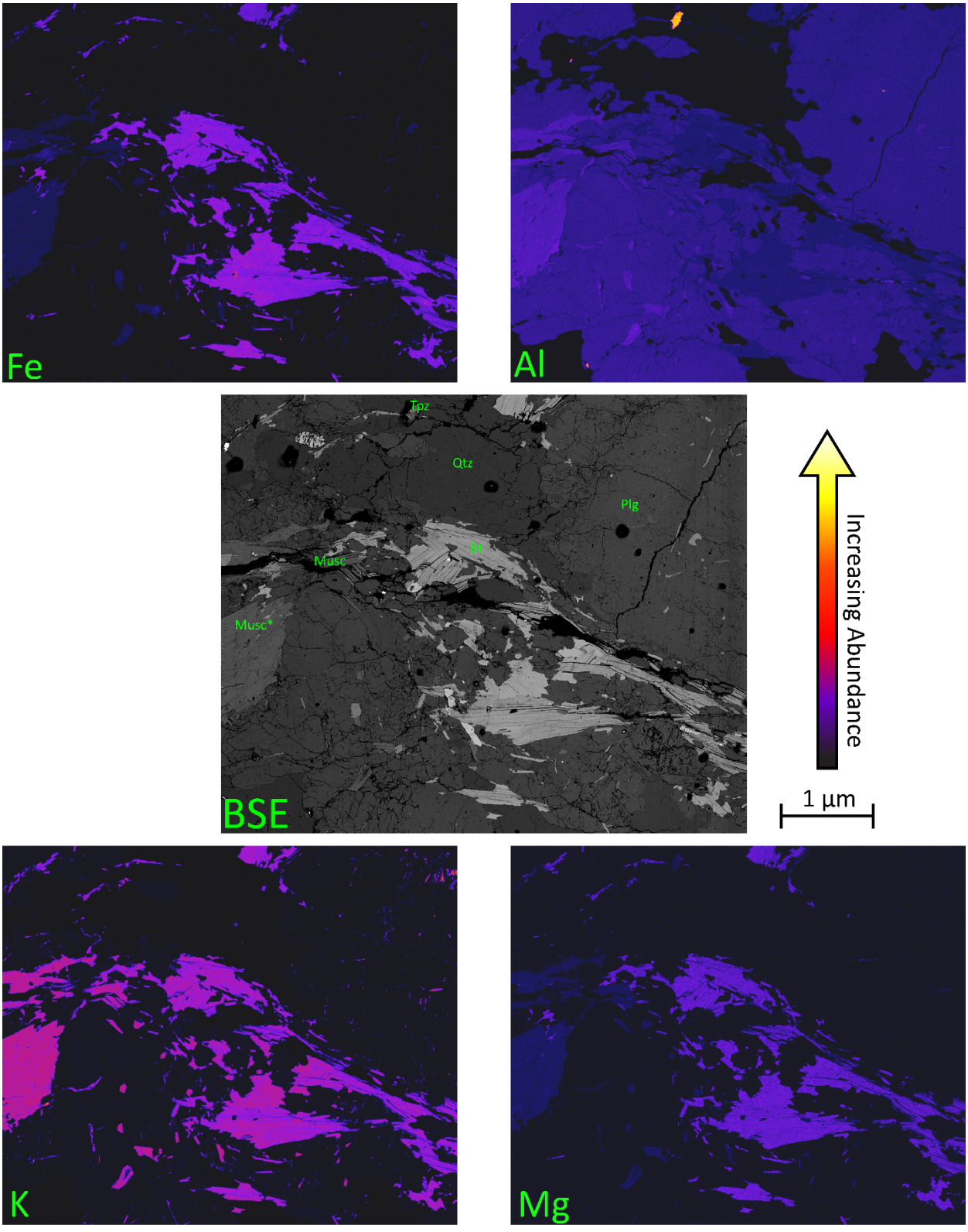

Appendix D: $^{40}Ar/^{39}Ar$ results.

Irradiation Package: AU-39
Median Date of Irradiation: 3/12/23
Median Date of Analyses: 5/5/2023
J Value: 0.0040444±0.0000038 (2σ)
Measured $^{40}Ar/^{36}Ar$ of Air during analyses: 293.6±1.0
Irradiation Production Factors:
(36/37)Ca: 0.0003046±0.0000084
(39/37)Ca: 0.0007380±0.0000370
(40/39)K: 0±0.0044
(38/39)Cl: 0.01±0.01

individual
he standard

confidence
), t = laser
lank, mass

error in
e.

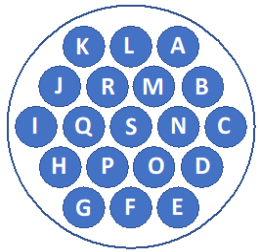

The rubric for irradiation filenames is: 'AU + package"+ "layer, radial position" + "phase" + "planchet hole # and sequence", saved as a text file. All samples for this study were within layer 2 of AU39, with positions labeled as in sketch to the right, and the monitor data for these layers are included in the dataset below.

Flux Monitors	P	t	40 V	39 V	38 V	37 V	36 V	Moles 40Ar*	% Rad	R	J-Value	% -sd
au39.2c.san.26a	3.2	15	9.91731 ± 0.002490	2.57485 ± 0.002460	0.00727 ± 0.000021	0.01686 ± 0.000116	0.000152 ± 0.000017	6.75E-14	99.5%	3.834128	169.53 ± 0.19	0.1%
au39.2c.san.27a	3.2	15	9.58160 ± 0.008110	2.49442 ± 0.006014	0.00678 ± 0.000022	0.01822 ± 0.000183	0.000093 ± 0.000016	6.52E-14	99.7%	3.830214	169.36 ± 0.44	0.3%
au39.2c.san.28a	3.2	15	11.74263 ± 0.033931	2.99961 ± 0.003827	0.00783 ± 0.000031	0.02038 ± 0.000101	0.000864 ± 0.000021	7.99E-14	97.8%	3.829648	169.34 ± 0.55	0.3%
au39.2c.san.29a	3.2	15	6.14244 ± 0.003286	1.59668 ± 0.003084	0.00479 ± 0.000040	0.01126 ± 0.000127	0.000114 ± 0.000020	4.18E-14	99.5%	3.825954	169.18 ± 0.38	0.2%
au39.2c.san.30a	3.2	15	12.21166 ± 0.004324	3.13861 ± 0.004234	0.00866 ± 0.000036	0.02461 ± 0.000077	0.000497 ± 0.000031	8.31E-14	98.8%	3.844011	169.94 ± 0.27	0.2%
au39.2g.san.31a	3.2	15	12.20903 ± 0.005064	3.15287 ± 0.001575	0.00967 ± 0.000043	0.03562 ± 0.000098	0.000301 ± 0.000018	8.31E-14	99.3%	3.844176	169.95 ± 0.14	0.1%
au39.2g.san.32a	3.2	15	4.07653 ± 0.003225	1.04453 ± 0.001865	0.00300 ± 0.000015	0.00683 ± 0.000070	0.000250 ± 0.000019	2.77E-14	98.2%	3.831982	169.43 ± 0.42	0.2%
au39.2g.san.33a	3.2	15	15.82876 ± 0.017857	4.06913 ± 0.006846	0.02130 ± 0.000093	0.03591 ± 0.000133	0.000762 ± 0.000033	1.08E-13	98.6%	3.834643	169.55 ± 0.36	0.2%
au39.2g.san.34a	3.2	15	18.91397 ± 0.009960	4.89707 ± 0.007487	0.01409 ± 0.000074	0.03445 ± 0.000155	0.000537 ± 0.000019	1.29E-13	99.2%	3.829916	169.35 ± 0.28	0.2%
au39.2g.san.35a	3.2	15	9.84533 ± 0.005511	2.54665 ± 0.004100	0.00733 ± 0.000034	0.01669 ± 0.000111	0.000321 ± 0.000017	6.70E-14	99.0%	3.828699	169.30 ± 0.30	0.2%
au39.2k.san.36a	3.2	15	8.73780 ± 0.005141	2.24376 ± 0.002600	0.00648 ± 0.000030	0.01968 ± 0.000208	0.000376 ± 0.000022	5.94E-14	98.7%	3.844718	169.97 ± 0.26	0.2%
au39.2k.san.37a	3.2	15	13.23427 ± 0.016710	3.43364 ± 0.006194	0.01019 ± 0.000089	0.02398 ± 0.000240	0.000159 ± 0.000018	9.00E-14	99.6%	3.840599	169.80 ± 0.38	0.2%
au39.2k.san.38a	3.2	15	8.60777 ± 0.005940	2.24584 ± 0.003777	0.00615 ± 0.000033	0.01719 ± 0.000156	0.000014 ± 0.000014	5.86E-14	100.0%	3.830953	169.39 ± 0.33	0.2%

au39.2k.san.39a	3.2	15	8.67989 ± 0.004835	2.24338 ± 0.004475	0.00718 ± 0.000035	0.01590 ± 0.000100	0.000313 ± 0.000020	5.91E-14	98.9%	3.827916	169.26 ± 0.37	0.2%
au39.2k.san.40a	3.2	15	11.69851 ± 0.005084	3.03749 ± 0.002454	0.00867 ± 0.000049	0.02088 ± 0.000198	0.000105 ± 0.000017	7.96E-14	99.7%	3.841157	169.82 ± 0.17	0.1%
au39.2s.san.41a	3.2	15	14.98674 ± 0.031510	3.87554 ± 0.003249	0.01056 ± 0.000045	0.02846 ± 0.000094	0.000141 ± 0.000014	1.02E-13	99.7%	3.856291	170.46 ± 0.39	0.2%
au39.2s.san.42a	3.2	15	12.71215 ± 0.035885	3.30007 ± 0.003671	0.00936 ± 0.000061	0.02283 ± 0.000104	0.000232 ± 0.000009	8.65E-14	99.5%	3.831321	169.41 ± 0.52	0.3%
au39.2s.san.43a	3.2	15	10.38485 ± 0.031395	2.68401 ± 0.003795	0.00820 ± 0.000067	0.03624 ± 0.000151	0.000379 ± 0.000017	7.07E-14	98.9%	3.827431	169.24 ± 0.58	0.3%
au39.2s.san.44a	3.2	15	10.75772 ± 0.028367	2.67703 ± 0.003275	0.01003 ± 0.000057	0.02388 ± 0.000069	0.001540 ± 0.000016	7.32E-14	95.8%	3.848569	170.14 ± 0.52	0.3%
au39.2s.san.45a	3.2	15	4.78699 ± 0.013061	1.23773 ± 0.001080	0.00309 ± 0.000015	0.00845 ± 0.000075	0.000039 ± 0.000006	3.26E-14	99.8%	3.858308	170.55 ± 0.49	0.3%

Sample	P	t	40 V	39 V	38 V	37 V	36 V	Moles 40Ar*	% Rad	R	Age (Ma)	% -sd
AT-1 | Single Crystal Total Fusion | 0.425-0.25mm | Muscovite												
au39.2e.mus.5a	3.2	20	3.47144 ± 0.001700	0.07185 ± 0.000143	0.00018 ± 0.000005	0.00107 ± 0.000086	0.000256 ± 0.000008	2.36E-14	97.8%	47.262678	320.19 ± 0.71	0.2%
au39.2e.mus.6a	3.2	20	7.76871 ± 0.003726	0.16408 ± 0.000287	0.00053 ± 0.000004	0.00291 ± 0.000143	0.000139 ± 0.000013	5.29E-14	99.5%	47.096934	319.16 ± 0.60	0.2%
au39.2e.mus.7a	3.2	20	7.78289 ± 0.011939	0.16230 ± 0.000653	0.00053 ± 0.000007	0.01649 ± 0.000241	0.000441 ± 0.000009	5.29E-14	98.3%	47.149794	319.49 ± 1.40	0.4%
au39.2e.mus.8a	3.2	20	4.60830 ± 0.006931	0.09679 ± 0.000364	0.00028 ± 0.000005	0.00008 ± 0.000065	0.000094 ± 0.000008	3.14E-14	99.4%	47.325239	320.58 ± 1.32	0.4%
au39.2e.mus.11a	3.2	20	3.23758 ± 0.005946	0.06664 ± 0.000294	0.00025 ± 0.000007	0.00219 ± 0.000134	0.000351 ± 0.000010	2.20E-14	96.8%	47.023901	318.70 ± 1.60	0.5%
au39.2e.mus.12a	3.2	20	3.56177 ± 0.004425	0.07282 ± 0.000277	0.00025 ± 0.000007	0.00080 ± 0.000127	0.000324 ± 0.000009	2.42E-14	97.3%	47.595309	322.25 ± 1.35	0.4%
au39.2e.mus.13a	3.2	20	3.32795 ± 0.006850	0.06967 ± 0.000301	0.00023 ± 0.000004	0.00014 ± 0.000090	0.000096 ± 0.000013	2.26E-14	99.1%	47.356815	320.77 ± 1.59	0.5%
au39.2e.mus.14a	3.2	20	3.19545 ± 0.006936	0.06572 ± 0.000196	0.00024 ± 0.000007	0.00017 ± 0.000086	0.000351 ± 0.000008	2.17E-14	96.8%	47.042740	318.82 ± 1.24	0.4%
au39.2e.mus.15a	3.2	20	3.83649 ± 0.004969	0.08057 ± 0.000306	0.00023 ± 0.000005	-0.00004 ± 0.000071	0.000107 ± 0.000016	2.61E-14	99.2%	47.224692	319.95 ± 1.36	0.4%
au39.2e.mus.16a	3.2	20	2.12115 ± 0.002102	0.04456 ± 0.000152	0.00012 ± 0.000004	0.00022 ± 0.000069	0.000110 ± 0.000009	1.44E-14	98.5%	46.875810	317.78 ± 1.22	0.4%
AT-1 | Single Crystal Step Heating | 0.425-0.25mm | Muscovite												
au39.2e.mus.17a	0.5	60	0.00479 ± 0.000157	0.00007 ± 0.000032	0.00000 ± 0.000011	0.00017 ± 0.000075	0.000004 ± 0.000007	3.26E-17	78.0%	55.806041	372.53 ± 307.10	82.4%
au39.2e.mus.17b	0.6	60	0.01794 ± 0.000232	0.00037 ± 0.000036	0.00001 ± 0.000009	0.00009 ± 0.000099	0.000020 ± 0.000012	1.22E-16	66.8%	32.440275	225.66 ± 75.20	33.3%
au39.2e.mus.17c	0.7	60	0.17575 ± 0.000607	0.00349 ± 0.000040	0.00002 ± 0.000004	0.00021 ± 0.000091	0.000058 ± 0.000012	1.20E-15	90.3%	45.422524	308.71 ± 8.17	2.6%
au39.2e.mus.17d	0.85	60	0.38971 ± 0.000681	0.00787 ± 0.000046	0.00004 ± 0.000004	0.00005 ± 0.000075	0.000061 ± 0.000013	2.65E-15	95.4%	47.244085	320.07 ± 3.85	1.2%
au39.2e.mus.17e	1	60	1.26250 ± 0.001430	0.02652 ± 0.000137	0.00009 ± 0.000004	0.00013 ± 0.000075	0.000060 ± 0.000014	8.59E-15	98.6%	46.943236	318.20 ± 2.02	0.6%
au39.2e.mus.17f	1.2	60	1.82208 ± 0.003111	0.03869 ± 0.000222	0.00012 ± 0.000003	0.00006 ± 0.000058	0.000002 ± 0.000015	1.24E-14	100.0%	47.078894	319.05 ± 2.06	0.6%
au39.2e.mus.17g	1.4	60	2.48661 ± 0.004157	0.05302 ± 0.000269	0.00026 ± 0.000009	0.00049 ± 0.000099	0.000050 ± 0.000013	1.69E-14	99.4%	46.625209	316.22 ± 1.77	0.6%
au39.2e.mus.17h	1.65	60	0.15007 ± 0.000248	0.00335 ± 0.000035	0.00002 ± 0.000005	0.00023 ± 0.000089	-0.000001 ± 0.000017	1.02E-15	100.2%	44.789149	304.75 ± 9.84	3.2%
au39.2e.mus.17i	1.9	60	0.14447 ± 0.000371	0.00310 ± 0.000030	0.00002 ± 0.000005	0.00101 ± 0.000104	0.000008 ± 0.000015	9.83E-16	98.4%	45.879401	311.57 ± 10.83	3.5%
au39.2e.mus.17j	2.2	60	0.06093 ± 0.000266	0.00141 ± 0.000046	0.00002 ± 0.000006	0.00007 ± 0.000081	0.000022 ± 0.000012	4.15E-16	89.5%	38.796975	266.80 ± 20.56	7.7%
au39.2e.mus.17k	2.5	60	0.21943 ± 0.000425	0.00467 ± 0.000045	0.00003 ± 0.000004	0.00032 ± 0.000074	0.000013 ± 0.000015	1.49E-15	98.2%	46.168343	313.37 ± 7.23	2.3%

au39.2e.mus.17l	2.8	60	0.40684 ± 0.000826	0.00866 ± 0.000041	0.00002 ± 0.000003	0.00053 ± 0.000099	0.000009 ± 0.000014	2.77E-15	99.3%	46.660014	316.44 ± 3.77	1.2%
au39.2e.mus.17m	3	60	0.05274 ± 0.000408	0.00125 ± 0.000037	-0.00003 ± 0.000025	0.00015 ± 0.000084	0.000032 ± 0.000012	3.59E-16	82.0%	34.489407	239.03 ± 22.25	9.3%
au39.2e.mus.17n	3.1	30	0.19076 ± 0.000251	0.00412 ± 0.000044	0.00001 ± 0.000002	0.00012 ± 0.000119	0.000006 ± 0.000016	1.30E-15	99.1%	45.868207	311.50 ± 8.51	2.7%
au39.2e.mus.17o	3.2	30	0.00555 ± 0.000211	0.00029 ± 0.000034	-0.00001 ± 0.000018	0.00006 ± 0.000101	-0.000022 ± 0.000011	3.78E-17	215.5%	19.174515	136.72 ± 81.26	59.4%

AT-2 | Single Crystal Total Fusion | 0.425-0.25mm | Muscovite

au39.2d.mus.29a	3.2	20	1.27889 ± 0.001133	0.03992 ± 0.000305	0.00044 ± 0.000011	0.00084 ± 0.000121	0.001673 ± 0.000013	8.70E-15	61.3%	19.650153	139.98 ± 2.00	1.4%
au39.2d.mus.30a	3.2	20	4.09244 ± 0.001980	0.08637 ± 0.000424	0.00028 ± 0.000005	0.00113 ± 0.000089	0.000108 ± 0.000013	2.78E-14	99.2%	47.012223	318.63 ± 1.62	0.5%
au39.2d.mus.31a	3.2	20	4.12020 ± 0.001805	0.08683 ± 0.000428	0.00024 ± 0.000004	0.00030 ± 0.000073	0.000127 ± 0.000008	2.80E-14	99.1%	47.019268	318.67 ± 1.60	0.5%
au39.2d.mus.32a	3.2	20	1.80896 ± 0.000924	0.03810 ± 0.000332	0.00013 ± 0.000004	0.00049 ± 0.000083	0.000029 ± 0.000008	1.23E-14	99.5%	47.256665	320.15 ± 2.84	0.9%
au39.2d.mus.33a	3.2	20	6.04348 ± 0.004294	0.12693 ± 0.000421	0.00038 ± 0.000006	0.00066 ± 0.000089	0.000134 ± 0.000008	4.11E-14	99.3%	47.299937	320.42 ± 1.10	0.3%
au39.2d.mus.34a	3.2	20	2.22275 ± 0.002106	0.04649 ± 0.000101	0.00018 ± 0.000006	0.00601 ± 0.000176	0.000082 ± 0.000008	1.51E-14	98.9%	47.283853	320.32 ± 0.84	0.3%
au39.2d.mus.35a	3.2	20	10.59597 ± 0.009367	0.22174 ± 0.000705	0.00072 ± 0.000010	0.00090 ± 0.000089	0.000345 ± 0.000013	7.21E-14	99.0%	47.326168	320.58 ± 1.07	0.3%
au39.2d.mus.36a	3.2	20	5.14307 ± 0.003277	0.10799 ± 0.000154	0.00034 ± 0.000007	0.00043 ± 0.000065	0.000059 ± 0.000008	3.50E-14	99.7%	47.464398	321.44 ± 0.52	0.2%
au39.2d.mus.37a	3.2	20	4.83320 ± 0.003529	0.10092 ± 0.000461	0.00037 ± 0.000006	0.01122 ± 0.000109	0.000297 ± 0.000010	3.29E-14	98.2%	47.020539	318.68 ± 1.52	0.5%
au39.2d.mus.38a	3.2	20	3.96839 ± 0.005240	0.08564 ± 0.000285	0.00028 ± 0.000005	0.00007 ± 0.000088	0.000367 ± 0.000011	2.70E-14	97.3%	45.069899	306.51 ± 1.16	0.4%

AT-2 | Single Crystal Step Heating | 0.425-0.25mm | Muscovite

au39.2d.mus.39a	0.5	60	0.00030 ± 0.000153	0.00000 ± 0.000025	-0.00001 ± 0.000011	0.00013 ± 0.000071	0.000015 ± 0.000012	2.02E-18	-1371.5%	-994.123258	-251.56 -± 235.09	93.5%
au39.2d.mus.39b	0.6	60	0.01018 ± 0.000165	0.00017 ± 0.000035	-0.00001 ± 0.000016	0.00006 ± 0.000127	0.000035 ± 0.000013	6.92E-17	-0.3%	-0.195002	-1.44 -± 200.37	13873.8%
au39.2d.mus.39c	0.7	60	0.06994 ± 0.000382	0.00152 ± 0.000023	0.00001 ± 0.000004	0.00013 ± 0.000127	0.000024 ± 0.000012	4.76E-16	89.8%	41.266240	282.53 ± 17.37	6.1%
au39.2d.mus.39d	0.8	60	0.13303 ± 0.000179	0.00264 ± 0.000058	0.00001 ± 0.000004	0.00054 ± 0.000187	0.000039 ± 0.000012	9.05E-16	91.2%	45.912587	311.78 ± 12.13	3.9%
au39.2d.mus.39e	0.9	60	0.14367 ± 0.000262	0.00302 ± 0.000075	0.00002 ± 0.000005	0.00058 ± 0.000097	0.000031 ± 0.000012	9.77E-16	93.5%	44.520718	303.07 ± 11.55	3.8%
au39.2d.mus.39f	1	60	0.59077 ± 0.001272	0.01246 ± 0.000060	0.00004 ± 0.000003	0.00002 ± 0.000106	0.000002 ± 0.000007	4.02E-15	99.9%	47.385520	320.95 ± 2.05	0.6%
au39.2d.mus.39g	1.25	60	1.39479 ± 0.002819	0.02974 ± 0.000137	0.00008 ± 0.000003	-0.00030 ± 0.000126	-0.000028 ± 0.000009	9.49E-15	100.6%	46.899544	317.93 ± 1.71	0.5%
au39.2d.mus.39h	1.4	60	1.70796 ± 0.002028	0.03607 ± 0.000124	0.00010 ± 0.000002	-0.00013 ± 0.000067	-0.000017 ± 0.000013	1.16E-14	100.3%	47.350645	320.73 ± 1.37	0.4%
au39.2d.mus.39i	1.6	60	1.73939 ± 0.002761	0.03658 ± 0.000086	0.00008 ± 0.000002	-0.00002 ± 0.000085	0.000004 ± 0.000007	1.18E-14	99.9%	47.512417	321.74 ± 0.99	0.3%
au39.2d.mus.39j	1.8	60	0.17460 ± 0.000505	0.00367 ± 0.000089	0.00000 ± 0.000000	0.00001 ± 0.000067	-0.000028 ± 0.000010	1.19E-15	104.8%	47.522105	321.80 ± 9.55	3.0%
au39.2d.mus.39k	2.1	60	0.06386 ± 0.000196	0.00134 ± 0.000063	-0.00001 -± 0.000117	0.00010 ± 0.000100	0.000038 ± 0.000012	4.34E-16	82.5%	39.289164	269.95 ± 23.98	8.9%
au39.2d.mus.39l	2.4	60	0.06613 ± 0.000416	0.00149 ± 0.000031	0.00000 ± 0.000001	-0.00007 ± 0.000069	0.000034 ± 0.000012	4.50E-16	84.9%	37.759881	260.15 ± 17.58	6.8%
au39.2d.mus.39m	2.7	60	0.03914 ± 0.000288	0.00095 ± 0.000031	0.00000 -± 0.000002	0.00006 ± 0.000105	0.000045 ± 0.000013	2.66E-16	66.2%	27.324489	191.87 ± 29.53	15.4%
au39.2d.mus.39n	3	30	0.75844 ± 0.001851	0.01594 ± 0.000100	0.00004 ± 0.000003	0.00035 ± 0.000044	0.000053 ± 0.000012	5.16E-15	97.9%	46.615213	316.16 ± 2.61	0.8%
au39.2d.mus.39o	3.2	30	0.02698 ± 0.000171	0.00052 ± 0.000030	-0.00001 ± 0.000020	0.00008 ± 0.000070	0.000047 ± 0.000012	1.84E-16	48.6%	25.193428	177.61 ± 52.21	29.4%

AMD-1 | Single Crystal Total Fusion | 0.425-0.25mm | Muscovite

au39.2i.mus.51a	3.2	20	6.80905 ± 0.008264	0.14104 ± 0.000442	0.00055 ± 0.000010	0.00047 ± 0.000075	0.000631 ± 0.000013	4.63E-14	97.3%	46.953630	318.27 ± 1.12	0.4%
au39.2i.mus.52a	3.2	20	3.91976 ± 0.005025	0.08222 ± 0.000330	0.00034 ± 0.000009	0.00019 ± 0.000096	0.000140 ± 0.000011	2.67E-14	98.9%	47.167667	319.60 ± 1.39	0.4%
au39.2i.mus.53a	3.2	20	4.62554 ± 0.006554	0.09719 ± 0.000652	0.00032 ± 0.000007	0.00008 ± 0.000123	0.000093 ± 0.000012	3.15E-14	99.4%	47.311214	320.49 ± 2.22	0.7%
au39.2i.mus.54a	3.2	20	5.75540 ± 0.012308	0.11841 ± 0.000526	0.00038 ± 0.000008	0.00036 ± 0.000070	0.000107 ± 0.000016	3.92E-14	99.5%	48.340244	326.87 ± 1.64	0.5%
au39.2i.mus.55a	3.2	20	5.74855 ± 0.009400	0.12052 ± 0.000264	0.00039 ± 0.000008	0.00048 ± 0.000120	0.000145 ± 0.000012	3.91E-14	99.3%	47.340954	320.67 ± 0.91	0.3%
au39.2i.mus.56a	3.2	20	2.63141 ± 0.002770	0.05521 ± 0.000298	0.00017 ± 0.000005	0.00021 ± 0.000067	0.000058 ± 0.000011	1.79E-14	99.4%	47.357296	320.78 ± 1.82	0.6%
au39.2i.mus.57a	3.2	20	5.29398 ± 0.003546	0.11183 ± 0.000409	0.00029 ± 0.000004	0.00105 ± 0.000169	0.000203 ± 0.000012	3.60E-14	98.9%	46.804047	317.33 ± 1.21	0.4%
au39.2i.mus.58a	3.2	20	3.21716 ± 0.003149	0.06664 ± 0.000342	0.00023 ± 0.000004	0.00031 ± 0.000081	0.000167 ± 0.000011	2.19E-14	98.5%	47.533239	321.87 ± 1.74	0.5%
au39.2i.mus.59a	3.2	20	4.34674 ± 0.005817	0.09168 ± 0.000385	0.00029 ± 0.000006	0.00040 ± 0.000059	0.000113 ± 0.000016	2.96E-14	99.2%	47.049269	318.86 ± 1.46	0.5%
au39.2i.mus.60a	3.2	20	7.27656 ± 0.005426	0.15459 ± 0.000521	0.00049 ± 0.000005	0.00073 ± 0.000085	0.000353 ± 0.000012	4.95E-14	98.6%	46.397103	314.80 ± 1.11	0.4%

AMD-1 | Single Crystal Step Heating | 0.425-0.25mm | Muscovite

au39.2i.mus.61a	0.5	60	0.00002 ± 0.000142	0.00000 ± 0.000036	-0.00001 ± 0.000013	0.00002 ± 0.000100	-0.000002 ± 0.000009	1.22E-19	3207.9%	6.026610	44.08 ± 20637.70	46817.2%
au39.2i.mus.61b	0.6	60	0.00217 ± 0.000142	0.00001 ± 0.000034	-0.00001 ± 0.000013	0.00011 ± 0.000062	0.000009 ± 0.000010	1.47E-17	-27.0%	-45.352255	-370.92 -± 6123.13	1650.8%
au39.2i.mus.61c	0.7	60	0.01846 ± 0.000227	0.00036 ± 0.000023	0.00002 ± 0.000012	0.00020 ± 0.000069	-0.000032 ± 0.000011	1.26E-16	150.7%	52.025257	349.55 ± 65.44	18.7%
au39.2i.mus.61d	0.8	60	0.10045 ± 0.000298	0.00215 ± 0.000064	0.00003 ± 0.000007	0.00013 ± 0.000098	0.000001 ± 0.000005	6.83E-16	99.6%	46.551023	315.76 ± 10.67	3.4%
au39.2i.mus.61e	0.9	60	0.28141 ± 0.000668	0.00592 ± 0.000075	0.00002 ± 0.000005	0.00017 ± 0.000108	0.000005 ± 0.000005	1.91E-15	99.5%	47.275424	320.27 ± 4.50	1.4%
au39.2i.mus.61f	1	60	0.42510 ± 0.000589	0.00913 ± 0.000116	0.00007 ± 0.000008	0.00014 ± 0.000099	-0.000003 ± 0.000006	2.89E-15	100.2%	46.542283	315.70 ± 4.23	1.3%
au39.2i.mus.61g	1.25	60	2.18686 ± 0.002867	0.04601 ± 0.000130	0.00015 ± 0.000004	0.00032 ± 0.000091	0.000014 ± 0.000006	1.49E-14	99.8%	47.445850	321.33 ± 1.03	0.3%
au39.2i.mus.61h	1.4	60	1.61856 ± 0.002308	0.03409 ± 0.000117	0.00013 ± 0.000004	0.00050 ± 0.000088	0.000006 ± 0.000006	1.10E-14	99.9%	47.424055	321.19 ± 1.25	0.4%
au39.2i.mus.61i	1.6	60	1.20092 ± 0.002247	0.02536 ± 0.000048	0.00010 ± 0.000005	0.00013 ± 0.000094	0.000001 ± 0.000010	8.17E-15	100.0%	47.350440	320.73 ± 1.20	0.4%
au39.2i.mus.61j	1.8	60	0.95724 ± 0.001814	0.02038 ± 0.000101	0.00008 ± 0.000005	0.00016 ± 0.000088	-0.000016 ± 0.000012	6.51E-15	100.5%	46.959848	318.30 ± 2.05	0.6%
au39.2i.mus.61k	2.1	60	0.25951 ± 0.000638	0.00551 ± 0.000029	0.00003 ± 0.000004	-0.00003 ± 0.000122	-0.000001 ± 0.000005	1.77E-15	100.2%	47.121470	319.31 ± 2.64	0.8%
au39.2i.mus.61l	2.4	60	0.14634 ± 0.000215	0.00304 ± 0.000072	0.00002 ± 0.000005	0.00013 ± 0.000054	0.000010 ± 0.000006	9.96E-16	97.9%	47.105852	319.21 ± 8.61	2.7%
au39.2i.mus.61m	2.7	60	0.09090 ± 0.000387	0.00197 ± 0.000051	0.00000 ± 0.000003	0.00010 ± 0.000078	0.000013 ± 0.000006	6.18E-16	95.8%	44.214354	301.14 ± 10.05	3.3%
au39.2i.mus.61n	3	30	0.07490 ± 0.000362	0.00163 ± 0.000042	0.00000 ± 0.000002	0.00003 ± 0.000096	0.000002 ± 0.000006	5.10E-16	99.3%	45.743835	310.72 ± 11.29	3.6%
au39.2i.mus.61o	3.2	30	0.05673 ± 0.000225	0.00120 ± 0.000042	0.00000 ± 0.000003	0.00014 ± 0.000108	-0.000007 ± 0.000010	3.86E-16	103.7%	47.249162	320.10 ± 20.36	6.4%

AMD-2 | Single Crystal Total Fusion | 0.425-0.25mm | Muscovite

au39.2h.mus.73a	3.2	20	11.58847 ± 0.009183	0.23660 ± 0.000498	0.00085 ± 0.000014	0.00201 ± 0.000090	0.000484 ± 0.000015	7.88E-14	98.8%	48.375294	327.09 ± 0.76	0.2%
au39.2h.mus.74a	3.2	20	19.79094 ± 0.024298	0.40999 ± 0.000763	0.00149 ± 0.000015	0.00204 ± 0.000080	0.000667 ± 0.000015	1.35E-13	99.0%	47.790145	323.46 ± 0.73	0.2%

au39.2h.mus.75a	3.2	20	9.80388 ± 0.010936	0.19553 ± 0.000474	0.00088 ± 0.000016	0.00160 ± 0.000092	0.001432 ± 0.000015	6.67E-14	95.7%	47.976926	324.62 ± 0.92	0.3%
au39.2h.mus.76a	3.2	20	5.40049 ± 0.007781	0.10129 ± 0.000237	0.00068 ± 0.000011	0.00095 ± 0.000090	0.001824 ± 0.000016	3.67E-14	90.0%	47.994714	324.73 ± 1.04	0.3%
au39.2h.mus.77a	3.2	20	19.74141 ± 0.015574	0.39998 ± 0.001034	0.00136 ± 0.000011	0.00228 ± 0.000080	0.000888 ± 0.000014	1.34E-13	98.7%	48.699494	329.10 ± 0.90	0.3%
au39.2h.mus.78a	3.2	20	14.23407 ± 0.008370	0.29509 ± 0.000462	0.00107 ± 0.000011	0.00251 ± 0.000097	0.000387 ± 0.000026	9.68E-14	99.2%	47.848330	323.82 ± 0.57	0.2%
au39.2h.mus.79a	3.2	20	7.19353 ± 0.008845	0.14955 ± 0.000520	0.00049 ± 0.000005	0.00077 ± 0.000149	0.000367 ± 0.000009	4.89E-14	98.5%	47.375305	320.89 ± 1.21	0.4%
au39.2h.mus.80a	3.2	20	3.38964 ± 0.005677	0.07053 ± 0.000175	0.00022 ± 0.000004	0.00058 ± 0.000055	0.000047 ± 0.000008	2.31E-14	99.6%	47.864465	323.92 ± 1.00	0.3%
au39.2h.mus.81a	3.2	20	6.45789 ± 0.008171	0.13517 ± 0.000711	0.00046 ± 0.000005	0.00067 ± 0.000083	0.000177 ± 0.000009	4.39E-14	99.2%	47.390191	320.98 ± 1.76	0.5%
au39.2h.mus.82a	3.2	20	4.90844 ± 0.007642	0.10342 ± 0.000417	0.00029 ± 0.000006	0.00090 ± 0.000094	0.000169 ± 0.000007	3.34E-14	99.0%	46.978828	318.42 ± 1.40	0.4%

AMD-2 | Single Crystal Step Heating | 0.425-0.25mm | Muscovite

au39.2h.mus.83a	0.6	60	0.00126 ± 0.000138	0.00004 ± 0.000024	0.00002 ± 0.000012	0.00009 ± 0.000071	0.000016 ± 0.000008	8.54E-18	-279.6%	-99.640409	-944.20 -± 1139.20	120.7%
au39.2h.mus.83b	0.7	60	0.01175 ± 0.000170	0.00026 ± 0.000019	0.00001 ± 0.000012	0.00003 ± 0.000080	0.000017 ± 0.000009	7.99E-17	57.3%	26.242587	184.65 ± 73.90	40.0%
au39.2h.mus.83c	0.8	60	0.06236 ± 0.000318	0.00106 ± 0.000047	0.00001 ± 0.000007	-0.00001 ± 0.000090	0.000058 ± 0.000009	4.24E-16	72.3%	42.469819	290.15 ± 25.21	8.7%
au39.2h.mus.83d	0.9	60	0.18838 ± 0.000288	0.00359 ± 0.000031	0.00002 ± 0.000006	-0.00002 ± 0.000069	0.000048 ± 0.000014	1.28E-15	92.5%	48.538932	328.10 ± 8.57	2.6%
au39.2h.mus.83e	1	60	1.06286 ± 0.001808	0.02173 ± 0.000145	0.00005 ± 0.000003	-0.00003 ± 0.000050	0.000065 ± 0.000009	7.23E-15	98.2%	48.034714	324.98 ± 2.41	0.7%
au39.2h.mus.83f	1.1	60	3.37061 ± 0.002866	0.07051 ± 0.000291	0.00023 ± 0.000004	0.00020 ± 0.000088	0.000020 ± 0.000014	2.29E-14	99.8%	47.716956	323.01 ± 1.42	0.4%
au39.2h.mus.83g	1.25	60	6.32415 ± 0.005415	0.13313 ± 0.000634	0.00046 ± 0.000007	0.00020 ± 0.000074	0.000007 ± 0.000014	4.30E-14	100.0%	47.488070	321.59 ± 1.57	0.5%
au39.2h.mus.83h	1.4	60	8.28680 ± 0.010301	0.17273 ± 0.000578	0.00052 ± 0.000009	0.00089 ± 0.000092	0.000061 ± 0.000012	5.64E-14	99.8%	47.872176	323.97 ± 1.17	0.4%
au39.2h.mus.83i	1.6	60	11.25767 ± 0.008499	0.23818 ± 0.000507	0.00069 ± 0.000007	0.00099 ± 0.000055	0.000054 ± 0.000011	7.66E-14	99.9%	47.199175	319.79 ± 0.73	0.2%
au39.2h.mus.83j	1.8	60	7.08788 ± 0.007255	0.14990 ± 0.000516	0.00043 ± 0.000005	0.00009 ± 0.000087	-0.000017 ± 0.000012	4.82E-14	100.1%	47.282933	320.31 ± 1.16	0.4%
au39.2h.mus.83k	2.1	60	1.45636 ± 0.002563	0.03078 ± 0.000145	0.00009 ± 0.000003	0.00010 ± 0.000088	0.000004 ± 0.000007	9.91E-15	99.9%	47.280936	320.30 ± 1.67	0.5%
au39.2h.mus.83l	2.6	60	0.89712 ± 0.000882	0.01879 ± 0.000064	0.00005 ± 0.000002	0.00011 ± 0.000090	-0.000025 ± 0.000011	6.10E-15	100.8%	47.737328	323.14 ± 1.64	0.5%

AMD-3 | Single Crystal Total Fusion | 0.425-0.25mm | Muscovite

au39.2f.mus.95a	3.2	20	16.19363 ± 0.022081	0.33611 ± 0.000977	0.00108 ± 0.000010	0.00194 ± 0.000100	0.000352 ± 0.000013	1.10E-13	99.4%	47.870122	323.96 ± 1.05	0.3%
au39.2f.mus.96a	3.2	20	11.76064 ± 0.015618	0.24213 ± 0.000959	0.00083 ± 0.000009	0.00054 ± 0.000140	0.000397 ± 0.000013	8.00E-14	99.0%	48.086140	325.30 ± 1.38	0.4%
au39.2f.mus.97a	3.2	20	19.13089 ± 0.015609	0.38968 ± 0.001415	0.00129 ± 0.000010	0.00173 ± 0.000130	0.000966 ± 0.000013	1.30E-13	98.5%	48.360338	327.00 ± 1.24	0.4%
au39.2f.mus.98a	3.2	20	14.39401 ± 0.025554	0.29743 ± 0.000499	0.00089 ± 0.000008	0.00134 ± 0.000046	0.000401 ± 0.000031	9.79E-14	99.2%	47.996715	324.74 ± 0.83	0.3%
au39.2f.mus.99a	3.2	20	11.88874 ± 0.013028	0.24823 ± 0.000660	0.00089 ± 0.000011	0.00126 ± 0.000124	0.000167 ± 0.000013	8.09E-14	99.6%	47.695337	322.87 ± 0.94	0.3%
au39.2f.mus.100a	3.2	20	19.36826 ± 0.009806	0.40584 ± 0.000958	0.00145 ± 0.000018	0.00439 ± 0.000157	0.000431 ± 0.000027	1.32E-13	99.3%	47.410660	321.11 ± 0.79	0.2%
au39.2f.mus.101a	3.2	20	9.37008 ± 0.007934	0.18938 ± 0.000729	0.00076 ± 0.000008	0.00056 ± 0.000082	0.000436 ± 0.000014	6.37E-14	98.6%	48.798324	329.71 ± 1.33	0.4%
au39.2f.mus.102a	3.2	20	20.43290 ± 0.021763	0.42809 ± 0.001195	0.00129 ± 0.000017	0.00395 ± 0.000078	0.000072 ± 0.000016	1.39E-13	99.9%	47.681204	322.79 ± 0.97	0.3%
au39.2f.mus.103a	3.2	20	12.28181 ± 0.026454	0.25744 ± 0.001073	0.00075 ± 0.000011	0.00163 ± 0.000146	0.000157 ± 0.000014	8.36E-14	99.6%	47.526495	321.83 ± 1.52	0.5%

au39.2f.mus.104a	3.2	20	11.73911 ± 0.018769	0.24898 ± 0.000601	0.00083 ± 0.000010	0.00250 ± 0.000160	0.000352 ± 0.000025	7.99E-14	99.1%	46.730486	316.88 ± 0.95	0.3%
AMD-3 | Single Crystal Step Heating | 0.425-0.25mm | Muscovite												
au39.2f.mus.105a	0.6	60	0.00212 ± 0.000142	0.00010 ± 0.000028	0.00000 -± 0.000017	0.00016 ± 0.000077	0.000049 ± 0.000012	1.44E-17	-585.3%	-128.332519	-1339.82 -± 602.16	44.9%
au39.2f.mus.105b	0.7	60	0.03551 ± 0.000347	0.00069 ± 0.000054	-0.00001 -± 0.000044	-0.00007 ± 0.000102	0.000041 ± 0.000012	2.42E-16	65.9%	33.736765	234.13 ± 46.18	19.7%
au39.2f.mus.105c	0.8	60	0.30612 ± 0.000529	0.00558 ± 0.000056	0.00002 ± 0.000003	-0.00005 ± 0.000123	0.000164 ± 0.000012	2.08E-15	84.1%	46.173204	313.40 ± 5.78	1.8%
au39.2f.mus.105d	0.9	60	0.42697 ± 0.000635	0.00755 ± 0.000040	0.00003 ± 0.000003	0.00001 ± 0.000110	0.000050 ± 0.000015	2.90E-15	96.6%	54.573780	365.07 ± 4.43	1.2%
au39.2f.mus.105e	1	60	2.01518 ± 0.001218	0.03782 ± 0.000131	0.00010 ± 0.000004	0.00011 ± 0.000110	0.000182 ± 0.000012	1.37E-14	97.3%	51.855061	348.51 ± 1.42	0.4%
au39.2f.mus.105f	1.1	60	4.05269 ± 0.002870	0.07984 ± 0.000382	0.00024 ± 0.000005	0.00001 ± 0.000074	0.000178 ± 0.000012	2.76E-14	98.7%	50.099211	337.73 ± 1.68	0.5%
au39.2f.mus.105g	1.25	60	4.73673 ± 0.006232	0.09602 ± 0.000225	0.00030 ± 0.000004	0.00013 ± 0.000104	0.000127 ± 0.000016	3.22E-14	99.2%	48.940287	330.58 ± 0.95	0.3%
au39.2f.mus.105h	1.35	60	4.02509 ± 0.005676	0.08268 ± 0.000118	0.00025 ± 0.000005	0.00010 ± 0.000118	0.000106 ± 0.000015	2.74E-14	99.2%	48.304125	326.65 ± 0.76	0.2%
au39.2f.mus.105i	1.45	60	3.63586 ± 0.005127	0.07563 ± 0.000267	0.00025 ± 0.000007	0.00011 ± 0.000107	0.000086 ± 0.000016	2.47E-14	99.3%	47.737809	323.14 ± 1.30	0.4%
au39.2f.mus.105j	1.6	60	4.92581 ± 0.006787	0.10336 ± 0.000282	0.00029 ± 0.000005	0.00025 ± 0.000102	0.000122 ± 0.000017	3.35E-14	99.3%	47.308845	320.47 ± 1.04	0.3%
au39.2f.mus.105k	1.8	60	6.69809 ± 0.005315	0.13983 ± 0.000445	0.00040 ± 0.000005	0.00006 ± 0.000092	0.000134 ± 0.000014	4.56E-14	99.4%	47.618046	322.40 ± 1.08	0.3%
au39.2f.mus.105l	2	60	8.09070 ± 0.009521	0.16831 ± 0.000608	0.00047 ± 0.000005	0.00009 ± 0.000072	0.000188 ± 0.000008	5.50E-14	99.3%	47.739038	323.15 ± 1.24	0.4%
au39.2f.mus.105m	2.2	60	1.67019 ± 0.002570	0.03470 ± 0.000214	0.00012 ± 0.000004	0.00008 ± 0.000057	0.000017 ± 0.000010	1.14E-14	99.7%	47.978641	324.63 ± 2.15	0.7%
au39.2f.mus.105n	2.5	60	0.60631 ± 0.001167	0.01276 ± 0.000066	0.00003 ± 0.000003	0.00011 ± 0.000122	0.000016 ± 0.000007	4.12E-15	99.2%	47.131020	319.37 ± 2.05	0.6%
au39.2f.mus.105o	2.8	60	0.48565 ± 0.000744	0.01021 ± 0.000081	0.00000 ± 0.000000	0.00016 ± 0.000074	0.000012 ± 0.000007	3.30E-15	99.3%	47.241322	320.05 ± 2.95	0.9%